SURFACE FUNCTIONALISATION OF NANOPARTICLES AND THEIR BIOLOGICAL APPLICATIONS

A THESIS SUBMITTED BY

RAMYA JAGANNATHAN

FOR THE AWARD OF A
PH.D. DEGREE IN BIOTECHNOLOGY
SUBMITTED TO THE UNIVERSITY OF PUNE

UNDER THE GUIDANCE OF
DR. ASMITA PRABHUNE

AND CO-GUIDANCE OF
DR. PANKAJ PODDAR

NATIONAL CHEMICAL LABORATORY, PUNE, INDIA

JAN 2010

CONTENTS

1. LIST OF TABLES i

2. LIST OF FIGURES ii

3. ACKNOWLEDGEMENT viii

4. DECLARATIONS x-xii

5. ABSTRACT OF THE THESIS xiii

6. ABBREVIATIONS xvi

7. CHAPTER 1: *INTRODUCTION* 1

1.1. Introduction 3

1.1.1. Profile of nanoparticles 3

1.1.2. What are these nanoparticles and why are they so important? 4

1.1.2.1. Size-dependent effects 5

1.1.3. Properties of nanoparticles 8

1.1.4. Synthesis of nanoparticles and its applications 10

1.1.5. Nanoscience, nanotechnology and risks 14

1.2. Surface functionalisation of nanoparticles 16

1.2.1. Science of functionalisation 16

1.2.2. Different types of functionalisation 17

1.2.3. Applications in biology 18

1.3. Outline of the thesis 19

1.4. Reference 21

8. CHAPTER 2: *EXPERIMENTAL PROCEDURES* 24

2.1. Spectroscopy 25

2.1.1. Ultra-violet and Visible Spectroscopy 25

2.1.2. Fourier Transform Infra-Red (FTIR) Spectroscopy 27

2.1.3. Fluorescence Spectroscopy 28

2.1.4. X-ray Photoemission Spectroscopy (XPS) or Electron Spectroscopy for Chemical Analysis (ESCA) 30

2.1.5. Nuclear Magnetic Resonance (NMR) Spectroscopy 32

2.2. X-Ray Diffraction (XRD) 33

2.3. Transmission Electron Microscopy (TEM) 34

2.4. Scanning Electron Microscopy (SEM) 37

2.5. Atomic Force Microscopy (AFM) 38

2.6. Dynamic Light Scattering (DLS) study 39

2.7. HPLC 41

2.8. Thermo gravimetric analysis (TGA) 42

2.9. Electrophoresis 43

2.10. Contact Angle measurements 43

2.11. References 43

9. CHAPTER 3: *SURFACE FUNCTIONALISATION OF NANOPARTICLES USING BIOMOLECULES* 46

3.1. Part 1: Synthesis of gold nanoparticles using antibiotics 48

3.1.1. Synthesis of gold nanoparticles using cephalexin 54

3.1.1.1.Experimental details 54

3.1.1.2.Results and discussions 55

3.1.2. Synthesis of gold nanoparticles using cefaclor 67

3.1.2.1. Experimental details 69

3.1.2.2. Results and discussions 69

3.1.3. Synthesis of gold nanoparticles using ampicillin 74

3.1.3.1.Experimental details 74

3.1.3.2.Results and discussions 75

3.1.4. Anti-bacterial activity of gold nanoparticles synthesized by antibiotics 77

3.1.5. Conclusions 79
3.2. Part 2: Functionalisation of iron oxide nanoparticles with Penicillin G acylase 81
3.2.1. Synthesis of iron oxide nanoparticles and capping by enzyme Pencillin G acylase 83
3.2.1.1.Experimental Details 84
3.2.1.2.Results and Discussions 86
3.2.2. Conclusions 90
3.3. References 92

10. CHAPTER 4: *NUCLEATION AND GROWTH OF GOLD NANOPARTICLES* 95
4.1.Introduction 97
4.1.1. DLS theory 100
4.1.2. Surface Plasmon Resonance 103
4.2.Experimental Details 106
4.3.Results and Discussions 107
4.3.1. DLS study of the system and its data analysis 107
4.3.2. UV-vis absorption spectroscopy data 113
4.3.3. TEM and SAED measurements 117
4.4.Conclusion 112
4.5.References 122

11.* CHAPTER 5: *SOLUBILISING CURCUMIN, SYNTHESIZING GOLD NANOPARTICLES AND THEIR ANTI-OXIDANT PROPERTY 124
5.1.1. PART I: Study of dissolution of curcumin in water - An Introduction 126
5.1.2. Results and discussions 129
5.1.2.1. Temperature dependent UV-vis absorption spectroscopy of curcumin in water and effects of intra/inter-molecular H-bonding on the electronic transitions 130
5.1.2.2. Effect of temperature on the spectrum of curcumin 135

5.1.2.3. Establishing and estimating solubility of curcumin in water 140
5.1.2.4. Addressing the stability of curcumin in water 141
5.1.2.5. Fluorescence of curcumin in water 146
5.1.3. Conclusions 147
5.2.1. PART II: Synthesis of gold nanoparticles using aqueous curcumin – An Introduction 149
5.2.2. Results and discussions 150
5.2.3. Conclusions 155
5.3. References 157

8. SUMMARY 159

9. LIST OF PUBLICATIONS 165

LIST OF TABLES

Table no.	Table legend	Page no.
1	Origin of electron microscope	35
2	Immobilisation of PGA onto nanoparticle: effect of enzyme loading on nanoparticles	90

LISTS OF FIGURES

Figure no.	Figure Legends	Page no.
Figure 1.1.	Cartoon representing the gap between the bulk and molecular species, where the 'nano' regime reigns	5
Figure 1.2.	Size comparison ranging from atomic nucleus to man	6
Figure 1.3.	Evolution of the band gap and the density of states as the number of atoms in a system increases	7
Figure 1.4.	Lycurgus Cup	9
Figure 1.5.	Two different approaches to control matter at the nanoscale	11
Figure 1.6.	The mean size and the size distribution	13
Figure 1.7.	Optomechanical crystals; periodic nanobeams bring light and sound together	14
Figure 1.8.	Movement of particles through the lungs	15
Figure 2.1.	Representative Jablonski diagram	29
Figure 2.2.	Schematic diagram of the XPS process showing photo ionization of an atom by the ejection of a 1s electron	31
Figure 2.3.	Schematic showing diffraction of X-ray from scattering centers (atoms) in the crystal	33
Figure 2.4.	Schematic graph showing typical intensity fluctuations for large and small particles	40
Figure 2.5.	Schematic showing two beams that interfere destructively (A) and constructively (B) as the particles fluctuate	41
Figure 2.6.	Schematic representation of water droplet on a hydrophilic and hydrophobic surface	43
Figure 3.1.	Schematic representation of vancomycin capped gold nanoparticles	49
Figure 3.2.	A schematic illustration of the reaction pathways that lead to fcc metal nanocrystals having different shapes	50
Figure 3.3.	Different shapes of gold nanoparticles	53
Figure 3.4.	Time-dependent UV-vis-NIR spectra of cephalexin	55

	reduced gold nanoparticles from various concentrations of chloroauric acid	
Figure 3.5.	Transmission electron micrograph of as-synthesized Au nanoparticles	57
Figure 3.6.	X-ray diffraction pattern of as-synthesized gold nanoparticles	59
Figure 3.7.	Electrophoresis of nanoparticles	59
Figure 3.8.	Chemical structure of (A) cephalexin, (B) 7-amino cephalosporinic acid (7-ACA), and (C) phenyl glycine molecules	60
Figure 3.9.	UV-vis-NIR absorption spectra of various concentrations of gold ions reduced by 7-amino cephalosporinic acid (7-ACA)	61
Figure 3.10.	FTIR spectra of (1) cephalexin (2) gold nanoparticles bound with cephalexin	62
Figure 3.11.	^{1}H NMR spectrum of cephalexin	63
Figure 3.12.	^{1}H NMR spectrum of gold nanoparticles reduced by cephalexin.	64
Figure 3.13.	X-ray photoelectron spectroscopy data for cephalexin (panels A-D) and cephalexin-reduced gold particles	66
Figure 3.14.	Structure of cefaclor	68
Figure 3.15.	UV-visible spectrum of gold nanoparticles synthesized at different concentrations of cefaclor and chloroauric acid	69
Figure 3.16.	UV Visible spectrum of cefaclor reduced gold nanoparticles at cefaclor concentration of 1 x 10^{-5}M and varying concentration of gold nanoparticles	70
Figure 3.17.	TEM micrographs and SAED pattern of cefaclor synthesized gold nanoparticles, at constant cefaclor concentration of 1 x 10^{-5}M	72
Figure 3.18.	X-ray diffraction pattern of cefaclor (1 x 10^{-5}M) synthesized gold nanoparticles (4 x 10^{-4}M)	73
Figure 3.19.	Structure of ampicillin	74
Figure 3.20.	TEM micrographs of ampicillin (1 x 10^{-5} M) reduced gold nanoparticles (1 x 10^{-4} M)	75
Figure 3.21.	HRTEM of ampicillin reduced gold nanoparticles	76
Figure 3.22.	HRTEM of larger ampicillin reduced gold nanoparticles	76

Figure 3.23.	Growth curve of *E.coli* (NCIM no. 2931) culture	78
Figure 3.24.	Growth curve of Staphylococcus (NCIM no. 2079) culture	78
Figure 3.25.	Anti-bacterial activity shown on spread plates of *B. subtilis* (NCIM no. 2063) culture. (A) Only culture, (B) Sodium borohydride reduced Au NPs, (C) Cephalexin synthesized Au NPs and (D) Cefaclor synthesized Au NPs	79
Figure 3.26.	Schematic representation of facets of use of magnetic nanoparticles	81
Figure 3.27.	Schematic representation of the objective in this study. Step 1 is the synthesis of magnetic nanoparticles, step 2 and 3 comprises of capping the bare nanoparticles with enzyme and glutaraldehyde respectively, step 4 is immobilizing enzyme onto the glutaraldehyde capped nanoparticles and step 5 involves determining the activity of the enzyme conjugated to these nanoparticles.	83
Figure 3.28.	X-ray diffraction pattern of iron oxide nanoparticles synthesized by co-precipitation method.	87
Figure 3.29.	TEM micrographs of iron oxide nanoparticles	87
Figure 3.30.	Comparison of binding percentage between enzyme immobilized on glutaraldehyde capped nanoparticles and bare nanoparticles	88
Figure 3.31.	AFM contact-mode image of (a) unbound iron oxide nanoparticles and (b) enzyme bound glutaraldehyde capped iron oxide nanoparticles	88
Figure 3.32.	Saturation kinetics of PGA binding on nanoparticles	89
Figure 4.1.	Calculated extinction, scattering and absorption spectra of a particle of size, d = 16 nm	97
Figure 4.2.	Interference pattern of light scattered from two scattering centers of small particles (A) and from larger particles (B). (C) & (D) shows the change in the interference pattern of scattered intensity with time, caused by Brownian motion of two scattering particles	101
Figure 4.3.	Schematic representation of the plasmon oscillation (shown in green) for spherical nanoparticles	104
Figure 4.4.	Schematic representation of transverse and longitudinal oscillations in an anisotropic particle	105
Figure 4.5.	Normalized temporal correlations of the intensity of	108

	scattered light	
	Intercepts of the intensity correlation function of scattered light (O) and the overall intensity of scattered light (Δ) vs. the incubation time of the sample	
Figure 4.6.	Examples of particle size distributions obtained during the early phases of the synthesis of gold colloids in the presence of cephalexin during incubation at 15 °C	109
	TEM micrographs of the gold nanoparticles synthesized at 15 °C after 1 hour reaction time	
Figure 4.7.	Changes in the mean particle size for both the small and the large gold colloids as a function of incubation period and solution temperature	111
Figure 4.8.	Changes in the total intensity of scattered light during the synthesis of colloidal gold particles at T = 15 and 25 °C	112
	Percentage of total light scattered by either population of colloidal gold particles during synthesis at T = 15 °C	
Figure 4.9.	Image of the vials containing gold nanoparticles synthesized by the cephalexin mediated method in aqueous medium at temperatures 15, 25, and 35 °C	113
Figure 4.10.	*In situ* UV-visible absorption spectroscopy measurements to demonstrate the temporal evolution of peaks due to the surface plasmon resonance absorption as the population of the nanoparticles increases in the solution	115
Figure 4.11.	A) Time-dependent hypsochromic shift in the wavelength of the surface plasmon resonance absorption peaks during the synthesis for reactions at temperatures 25 and 35 °C. (B) Temporal evolution in the absorption peak intensity for the reactions at 25 and 35 °C	116
Figure 4.12.	TEM micrographs of the gold nanoparticles synthesized at 15 °C	117
Figure 4.13.	TEM micrographs of the gold nanoparticles synthesized at 25 °C	118
Figure 4.14.	TEM micrographs of the gold nanoparticles synthesized at 35 °C	119
Figure 4.15.	Selected area electron diffraction (SAED) patterns of gold nanoparticles synthesized at temperatures 15 °C (A), 25 °C (B), and 35 °C (C).	120

Figure 5.1.	From the cover page of the weekly magazine Science News, 2007	127
Figure 5.2.	Structure of (A) curcumin, (B) demethoxycurcumin and (C) bis-demethoxycurcumin	130
Figure 5.3.	(A) Temperature dependent UV-Visible spectra of curcumin in water, (B) Change in intensity (of absorption at λ_{max} ~ 420 nm) vs. temperature and (C) Comparison spectrum of curcumin in water with curcumin in methanol	132
Figure 5.4.	Temperature dependent UV-visible spectroscopy of curcumin in methanol	134
Figure 5.5.	(A) UV-Visible Spectroscopy of curcumin in water; the graph shows spectra taken at 90 °C, cooled back to room temperature ~ 25 °C and reheated to 90 °C. (B) Schematic picture of dissolution of curcumin in water upon heating and cooling, and its corresponding blue shift and red shift in its absorption spectra	135 138
Figure 5.6.	UV-Visible spectroscopy of curcumin in water and methanol at increasing temperatures and at different vol %(A: 50% methanol, B: 20% methanol and C: 10% methanol in water)	139
Figure 5.7.	Picture of curcumin in water after filtering through a 0.22 μ filter at different temperature. (i) Color of solution filtered immediately after dissolution by heating and (ii) Color of solution filtered after cooling	140
Figure 5.8.	UV-vis spectra of curcumin in methanol	142
Figure 5.9.	Proton NMR spectra of curcumin in CD_3OD. The first spectrum is that of curcumin without any heat treatment and the second spectra is that of curcumin with heat treatment in water	143
Figure 5.10.	FTIR spectra of curcumin at different stages of heating in water	144
Figure 5.11.	HPLC chromatograms of curcumin (A) before heating (B) after heating in water, drying and re-dissolving in methanol	145
Figure 5.12.	Photoluminescence of curcumin in methanol (1) and water (2) at the excitation wavelength of 420 nm.	146
Figure 5.13.	UV-Visible Spectroscopy of gold nanoparticles at different concentrations: (1) 1 x 10^{-4} M, (2) 1.5 x 10^{-4} M, (3) 2 x 10^{-}	150

	^{4} M, (4) 5 x 10^{-4} M and (5) 5 x 10^{-5} M, synthesized by curcumin	
Figure 5.14.	TEM micrographs of gold nanoparticles (1.5 x 10^{-4}M) synthesized by curcumin (A), SAED pattern (B) and the particle size distribution (C)	152
Figure 5.15.	Thermo-gravimetric analysis of gold nanoparticles synthesized by curcumin	153
Figure 5.16.	Fluorescence spectra of (1) curcumin in water and (2) gold nanoparticles (1.5 x 10^{-4}M) synthesized by curcumin in water	154
Figure 5.17.	Anti-oxidant activity by DPPH radical test. (1) Only DPPH in water as control, (2) gold nanoparticles (1.5 x 10^{-4}M) synthesized by curcumin in water and (3) curcumin in water.	155

ACKNOWLEDGEMENTS

"Kill therefore with the sword of wisdom the doubt born of ignorance that lies in thy heart", advised the charioteer Krishna to warrior Arjuna.
This world moves on the consummation of the wisdom of our forefathers in all the facets of the universe. With this in mind, in deep veneration I thank our forefathers for their gift to their children, however small or big, without which we would be doomed in ignorance, as we proceed to gift our children, the knowledge, however small or big.

First and foremost, I would like to extend my sincere gratitude to Dr. Asmita Prabhune and Dr. Pankaj Poddar for accepting me and introducing me to this exciting field of interdisciplinary science, and for all the help and support. Their inspiration, encouragement and admonishments throughout my PhD has shaped up the research years at NCL as a learning experience.

Dr. Prabhune will always be remembered for someone who was there for me at the most needed hour. She is one who teaches and cares for with the student in mind. I constantly learn from her, from her scientific as well as mundane experiences. Her dedicated help and advice supported me more than words can say. I feel fortunate being associated with her.

During my initial days under Dr. Poddar's guidance, his enthusiasm and passion for scientific work gave me a direction and a way to work out in science. These years, I have learnt extensively from him, including finding out solutions, approaching the problems from all possible angles and not to incubate them and how to write scientifically.

I am highly grateful to him for showing me the dos and don'ts of life in research.

Dr. Saurav Pal is a great teacher, from whom I've floundered to learn the ways of Physics and Chemistry! He has helped me always, with a patient ear and good guidance. I'm thankful to him for allowing me to work in this great laboratory and constant support.

I am highly thankful to my seniors – Hrushikesh Joshi, Vipul Bansal, Ambarish Sanyal, Akhilesh Rai, Tanushree Sanyal, Amit Singh, Atul Bharde, Sourabh Shukla, Manasi, Minakshi, Deepti, Prathap Chandran, Sanjay Singh, Ambrish Rathore, Imran Usmani and Anil Jhadav. My labmates Adhish, Raja, Vivekanad, Tuhin, Priyanka, Virginia, Umesh, Sudarshan, Baisakhi, Siddharth and Chandrashekar were all very helpful. Working with Priya Mary Abraham has also been a good experience. In addition to the helping hand that she had rendered, I also learnt a lot from her, by way of patience and perseverance. I had the pleasure to

work with Ankita Gupta, Amit Kumar, Aradhana, Neetu Sharma, who did their graduation projects in this lab and have been somehow beneficial for the work presented in this thesis. I also want to thank Abhishek, Manasi, Manaswini, Gowrishankar, Bhaskar; working and learning with them was very fruitful.

It is an honour for me to whole-heartedly thank Dr. K. N. Ganesh, Dr. R. R. Bhonde, Dr. K. Vijaymohan, Dr. Satish Ogale, Dr. C. S. Gopinath, Dr. Rajamohanan, Dr. A. Basu, Dr. B. L. V. Prasad, Dr. Anil Kumar, Dr. Suresh Bhat, Dr. Ashok Giri, Dr. Guruswamy, Dr. Venkat Panchagnula, Dr. A. Pundle and Dr. Dhiman Sarkar for their time and guidance. I also want to thank Dr. Ponrathnum and Dr. Peddireddy.

I would like to give special thanks to Ms. Nivika Gupta for her help with lyophilisation. Mrs. Suguna Adyanthaya, from the lab, was a very resourceful help during the research period. I would like to thank her for all that she has done.

I owe my gratitude to the staff members of our division, who have helped me in innumerable way, especially Mr. Deepak and Mr. Punekar. I am grateful to many people in the Center for Materials Characterization, NCL who have assisted me in the course of this work, specialthanks to Gholapji.

I am grateful to Dr. S. Sivaram, Director NCL, for giving me an opportunity to work in this laboratory and making the facilities available for carrying out research. I acknowledge the Council of Scientific and Industrial Research (CSIR), Government of India for providing me with the necessary funding and fellowship to pursue research at NCL. I am also grateful to DST & NCL for providing me with the financial support for presenting my work at an international conference (GOLD 2009) at Heidelberg, Germany.

I am highly indebted to some of friends, like Dr. Murugaiyan, who have been with me during rough times and guided me through the storm. Ms. Sandra, Dr. Veer Bhadur Singh (Vicky), Dr. Atul Kumar, Ms. Meera Singh, many thanks to you. Friends like Saumya, Aejazur, Dr. Pavithra, Dr. J. P. Singh have also be helpful and I express my gratitude to them. Many thanks to Ms. Renu Singh who has been a great help during the final stages. Additionally, I'm indebted to many whose name may not be here, yet, who has been instrumental in any small way to aid in my work.

Last, but not the least, family always backs you in all your endeavours. Needless to say, this would not be possible for me without my family.

Ramya Jagannathan Dwivedi

DECLARATION BY THE RESEARCH GUIDE

Certified that the work incorporated in the thesis entitled: "**Surface functionalisation of nanoparticles and their biological applications**", submitted by Ms. Ramya Jagannathan, for the degree of Doctor of Philosophy, was carried out by the candidate under my supervision at the Division of Biochemical Sciences and Physical and Materials Chemistry Division, National Chemical Laboratory, Pune. Materials acquired from other sources have been duly acknowledged. To the best of my knowledge, the present work or any part thereof has not been submitted to any other University for the award of any other degree or diploma.

Dr. (Mrs.) Asmita. A. Prabhune
Research Guide

Date:
Place:

DECLARATION BY THE RESEARCH CO-GUIDE

Certified that the work incorporated in the thesis entitled: "**Surface functionalisation of nanoparticles and their biological applications**", submitted by Ms. Ramya Jagannathan, for the degree of Doctor of Philosophy, was carried out by the candidate under my supervision at the Division of Biochemical Sciences and Physical and Materials Chemistry Division, National Chemical Laboratory, Pune. Materials acquired from other sources have been duly acknowledged. To the best of my knowledge, the present work or any part thereof has not been submitted to any other University for the award of any other degree or diploma.

Dr. Pankaj Poddar
Research Co-guide

Date:
Place:

DECLARATION OF THE CANDIDATE

I hereby declare that this thesis entitled "**Surface functionalisation of nanoparticles and their biological applications**" is entirely original and was carried out by me under the supervision of Dr. Asmita A. Prabhune in the Division of Biochemical Sciences, NCL, Pune and Dr. Pankaj Poddar in the Materials and Physical Chemistry Division, NCL, Pune. Any material borrowed from other sources has been duly acknowledged. I further declare that this material presented here has not formed the basis for the award of any degree or diploma of any University or Institution.

Ramya Jagannathan
(Ph.D. candidate)

Date: January 2010
Place:

ABSTRACT

CHAPTER 1: INTRODUCTION

This chapter is an introduction to the research work presented in this thesis. It begins with a bird's eye view of the field of nanoscience and nanotechnology, covering from its history to the latest development. The chapter proceeds to describe surface functionalisation and its importance, different types of functionalisation and its applications in biology.

CHAPTER 2: EXPERIMENTAL PROCEDURES

This chapter comprises of an overview of all the techniques used in this thesis work, their principle, instrument and working specifications and their uses.

CHAPTER 3: PART I- FUNCTIONAILSATION OF GOLD NANOPARTICLES WITH ANTIBIOTICS; PART II- IRON OXIDE NANOPARTICLES AS ENZYMATIC BIOSENSORS

Recently, we reported a novel synthesis route where we used an antibiotic cephalexin to reduce chloroauric acid. In this method colloidal gold capped by antibiotic in aqueous solution is readily prepared by a facile one-pot protocol. We have shown by a detailed investigation based on nuclear magnetic resonance and X-ray photoemission spectroscopy results, that the sulfur moiety present in the beta lactam is responsible for the dual role of reducing and capping (stabilizing) the gold nanoparticles. Interestingly, in this method, we could control the morphology of the gold nanoparticles from quasi-spherical to flat triangular flakes and finally to truncated triangles and hexagons by increasing the concentration of gold ions correspondingly. In yet another remarkable result in our earlier study, the transmission electron micrograph also showed the presence of a large number of smaller 1-3 nm particles. However, in the absence of any other supporting information to validate the presence of these particles, authors did not comment on the origin of these smaller structures in the c images. We believe that this synthesis route is a perfect model system to study the growth of the gold nanoparticles, which is elaborated in following chapter.

Also, in a different study of functionalisation, chemically synthesized iron oxide nanoparticles are functionalised using the commercially important enzyme Penicillin G acylase as a means for immobilization and ease of separation after reaction with the substrate.

CHAPTER 4: NUCLEATION AND GROWTH OF GOLD NANOPARTICLES

The unusual nucleation and growth kinetics of gold nanoparticles synthesized in the presence of the antibiotic cephalexin using *in situ* static and dynamic light scattering in conjunction with *in situ* UV-vis absorption measurements and transmission electron microscopy is reported in this chapter. Following a brief latency period, two well-separated populations of gold nanoparticles, with average sizes of 1-2 nm versus several tens of nanometer, respectively, nucleate simultaneously. For either size regime, the total number of particles increased rapidly, while their mean size and relative frequency remained essentially constant over a growth period of 5 h. With increasing temperature, the morphology of the larger nanoparticles became increasingly spherical, as indicated by the noticeable blue shift of the plasmon frequency for these particles. The detailed morphology for either particle population was confirmed with transmission electron microscopy. This is the first observation of simultaneous growth of two distinct populations of crystalline nanoparticles in the solution phase. The coupled growth of two distinct populations of nuclei, their tight control of size but rapid increase in overall numbers present novel and intriguing facets of this antibiotic-mediated solution-growth of gold nanoparticles. The size evolution of the Mie-frequency exhibits a noticeable blue shift as the temperature increases, correlating with the roundness of the particle/bimodal distribution.

CHAPTER 5: *SOLUBILISING CURCUMIN, SYNTHESIZING GOLD NANOPARTICLES AND THEIR ANTI-OXIDANT PROPERTY*

Curcumin is a phytochemical that gives yellow color to turmeric and is responsible for most of the therapeutic effects of turmeric. The keto-enol-enolate equilibrium of this heptadiene-dione moiety determines its physiochemical and antioxidant properties. Solubility of curcumin is very low in water at neutral pH and room temperature. The mechanism behind its solubility issues at various temperatures and the influence of interplay of temperature and intra/intermolecular H-bonding in curcumin leading to aggregation-disaggregation in various temperature regions is investigated. A remarkable change in the temperature dependent electronic transition behavior of the molecule in water is observed. The study indicates that it is perhaps the breaking of the intra-molecular hydrogen bonding which leads to the exposure of the polar groups and hence responsible for the dissolution of curcumin at higher temperature. We believe that formation of inter-molecular aggregates might be responsible behind a better room temperature stability of the molecules after cooling its aqueous suspension from 90 ºC to 25 ºC.

The synthesis of gold nanoparticles using curcumin in water around 90 °C is carried, thereby increasing the possibility of enhancing the bioavailability and drug-action. In this method

curcumin acts both as a reducing agent and as a capping agent. The nanoparticle size (~20 nm) is quantified by transmission electron microscopy. The synthesized nanoparticles are very stable and show good anti-oxidant activity.

SUMMARY

The summary reflects the salient features of the work presented in the thesis and emphasizes on potential avenues for future research work in this field.

ABBREVIATIONS

µM	Micromolar
µm	Micrometer
6-APA	6-Amino Penicillanic Acid
7-ACA	7-Amino Cephalosporinic Acid
AFM	Atomic Force Microscopy
B.E.	Binding Energy
CNT	Carbon NanoTubes
DLS	Dynamic Light Scattering
DPPH	2,2-diphenyl-1-picryl hydarzyl
ESCA	Electron Spectroscopy for Chemical Analysis
eV	electron Volts
fcc	face-centered cubic
FTIR	Fourier Transform Infra-Red
h	Hours
hC	half Curcumin, 4(4-hydroxy-3-methoxyphenyl)-3-buten-2-one
HPLC	High Performance Liquid Chromatography
HRTEM	High Resolution Transmission Electron microscopy
IME	IMmobilized Enzymes
IR	Infra-Red
IU	International Units
LSPR	Localized Surface Plasmon Resonance
LSPRR	Localized Surface Plasmon Polariton Resonance
min	Minutes
MRI	Magnetic Resonance Imaging
NCIM	National Center for Industrial Microorganisms
ng	Nanogram
nM	Nanomolar
nm	Nanometer
NMR	Nuclear Magnetic Resonance

NP	Nanoparticles
PBP	Penicillin-Binding Proteins
PDAB	p-dimethylaminobenzaldehyde
Pen G	Penicillin G
PGA	*Pencillin G Acylase*
SAED	Selected Area Electron Diffraction
SAM	Self Assembled Monolayer
SAXS	Small Angle X-ray Scattering
SEM	Scanning Electron Microscopy
SLS	Static Light Scattering
SPR	Surface Plasma Resonance
STM	Scanning Tunneling Microscopy
TAE	tris acetate EDTA buffer
TEM	Transmission Electron Microscopy
TGA	Thermo Gravimetric Analysis
TOPO	tri octyl phosphine oxide
UV-Vis Spectroscopy	Ultraviolet-Visible Spectroscopy
XPS	X-ray Photo Emission Spectroscopy
XRD	X-Ray Diffraction

I dedicate this work to my father, my mother & my brother…

who taught me my lessons and the truth, for influencing the road not taken, for affection

And to my husband…

who is travelling with me on this journey to the pinnacle and to the abyss and to the pinnacle and to the abyss…

"The grandest idea in the religion of the Vedanta is that we may reach the same goal by different paths; and these paths I have generalized into four, viz those of work, love, psychology and knowledge"

Swami Vivekananda

INTRODUCTION

Chapter 1

This chapter is an introduction to the research work presented in this thesis. It begins with a bird's eye view of the field of nanoscience and nanotechnology, covering from its history to the latest development. The chapter proceeds to describe surface functionalisation and its importance, different types of functionalisation and its applications in biology.

1.1. Introduction

Nanomaterials are built through the assembly of nanometer-scale units into ordered super lattices and they offer exciting perspectives as novel materials whose optical, electronic, magnetic, transport, mechanical and thermodynamic properties may be controlled by the selection of the composition and sizes of the building-block units and that can be made further use of.[1] The work reported in this thesis is an endeavor towards that explained in the previous sentence. This chapter is a brief introduction to the research work presented. It begins with the definition of 'nanotechnology' and its birth, elaborating on why it is so important. The advent and ongoing development of technology has aided in studying these particles which though have been in existence since time immemorial, could be researched closely only in this generation of science. The properties of the nanomaterials are followed by an outline of the various synthesis procedures, its applications and the health risks involved in introducing them into the environment. The science of surface functionalisation of nanoparticles is explained with different types and their applications in various fields, with due emphasis in biology. The objective of the thesis and an outline of the thesis are provided at the end of this chapter.

1.1.1. Profile of nanoparticles

Nanomaterials have been in existence in nature for long; much before the famous address by Richard P. Feynman, Professor of Physics at the California Institute of Technology and Nobel Laureate, in 1959, at the American Physical Society, which is published in *Engineering and Science*, entitled "Plenty of Room at the Bottom".[2] For example, nano-sized gold and silver has been used in glass to tint them for ages and carbon black (10 to 400 nm sized carbon particles) has been in use as fillers for automotive tires for more than 100 years. However, the era of '*nano*' began in the last century and the achievements of the challenges posed by Prof Feynman proved his prophecy true. In 1960, William McLellan constructed a small motor by hand using tweezers and a microscope and in 1985, Thomas Newman wrote the first page of Charles Dickens' *A Tale of Two Cities* using a computer controlled finely focused pencil electron beam on an area of 5.9 micrometers square.[3] Nanoscience and nanotechnology, ever since, has been an explosion of understanding, designing and fabricating new nanomaterials for applications of interest, in any field. With the

advancing technology that helped make breakthroughs in the field of microscopy, which made the burgeoning field feasible, scientists witnessed the dawn of a new era. TEM, SEM, STM and AFM are those tools with which the study at a scale of nanometers is carried out and every field on earth is influenced. A nanometer is the equivalent in size of ten hydrogen atoms and one-millionth the diameter of the head of a pin.[3]

On the website of US National Science Foundation, nanotechnology is defined as research and technology development at the atomic, molecular or macromolecular level, in the length scale of ~1-100 nm range, to provide a fundamental understanding of phenomena and materials at the nanoscale and to create and use structures, devices and systems that have novel properties and functions because of their small and/or intermediate size.

1.1.2 What are these nanoparticles and why are they so important?

The word '*Nano*' meaning dwarf in Greek is already in the market on the wide range of applications. As the definition above, systems in which the dimensions measure in the range of nanometers are covered under the large canopy of the nanoscience and nanotechnology. The nanoscience and nanotechnology has taken an upswing over the frontiers in scientific research. The nanoparticles can be of different types comprising of metal or metal oxide nanoparticles, organic/inorganic nanoparticles, quantum dots, polymeric nanoparticles, liposome, DNA machines, and carbon nanotubes (CNT), graphene, etc.

Nanoscience and nanotechnology thus encompass a range of techniques rather than a single discipline and stretch across the whole spectrum of science, touching medicine, physics, engineering and chemistry. The gap between the physics/chemistry of atoms/molecules and bulk materials/condensed matter is bridged by a broad slope (See Figure 1.1) and not a fall as shown in red; it reflects both the geometric and delocalized electronic shell structures of the clusters of atoms or molecules. Chemists may prefer to think of small nanoparticles as clusters of molecules.

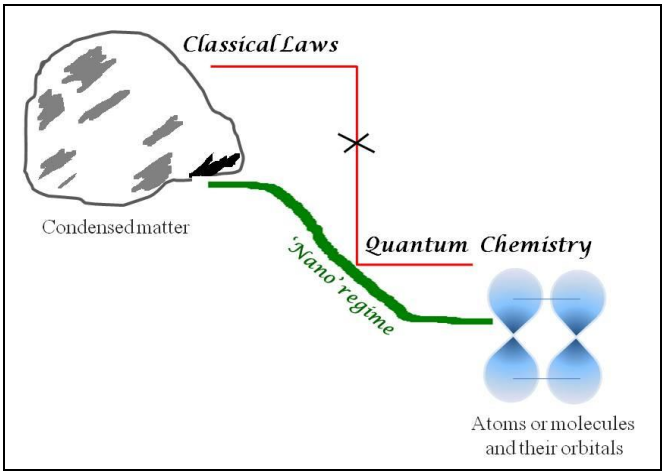

Figure 1.1. Cartoon representing the gap between the bulk and molecular species, where the 'nano' regime reigns.

The broad slope is characterized by the size-dependent variations in the matter, which determines the physical and chemical properties of the system involved. Quite often, the discontinuous behavior of quantum size effects is superimposed on a smoothly scaling slope which also reflects the size of a quantized system.[4] The intense research in the field of nanoparticles by chemists, physicists and materials scientists is motivated by the fundamental question of how molecular electronic properties evolve with change in size in this intermediate region between molecular and solid-state physics. To elaborate, the size variations involved are in the range of a few hundreds to few nanometers, which is illustrated in the representation, Figure 1.2. The change in properties can be explained in the following section, size-dependent effects.

1.1.2.1 Size-dependent effects

It is important to understand the process of size quantization or quantum confinement before plunging into more about nanoparticles. The unusual properties of nanoparticles are primarily due to confinement of electrons within particles of dimensions smaller than the bulk electron delocalization length. This process is known as quantum confinement.[5, 6] In the size regime of a few nanometers, the boundaries of the crystallite are comparable in dimension to the wavelength of electrons in the extended solid. As a consequence, the optical and electrical properties of the nanocrystals are dominated by quantum effects. Size quantization refers to changes in the energy-level structures of materials as the material-unit (most

often a crystal) size drops below a certain size. This size, which can be identified with the Bohr diameter of the material, can vary from almost 100 nm to a single nanometer or even less.

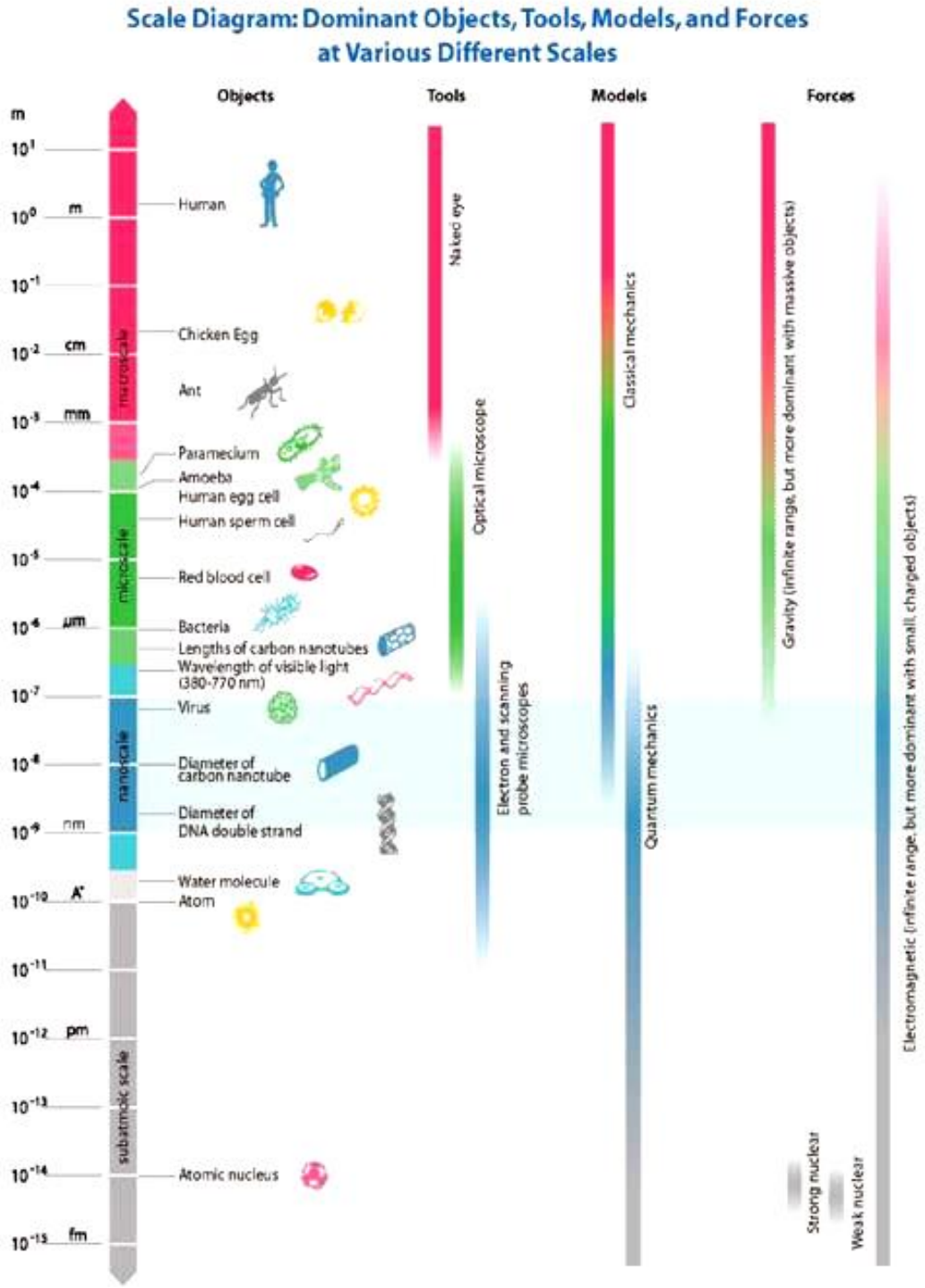

Figure 1.2. Size comparison ranging from atomic nucleus to man. [Adapted from ref [7]]

For metals, it is smaller than a few tens of nanometers. For gold clusters, it is approximately 1 nm (often less than 100 atoms). Size quantization is characterized by an increase in band gap (blue-shift in optical spectra) and increasing separation of energy levels with decrease in crystal size. (see Figure 1.3) As the energy-level structure changes continuously with change in crystal size (in the size-quantization regime), a material of a particular fixed chemical composition can be made with varying and tunable physical properties.[8]

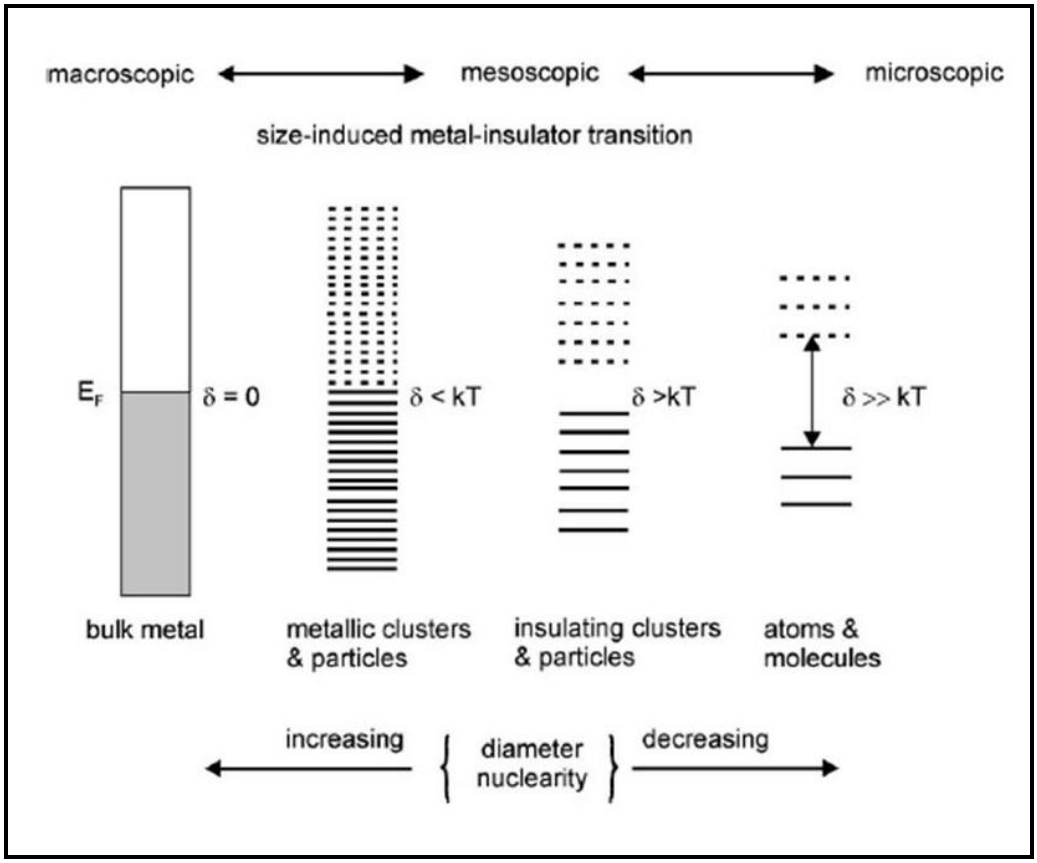

Figure 1.3. Evolution of the band gap and the density of states as the number of atoms in a system increases (from right to left). d is the so-called Kubo gap. (Adapted from ref [4])

Thus, the basic material properties are determined by both the physics of the material and its chemistry. In addition to the quantum size effects, the surface effects also affect the physical & chemical properties of the materials, which is discussed in the following section.

1.1.3 Properties of nanoparticles

Colloidal nanocrystals are sometimes referred to as 'artificial atoms' because the density of their electronic states — which controls many physical properties — can be widely and easily tuned by adjusting the crystal's composition, size and shape.[9] The physical and chemical properties of nanoparticles can be tuned over a range by variation of the particle size. Depending upon which new properties arise such as quantum confinement, plasmon excitation, superparamagnetism, the Coulomb blocking effect, etc. The optical properties of nanoparticles, especially metal nanoparticles, have been of great interest. [10-13] The strong color of the colloid of the noble metal nanoparticles is caused by the surface plasmon absorption. Surface Plasmon Spectroscopy is a versatile technique for studying chemisorptions, redox reactions, (bio) sensing, alloying, and electrochemical processes such as under potential deposition involving small metal nanocrystals that exhibit well-defined surface plasmon modes.[14] This includes Au, Ag, Cu, Sn, Pb, Hg, Cd, In and the alkali metals.[15] Many metals such as Sn, Pb, Hg, Cd and In have plasma frequency in the UV part of the electromagnetic spectrum and thus the nanoparticles do not display strong color effects. Moreover, such small metal particles also get readily oxidized making surface plasmon experiments difficult. However, the coinage elements like Au, Ag and Cu are exceptional: (1) they are noble and form air-stable colloids and (2) due to d-d band transitions, the plasma frequency is pushed into the visible part of the spectrum. For ages, the 'soluble' Au and Ag have been in use for the exhibition of their unique colors. For example, the first optical metamaterial is the ruby glass, which contained tiny gold droplets, typically 5-60 nm in size.[16] As demonstrated by the exquisite Lycurgus Cup (see Figure 1.4) these gold particles color the glass in an extraordinary way. In daylight the cup appears a greenish color, but illuminates it from the inside and it glows ruby.

Figure 1.4. Lycurgus Cup (British Museum; AD fourth century) [Adapted from ref[16]]

It appears green when viewed in reflected light, but looks red when a light is shone from inside and is transmitted through the glass. Analysis of the glass reveals that it contains a very small amount of tiny (~70 nm) metal crystals containing Ag and Au in an approximate molar ratio of 14:1. Bulk Au looks yellowish in reflected light, but thin Au films look blue in transmission. This characteristic blue color steadily changes to orange, through several tones of purple and red, as the particle size is reduced down to ~3 nm. The surface plasmon resonance and its effects are explained in Chapter 4.

Small crystals require lower melting temperature and the scaling laws in the nanometer regime is driven by the fact that in this regime, the liquid phase has lower surface energy than a solid with facets, edges and corners.[17] The effect can be quite significant, leading to a halving of the melting temperature for a solid particle of 2–3 nm diameter relative to that of the corresponding bulk solid. Melting is a cooperative phenomenon which is not well defined for a small number of members of the ensemble like nanoparticles.[4] A sharp melting point is only obtained in the thermodynamic limit of an infinite number of particles as is the case in a bulk material. For the nano regime, melting points are broad and size-dependent. Thus we find changes in the melting point as we go from bulk to nano. It is known that the

atoms or molecules at the surface layers suffer lower stabilization due to less coordination as compared to the interior. The extrapolation of this fact to the nanoparticles, explains the size-dependence of the melting point of the same material. The Gibbs-Thomson equation describes how the melting point scales inversely with the radius of the particle[18]:

$$\frac{T_m - T_m^*}{T_m^*} = \frac{\Delta T_m}{T_m^*} = \frac{2\, V_m\,(l) \Upsilon_{sl}}{\Delta H_m r}$$

where, *Tm* is the melting point of the cluster with radius *r*,

*Tm** is the melting point of the bulk,

Vm(l) the molar volume of the liquid,

Υ_{sl}, the interfacial tension between the solid and the liquid surface layer, and

ΔHm is the bulk latent heat of melting.

Also, the catalytic activity of the nanoparticles is well established, for example, the excellent catalytic activity of small gold particles, which is an inert metal in the bulk state, is known.[19] The selectivity, however, is most sensitive to the packing of atoms on the surface or the exposed facets of a nanocrystal.[20, 21]

The weak intrinsic fluorescence of noble bulk metals (quantum yield ~10^{-10}) results from the electronic inter-band transition.[22] Nanorods also have enhanced emission over bulk metal and nanospheres, due to the large enhancement of the longitudinal plasmon resonance.

Elements that are non-magnetic at bulk state become magnetic at nano-size. Nanoparticles comprising several hundred atoms of Au, Pd and Pt embedded in a polymer revealed magnetic moments corresponding to several unpaired electron spins per entire particle.[23, 24] The magnetic properties of iron oxide nanoparticles is discussed in Chapter 3 (Part II).

1.1.4. Synthesis of nanoparticles and its applications

The most challenging part of research in the field of nanoscience & nanotechnology is the cost effective and environmentally safe procedures for synthesizing the desired nanomaterials. Of the two distinct synthesis procedures, (1) top-down approach and (2) bottom-up approach, the latter is more effective and hence commonly used. (see Figure 1.5) The top-down approach has been developed from ancient methods like lithography, writing or stamping. Now the top-down approach is capable of creating

features down to the sub-100 nm range, using sophisticated tools like electron-beam writing, advanced lithographic techniques using UV or hard X-ray radiation [25] and techniques like microcontact printing. [26] In contrast, bottom-up methods aim to guide the assembly of atomic and molecular constituents into organized surface structures through processes inherent in the manipulated system. The bottom-up approach is inherently non-equilibrium phenomenon and the growth scenario is governed by the competition between kinetics and thermodynamics of the reaction.

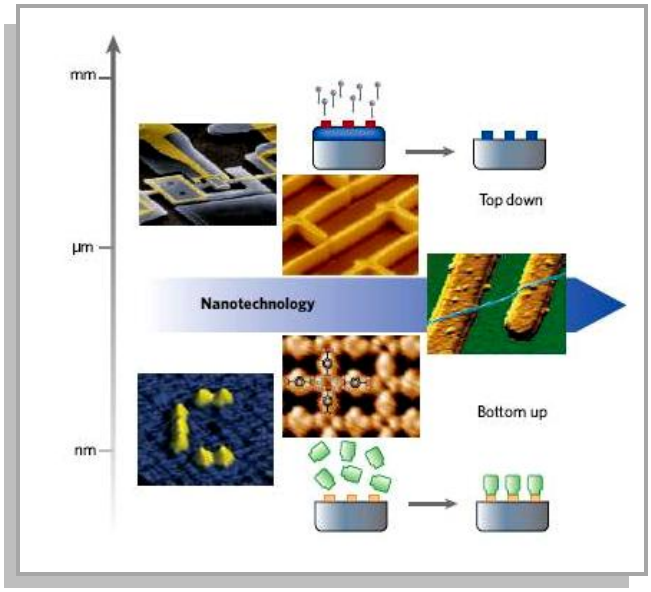

Figure 1.5. Two different approaches to control matter at the nanoscale. [Adapted from ref[27]]

In this thesis, we have used bottom-up approach to synthesis nanoparticles from metal-ions in solution phase. The synthesis system consists of the typical three components: precursors, organic surfactants and solvents. Upon crossing the threshold of the activation energy (by means of temperature, catalyst or active chemical like a reducing agent), the precursors chemically transform into active atomic or molecular species (monomers); these then form nanocrystals whose subsequent growth is greatly affected by the presence of surfactant molecules.

The formation of the nanocrystals involves two steps: nucleation of an initial 'seed' and growth. During nucleation, precursors form a supersaturation of monomers followed by a burst of nucleation of nanocrystals.[9] These nuclei then grow by incorporating additional monomers still present in the reaction medium, until all of it is exhausted.

In our work, the metal ions are reduced by a reducing reagent in solution; they nucleate to form clusters and grow into nanoparticles while in the presence of protective ligands. Either the stoichiometry of the available metal ion supply or the passivation of further growth by the protective ligands, in combination with numerous other parameters like the temperature, osmotic potential, dilution factor, stirring rate, etc. can determine the eventual nanoparticles size. Reduction of $HAuCl_4$ by boiling sodium citrate solution to obtain spherical gold nanocrystals is one of the most popular methods of synthesizing gold nanoparticles.[28, 29] There are numerous methods in wet-chemistry to synthesize gold, silver, platinum nanoparticles, etc. In fact, the synthesis procedures have reached the stage of controlling various parameters (such as size, shape, crystallinity, composition) to achieve control[9] and to fine-tune the properties of the nanoparticles.[30] To obtain well-defined structures, tailored syntheses of colloidal nanocrystals are available, such as co-precipitation in aqueous phase, using reverse micelles as templates, hydrothermal/solvothermal synthesis and surfactant-controlled growth in a hot organic solvent.[31, 32] Depending on the ratio of the salt and capping agent, the particle size can be tuned.

Xiaogang Peng et al[33] in his paper conclude suggesting that the continuous monitoring and adjustment of the monomer concentration provides an optimal growth sequence, so that the average size present is always just slightly larger than the critical size, for reproducibly and reliably large amounts of uniform size. Figure 1.6 in the following page shows the narrow distribution achieved in their work.

Phase transfer[34, 35] and ligand exchange reactions[36, 37] are other methods of synthesis. Complex morphologies such as dendritic heterostructures have been produced in colloidal nanocrystals synthesis (CdSe on CdTe).[38] To name a few breakthroughs in the synthetic procedures, read the following. The 'Nano-filling method' is a unique way of synthesizing stable nanowires. Confinement of electrons in one or more dimensions to show unique quantum properties is essential for nanoelectronics devices. However, nanowires of few atoms thick are structurally and chemically unstable. Ryo Kitaura and co-workers have shown that ultrathin metal nanowires can remain stable for long periods if they are grown inside carbon nanotubes.[39, 40]

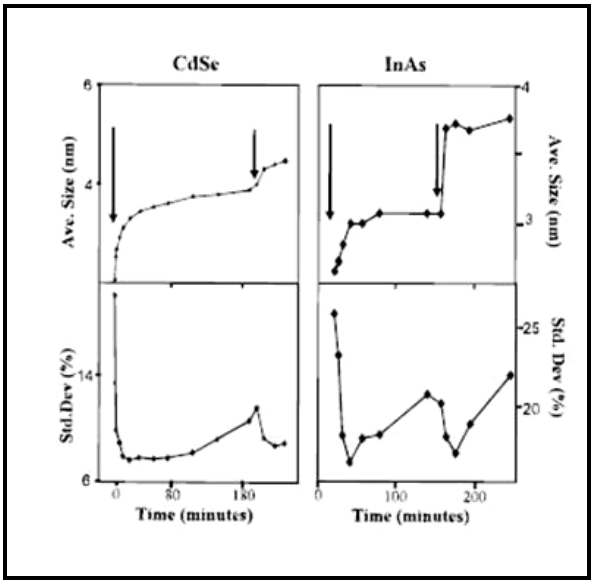

Figure 1.6. The mean size and the size distribution. [Adapted from ref[33]]

Multi-walled Carbon Nano-Tubes (CNT) are found to penetrate tomato seeds and accelerate sprouting process. The seeds treated with CNTs grew faster, with larger biomass and longer stems[41]. This opens up new approaches for delivery agents in agriculture and horticulture and new avenues in bio-fuel research.

Optomechanical crystals have been created that can act as both photonic and phononic crystals, allowing light and sound to be confined within a small region.[42, 43] This kind of research is a combination of art permeating science. (Figure 1.7.)

The advent of quantum dots has revolutionized the imaging and analysis field of biological samples, by overtaking the organic fluorophores. The quantum dots do not photo-bleach; they give better results with high resolution and also provide a readily accessible range of colors. The quantum dots and rods are also used as alternatives to semiconductor polymers in light emitting diodes[44], lasers[45] and solar cells.[46]

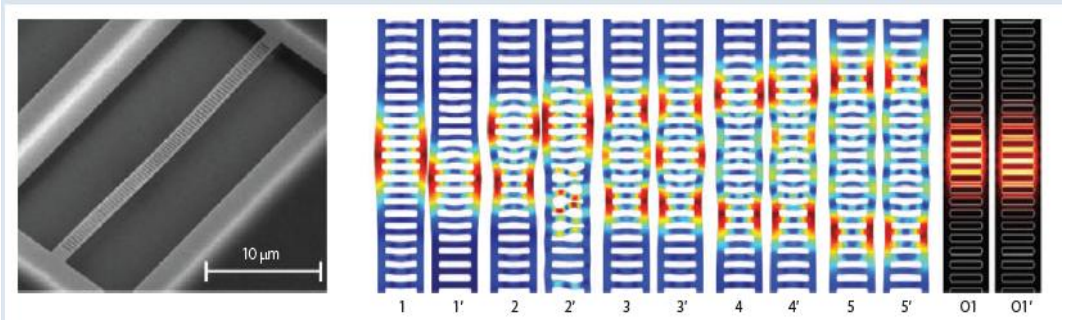

Figure 1.7. Optomechanical crystals; periodic nanobeams bring light and sound together.

Chromophores within ~5 nm of the surface of the metal nanoparticle have their fluorescence quenched while chromophores at distances of ~10 nm or greater have their fluorescence enhanced up to 100-fold. The electric field of the metal nanoparticle is still near enough to influence the fluorescence and enhance it, but cannot interact directly with the chromophores electrons and quench it. Working to improve the performance of lithium-ion batteries, it is shown that energy storage can be improved by building the battery anode from silicon nanotubes.[47] Likewise, the applications of nanoparticles in various fields is innumerable and still increasing magnanimously.

1.1.5. Nanoscience, nanotechnology and risks

Concerns arise in this cross-disciplinary area about toxicological aspects and ethical implications. One can find nanoparticles in day-to-day uses, such as sunscreens, toothpastes, sanitary ware coatings and even medicines and food products. According to Dan M. Kahan,[48] there exists a reciprocal link between the development of nanotechnology and research into public perceptions of risk. Also, an increase in knowledge does not result in reduced aversion to risks.[49] Hence addressing the health risks and environmental effects is an important part of 'nano' research. This section gives a brief summary of the risks and effects mentioned. The actual health risk will depend not only on the intrinsic hazard of the agent but also on the likely exposure. With the rise in wide interests and faceted applications, the nanoparticles production has increased tremendously from multi-ton carbon-black and fumed silica for applications in plastic fillers and car tires to microgram quantities of fluorescent quantum dots used for markers in biological imaging.[50]

The nanoparticles could affect at the molecular, cellular, physiological levels and attack the organs as well. For example, the schematic below shows the possible routes a nanoparticle can take within the lung aided by the fluid present in the pleural space, which lubricates the movement of lungs. (Figure 1.8.)

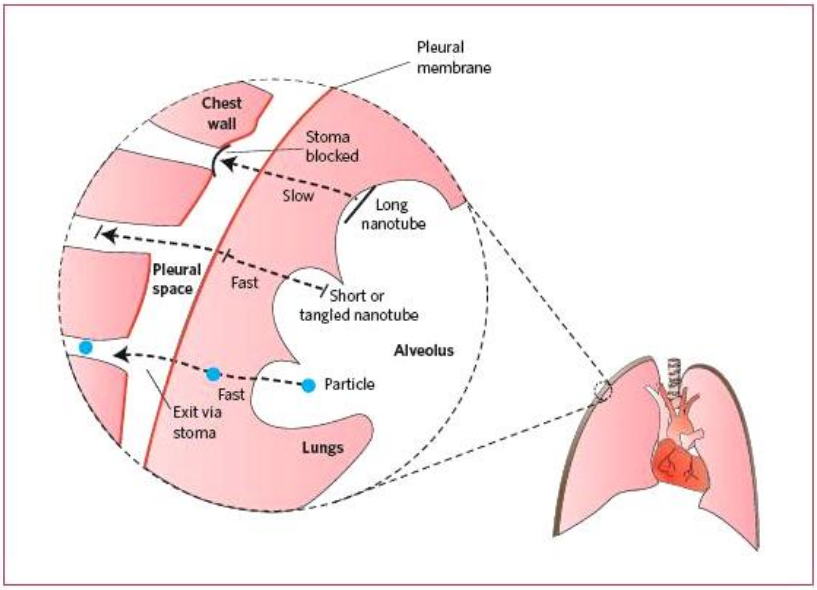

Figure 1.8. Movement of particles through the lungs. [Adapted from ref[51]]

Small particles and short nanotubes move rapidly and drain easily through the pores, whereas long and fibrous nanotubes get lodged at the drainage points and block. This causes to inflammation leading to pathological changes over time.[51] Strong immune and inflammatory responses are already detected when using nanoparticles in different mammalian systems.[52-56]

Evidences suggest that the key factors contributing to nanomaterials related cytotoxicity are size/mass (size distribution), shape, surface area, chemical composition (purity, crystallinity, electronic properties, etc.), solubility and stability, bio-persistence, surface charge and surface functionalisation. The paucity of sound data renders it premature to formulate any definitive risk assessment about engineered nanomaterials; therefore, several other important issues require close attention.[50]

1.2. Surface functionalisation of nanoparticles

Surface functionalisation of nanomaterials holds the potential for creation of new materials and new applications. After the synthesis of the colloidal particles, further modifications are necessary to stabilize the particles against aggregation[57, 58]; the modifications enable easy use, depending upon the requirement of the application. Different interactions may be then controlled through the process of surface 'functionalisation' (or 'derivatization') as explained below.

1.2.1. Science of surface functionalisation

The inorganic cores possess useful properties that are controlled by their composition, size and shape, and the surfactant coating ensures that these structures are easy to fabricate and process further into more complex structures.[9] Synthesis of the nanomaterials requires passivation of the surfaces to protect against modifications of their properties by their environment and to inhibit their propensity to agglomerate or sinter. Through its chemical interaction with a metal surface, the presence of a capping agent can change the order of free energies for different crystallographic planes, and thus their relative growth rates. The plane with a slower addition rate will be exposed more on the nanocrystal surface.[59] Organic surfactant molecules in the growth medium are chosen for their obsolete nature to adhere to a growing crystal. More than half the atoms of the nanocrystals may be present on the surface and this makes growth strategy at the inorganic-organic interface pivotal.[9] That is how in nature, the biomineralisation, where the complex patterns of biologically organized organic functionalities control the temporal and the spatial arrangement of some inorganic solids.

One of the most elegant passivation routes is through self-assembly, that is spontaneous formation of passivating monolayers.[1] It is well known that immersion of coinage metals such as gold, silver and copper in organic solutions of alkanethiols results in the spontaneous assembly of densely packed monolayers, termed the 'self-assembled monolayers' or SAMs, of the alkanethiols on the substrate surface.[60] The surface functionalisation involves in the control of the interactions between the particles and a host medium, a substrate or other individual species like molecules, other particles or biological systems. This control is usually achieved through the process of functionalisation of the nanoparticles, which consists of grafting

molecules onto their surfaces with specific chemical functions. These functions may be chosen either

(i) to just ensure the stabilization of the particles by playing on dispersion forces, or

(ii) to allow their binding to more or less specific sites of the target substrate.[61]

1.2.2. Different types of surface functionalisation

Inorganic nanoparticles such as gold, silver, CdS etc. can be stabilized with ionizable groups such as carboxylic acids and amine groups. ω-functionalized thiol derivatives are normally used to modify the surface of noble metal and metal sulfide quantum dots. The thiol groups are known to chemisorb on such nanoparticle surface while the terminal ionizable or long chain functional groups enable stabilization of the particles via Coulomb and steric interactions.

Depending upon the chemical nature of the surface of the nanoparticle, a different number of variants of the technique is used for the assembly of inorganic ions, bio-macromolecules (proteins and DNA), and inorganic nanoparticles at the air-water interface.[62] A few examples of organic surfactants are alkyl phosphine oxides, alkyl phosphonic acids, alkyl phosphines, fatty acids and amines, and some nitrogen-containing aromatics. These molecules all contain metal coordinating groups as well as solvophilic groups. The former group is typically electron-donating to allow co-ordination to the electron-poor metal atoms at the nanocrystals surface. This prevents further growth and aggregation.[9]

Hydrophobic nanoparticles may simply float on the surface of the water, compressed into a close-packed monolayer and transferred onto suitable solid supports by the versatile Langmuir-Blodgett methods, using the Coulomb or electrostatic interactions in the nanoparticle (such as silver, gold, semiconductor quantum dots such as CdS and CdTe, oxides such as SiO_2, TiO_2, Fe_3O_4, and γ–Fe_2O_3 and latex spheres) assembly at the air-water interface. [62]

To further derivatize the nanocrystal surface, introduction of other competing ligands is also possible, through surfactant exchange; allowing the introduction of a wide range of possible chemical functionalities. This strategy has the additional advantage for chemical manipulation of the nanocrystals properties which is sensitive to the

nature of the functionalized surface coating.[63] One of the most popular soft lithographic techniques applications for creating patterned structured in SAMs is based on micro-contact printing (μCP).[64] For sub-micron ranges silicon chips, photolithographic techniques are used; the pattern in the photo-resist is generated by light exposure through a mask followed by chemical development, transferred into thin films of immobilized molecules.[65] The process of immobilization or functionalisation is in itself a large science which in turn is determined by the applicability.

Thus, functionalisation of various nanosystems provides various means to link them to other surfaces and biomolecules.

1.2.3. Applications in biology

Functionalizing biomolecules on surfaces have applications that range from medical diagnostics, analytical chemistry, and culturing and studying cells on surfaces, to synthesizing or engineering useful biomolecules.[66] A Lab-on-a-Chip device is a combination and integration of fluidic elements, sensor components and detection elements to perform the complete sequence of a chemical reaction or analysis, including sample preparation, reactions, separation and detection.[66] Modifications of the surface of this device are essential for the designed functionality. These include modifications of wetting characteristics (hydrophobic/hydrophilic), increased biocompatibility, reducing or eliminating solute interactions, changing the electro-osmotic flow, immobilizing the reagents, enzymes, antibodies, proteins, DNA, etc. to carry out chemical reactions or detection mechanism, or to provide a proper surface for immobilization, increasing the surface area for catalytic reactions, and tethering sieving matrices or stationary phases for separation devices.[66] The enhanced scattering cross section of metal nanoparticles due to surface field effects can be used as a powerful technique to image biological systems. Functionalizing gold particles with antibodies, such as anti-EGFR antibody, El-sayed *et al.*[67], are able to distinguish between cancer and non-cancerous cells.

Of all the applications of nanoscience in biology, medicine forms the major thrust, in terms of impact and utilization.[68] The design of multilevel molecular aggregates at nano- and meso- levels that have novel functional and dynamic properties (size-dependent and site-specific) are desirable for applications in medicine. Moreover,

nanomedicine forms the stepping of a highly modernized form of personalized medicine.[69] Miniaturization, parallelization, integration, as well as automation, along with speed, convenience, accuracy and low cost are mandatory and this can be consummated in nanomedicine. Kristina Riehemann et al. [68] discuss the diagnosis, analysis methods, therapy, research and development using nanomedicine. In addition to the developments in medical science and technology, progress in materials science definitely helps progress in medical device technology. The implants used in medicine interact with a highly sophisticated manner through its surface; hence biocompatibility is an important parameter to be considered seriously while designing an implant. The following two examples exemplify the importance of surface functionalisation as well as the application of nanobiotechnology.

The technology used in developing an implantation stent (used in combating vascular diseases and myocardial infarction) with the anti-proliferative drug, using nanoporous alumina membrane has saved millions of lives to date. The surface of the stent has to be functionalized accordingly using biocompatible material and drug storage-release capacity. Similarly, implantation of seeds containing radioactive nuclides (such as ^{125}I and ^{103}Pd) to irradiate tissues locally in cancers or to irradiate the restenotic area[70], uses nanostructure implant surfaces, that are safe, with the system acting as a nano test tube producing homogeneous activity.

1.3. Outline of the thesis

The thesis consists of 5 chapters.

- The *second chapter* describes the experimental procedures used in the research work for characterization and analysis, presented in this thesis. The principle, theory and working specifications are outlined with suitable diagrams wherever necessary.
- The *third chapter* describes the study of (i) gold nanoparticles synthesized by antibiotics like cephalexin, cefaclor and ampicillin and (ii) iron oxide nanoparticles capped by enzyme Penicillin G acylase. The synthesis, characterization and biological activity of these nanoparticles are discussed here.
- The *fourth chapter* describes the capturing of gold nanoparticles during its synthesis by the antibiotic cephalexin using optical methods like Dynamic Light Scattering (DLS) and Surface Plasmon Resonance using UV-Vis light spectroscopy.

These methods are elaborated for a better understanding. The data is supported by TEM micrographs and SAED pattern. Unique bimodal distribution is observed at different temperatures (15 °C, 25 °C & 35 °C) using DLS. This study also provides a good comparison between the different techniques used.

- The *fifth chapter* describes the functionalisation of gold nanoparticles in aqueous media using curcumin, the wonder drug obtained from turmeric, acting both as reducing and stabilizing agent. The study begins with the spectroscopic evidences of solubilising curcumin in water in a temperature-dependent manner. An attempt to explain the mechanism involved is elaborated. The as-synthesized gold nanoparticles are characterized using different techniques and these nanoparticles are shown to possess good anti-oxidant activity.

1.4. References

1. Landman, U., and Luedtke, W.D. (2004) *Faraday Discuss* 125, 1; discussion 99.

2. Feynman, R. (1960) Plenty of room at the bottom. In *Engineering and Science*, California Institute of Technology

3. Ralph S. Greco, *et al.* (2005) *Nanoscale technology in biological systems*. CRC Press, 2005

4. Roduner, E. (2006) *Chem Soc Rev* 35, 583

5. Henglein, A. (1988) *Topics in Current Chemistry* 143, 113

6. El-Sayed, M.A. (2001) *Accounts of Chemical Research* 34, 257

7. Greenberg, A. (2009) *ACS Nano* 3, 762

8. Gary, H. (2007) When Small Is Different: Some Recent Advances in Concepts and Applications of Nanoscale Phenomena. 19, 639

9. Yin, Y., and Alivisatos, A.P. (2005) *Nature* 437, 664-670

10. Hendrich, C., *et al.* (2003) *Applied Physics B-Lasers and Optics* 76, 869

11. Ziegler, T., *et al.* (2004) *Chemical Physics Letters* 386, 319

12. Dulkeith, E., *et al.* (2004) *Physical Review B* 70, 205424

13. Pinchuk, A., and Kreibig, U. (2003) *New Journal of Physics* 5, 151

14. Mulvaney, P. (1996) *Langmuir* 12, 788

15. Sardar, R., *et al.* (2009) *Langmuir* 25, 13840

16. Leonhardt, U. (2007) *Nature Photonics* 1, 207

17. Buffat, P., and Borel, J.P. (1976) *Physical Review A* 13, 2287

18. Thomson, W. (1871) *Philos. Mag.* 42, 448

19. Haruta, M. (1997) *Catalysis Today* 36, 153

20. Narayanan, R., and El-Sayed, M.A. (2005) *Journal of Physical Chemistry B* 109, 12663

21. Zecchina, A., *et al.* (2007) *Chemistry-a European Journal* 13, 2440

22. Mooradian, A. (1969) Photoluminescence of Metals. *Physical Review Letters* 22, 185

23. Nakae, Y., *et al.* (2000) *Physica B-Condensed Matter* 284, 1758

24. Yamamoto, Y., *et al.* (2003) *Physica B-Condensed Matter* 329, 1183

25. Ito, T., and Okazaki, S. (2000) *Nature* 406, 1027

26. Xia, Y., *et al.* (1999) *Chem Rev* 99, 1823

27. Barth, J.V., *et al.* (2005) *Nature* 437, 671

28. Turkevich, J., *et al.* (1951) *Discuss. Faraday Soc.* 11, 55-75

29. Frens, G. (1973) *Nature-Physical Science* 241, 20

30. Sun, Y., and Xia, Y. (2002) *Science* 298, 2176

31. Cushing, B.L., *et al.* (2004) *Chemical Reviews* 104, 3893

32. Pileni, M.P. (2003) *Nature Materials* 2, 145

33. Peng, X., *et al.* (1998) *Journal of the American Chemical Society* 120, 5343

34. Brust, M., *et al.* (1994) *Journal of the Chemical Society-Chemical Communications*, 801

35. Brust, M., *et al.* (1995) *Journal of the Chemical Society-Chemical Communications*, 1655

36. Hostetler, M.J., *et al.* (1996) *Journal of the American Chemical Society* 118, 4212

37. Templeton, A.C., *et al.* (1999) *Journal of the American Chemical Society* 121, 7081

38. Milliron, D.J., *et al.* (2004) *Nature* 430, 190

39. Kitaura, R., *et al.* (2008) *Nano Lett* 8, 693

40. Kitaura, R., *et al.* (2009) *Angew Chem Int Ed Engl* 48, 8298

41. Khodakovskaya, M., *et al.* (2009) *ACS Nano* 3, 3221

42. Eichenfield, M., *et al.* (2009) *Nature* 462, 78

43. Eichenfield, M., *et al.* (2009) *Nature* 459, 550

44. Tessler, N., *et al.* (2002) *Science* 295, 1506

45. Kazes, M., *et al.* (2002) *Advanced Materials* 14, 317

46. Huynh, W.U., *et al.* (2002) *Science* 295, 2425

47. Park, M.-H., *et al.* (2009) *Nano Letters* 9, 3844

48. Kahan, D.M. (2009) *Nat Nanotechnol* 4, 705

49. Satterfield, T., *et al.* (2009) *Nat Nanotechnol* 4, 752

50. Hoet, P.H.M., *et al.* (2004) *Nature Biotechnology* 22, 19

51. Donaldson, K., and Poland, C.A. (2009) *Nat Nanotechnol* 4, 708

52. Oberdorster, G., *et al.* (2002) *J Toxicol Environ Health A* 65, 1531

53. Nemmar, A., *et al.* (2002) *Circulation* 105, 411

54. Lam, C.W., *et al.* (2004) *Toxicol Sci* 77, 126

55. Bermudez, E., *et al.* (2004) *Toxicol Sci* 77, 347

56. Ding, L., *et al.* (2005) *Nano Lett* 5, 2448

57. Lewis, L.N. (2002) *Chemical Reviews* 93, 2693

58. Mandal, S., *et al.* (2005) *Current Applied Physics* 5, 118

59. Xia, Y., *et al.* (2009) *Angewandte Chemie-International Edition* 48, 60

60. Ulman, A. (1991) *An Introduction to Ultathin Organic Films: From Langmuir-Blodgett to Self-Assembly*. Academic Press

61. Vaseashta, A., *et al.* (2004) *Nanostructured and Advanced Materials*. Springer

62. Rotello, V. (2004) *Nanoparticles Building Blocks for Nanotechnology*. Plenum Publisher

63. Katari, J.E.B., *et al.* (1994) *Journal of Physical Chemistry* 98, 4109

64. Xia, Y.N., *et al.* (1999) *Chemical Reviews* 99, 1823

65. Kleinfeld, D., *et al.* (1988) *Journal of Neuroscience* 8, 4098

66. Niemeyer, C.M., and Mirkin, C.A. (2004) *Nanobiotechnology*. WILEY-VCH

67. El-Sayed, I.H., *et al.* (2005) *Nano Letters* 5, 829

68. Kristina, R., *et al.* (2009) *Angewandte Chemie International Edition* 48, 872

69. Gurwitz, D., and Livshits, G. (2006) *Eur J Hum Genet* 14, 376

70. Robertson, R. (2000) Encapsulated low-energy brachytherapy sources

EXPERIMENTAL PROCEDURES

Chapter 2

This chapter comprises of an overview of all the techniques used in this thesis work, their principle, instrument and working specifications and their uses.

2.1 Spectroscopy

Spectroscopy is the study of interaction of light (or say electromagnetic radiation, to be more scientific!) and matter. It is one study that has revolutionized for centuries throughout the history of science. The classic experiments of Sir Isaac Newton (1642-1720) constitutes the first scientific study of spectroscopy, when in 1666 he produced the spectrum of colors from white light using a triangular glass prism.
The distribution of energy possessed by a molecule at any given moment, defined as the sum of the contributing energy terms:

$$E_{\text{total}} = E_{\text{electronic}} + E_{\text{vibrational}} + E_{\text{rotational}} + E_{\text{translational}}$$

The electronic component is linked to the energy transitions of electrons as they are distributed throughout the molecule, either localized within specific bonds, or delocalized over structures, such as an aromatic ring. The vibrational energy corresponds to the absorption of energy by a molecule as the component atoms vibrate about the mean center of their chemical bonds. Rotational energy, which gives rise to its own form of spectroscopy, is observed as the tumbling motion of a molecule, which is the result of the absorption of energy within the microwave region. The translational energy relates to the displacement of molecules in space as a function of the normal thermal motions of matter. Interaction at the different energy levels is used for studying the sample, using different spectroscopy as explained in the following sections.

2.1.1 Ultra-violet and Visible Spectroscopy

Also known as *Electronic Spectroscopy* since the absorption of ultraviolet and/or visible light by a molecule leads to electronic transitions in the molecule. The strength of electronic spectroscopy lies in its ability to measure the extent of multiple bond or aromatic conjugation within molecules[1]. This spectroscopy is primarily used in studying organic molecules, and helps in differentiating conjugated dienes from non-conjugated dienes, conjugated dienes from conjugated trienes, αβ-unsaturated

ketones from their βγ-analogs, etc. Electronic spectroscopy may also be used to study changes or strains in the molecules and formation of dimers or polymers by correlating the change in the spectrum. These distinctions are easily achieved largely on the basis that the longer the conjugation, the longer the wavelength of the absorption maxima in the spectrum[1].

Chormophores (Greek chromophoros – color carrier) are any functional groups that absorb electromagnetic radiation, whether or not a 'color' is produced. The absorption spectrum is formed of absorption bands, rather than absorption lines, because vibrational and rotational effects are superimposed on the electronic transitions so that an envelope of transitions arises. Energy absorbed in the UV or visible region causes changes in the electronic energy of the molecule, and hence results in corresponding change in its ability to absorb light in the UV–visible region of electromagnetic radiation, in turn leading to color transitions. The relationship between the energy absorbed in an electronic transition and the frequency (ν), wavelength (λ) and wavenumber ($\bar{\upsilon}$) of radiation producing the transition can be explained as:

$$\Delta E = h\nu = hc \div \lambda = h\bar{\upsilon}c$$

where *h* is the Planck's constant,

c is the velocity of light and

ΔE is the energy absorbed in an electronic transition in a molecule from a low energy state (ground state) to a higher energy state (excited state).

Absorption of light by molecules is governed by the Beer-Lambert's law:

$$\log\left({}^{Io}/_{I}\right) = \varepsilon cl \qquad \text{or} \qquad \varepsilon = A/cl$$

where *Io* is the intensity of the incident light (or the light intensity passing through a reference cell),

I is the light transmitted through the sample solution,

Log (*Io*/*I*) is the absorbance (A) of the solution (formerly called the optical density, O.D.),

c is the concentration of solute (in mol l^{-1}, mol dm^{-3}),

l is the path length of the sample (in cm, m x 10^{-2}) and

ε is the molar absorptivity (formerly called the molecular extinction coefficient, in l mol^{-1} cm^{-1}, m^2 mol^{-1} x 10^{-2}). This value is constant for a particular molecule/compound at a given wavelength.

The spectrum collected for each sample throughout the work is above the lower wavelength limit for each solvent in which the sample is dispersed or dissolved. (The 'lower wavelength limit' is the limit below which the solvent will show excessive absorbance and hence the sample absorbance will not be recorded linearly) Thus, the lower wavelength limit for common solvents such as water, ethanol (95% or absolute), methanol, dichloromethane and carbon tetrachloride is 205 nm, 210 nm, 210 nm, 235 nm and 265 nm respectively. Generally, the conventional Ultra-violet and visible spectroscopic technique is not used below 200 nm, since oxygen present in air absorbs strongly in this wavelength.

The position and intensity of a maximum absorbance band of a molecule may shift when the spectrum is recorded in different solvents. This is called the 'solvent effect', and is discussed at length in Chapter 5.

In addition to the study of the electronic transitions involved in molecules upon interaction with the incident light, the Ultra-Violet and visible spectroscopy is a powerful tool to study and characterize noble metal colloidal particles, since they absorb strongly in the visible region. It is used as a major technique to study the surface plasmon resonance (SPR) of gold nanoparticles in this work. The phenomenon of SPR is explained in Chapter 4 in detail.

For all temperature-dependent and *in situ* UV-vis spectroscopy studies, we used a Cary 50 UV-vis spectrophotometer. For the rest, we used a Jasco UV-vis-NIR spectrometer (model V570 UV/vis/NIR) dual-beam spectrometer. Matched quartz cells (cuvettes) are used for the experiments after they are thoroughly cleaned and wiped with soft tissue, without hampering the optical surfaces.

2.1.2 Fourier Transform Infra-Red (FTIR) Spectroscopy

In FTIR spectroscopy, a mathematical operation known as Fourier transformation converts the *time domain* signal (intensity versus time) to the *frequency domain* signal (intensity versus frequency). This relationship was studied and defined by Jean-Baptiste Joseph Fourier (1768-1830). This assists in saving the time required to obtain an IR spectrum (1 sec or less versus 10 to 15 min for a single scan). This in turn, provides an opportunity to enhance the signal-to-noise (S/N) ratio of IR spectrum by increasing the total number of sample scans, since the S/N ratio is proportional to the square root of the total number of scans. This explains the term

"Fourier transform" used in infrared spectrometry. In FTIR spectroscopy, frequency is conventionally displayed in the form of wavenumber ($\bar{\upsilon} = 1/\lambda$).

Infra-Red Spectroscopy deals with the fact that the atoms in a molecule vibrate about some mean position; thus it is also called the *vibrational spectroscopy*. The vibrational spectrum of a molecule is considered to be a unique physical property and is characteristic of the molecule. The basic interpretation of an FTIR spectrum leads to the characterization and identification of the sample. The IR spectrum is formed as a consequence of the absorption of electromagnetic radiation at frequencies that correlate to the vibration of specific sets of chemical bonds from within a molecule. Bonds with different bond lengths, strength, bending and torsional characteristics absorb different wavelengths of IR radiation, and the absorption maxima maybe characteristics of the types of linkages present; the absorption generally occurs in the 4000 – 400 cm^{-1} region of the spectrum. The fundamental requirement for infra-red activity, leading to absorption of infrared radiation, is that there must be a net change in dipole moment during the vibration[2]. A few examples to name are: the O-H and N-H vibrations are detected in the 3000-3700 cm^{-1}, the sulfate ion is in the 1100 cm^{-1} and 500 cm^{-1} and the ammonium ion vibrates in the 3100 cm^{-1} and 1400 cm^{-1} region of the radiation.

FTIR data presented in this thesis were taken from Perkin-Elmer FTIR Spectrum 1 spectrophotometer operated at a resolution of 4 cm^{-1}. Diffuse Reflectance Infrared Fourier Transform (DRIFT) was the method used for recording the IR spectra of all samples. Samples were either finely powdered with KBr and formed pellets or were drop-coated onto clean silicon wafers and dried prior to measurements.

2.1.3 Fluorescence Spectroscopy

The first observation of fluorescence from a quinine solution in sunlight was reported by Sir John Frederick William Herschel in 1845.[3] Fluorescence is now a dominant methodology used extensively in biotechnology, flow cytometry, medical diagnostics, DNA sequencing, forensics, and genetic analysis, to name a few. Fluorescence detection is highly sensitive. Many fluorophores display sub-nanosecond lifetimes. In contrast to aromatic organic molecules, atoms are generally non-fluorescent in condensed phases. One notable exception is the group of elements commonly known as the lanthanides[4]. A fluorescence emission spectrum is a plot of the fluorescence intensity

versus wavelength (nm) or wavenumber (cm^{-1}). Emission spectra vary widely and are dependent upon the chemical structure of the fluorophore and the solvent in which it is dissolved. A number of possible interactions such as quenching, energy transfers and solvent interactions occur in the process of fluorescence. Professor Alexander Jablonski is regarded as the father of fluorescence spectroscopy because of his many accomplishments, including descriptions of concentration depolarization and defining the term "anisotropy" to describe the polarized emission from solutions[5]. A typical Jablonski diagram, used to illustrate various molecular processes that can occur in excited states is shown in Figure 2.1.

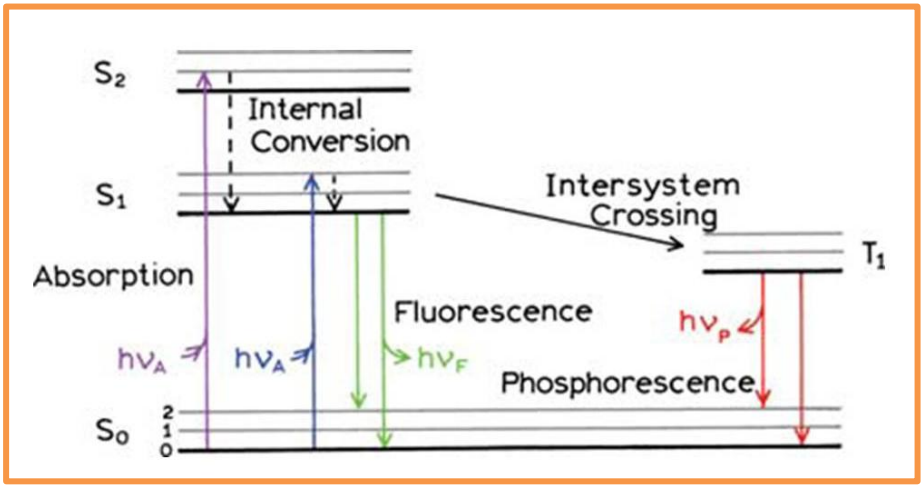

Figure 2.1. Representative Jablonski diagram [5])

The singlet ground, first, and second electronic states are respectively depicted by S0, S1, and S2; energy states containing only spin-paired electrons are called singlet-states, while those with parallel spin electrons are called triplet states (T1, etc.). At each of these electronic energy levels the fluorophores can exist in a number of vibrational energy levels, depicted by 0, 1, 2, etc. The transitions between states are depicted as vertical lines to illustrate the instantaneous nature of light absorption. Transitions occur in about 10^{-15} s, a time too short for significant displacement of nuclei. This is the Franck-Condon principle. A fluorophore is usually excited to some higher vibrational level of either S1 or S2. With a few rare exceptions, molecules in condensed phases rapidly relax to the lowest vibrational level of S1. This process is called internal conversion and generally occurs within 10^{-12} s or less.

Since fluorescence lifetimes are typically near 10^{-8} s, internal conversion is generally complete prior to emission.

Molecules in the S1 state can also undergo a spin conversion to the first triplet state T1. Emission from T1 is termed phosphorescence, and is generally shifted to longer wavelengths (lower energy) relative to the fluorescence. Conversion of S1 to T1 state, which is more stable than S1 and more long-lived, is called intersystem crossing. Transition from T1 to the singlet ground state is forbidden, and as a result the rate constants for triplet emission are several orders of magnitude smaller than those for fluorescence.

In 1852, Sir G. G. Stokes, at the University of Cambridge observed for the first time that fluorescence typically occurs at lower energies or longer wavelengths[6]. The Stokes shift could be explained by the rapid decay to the lowest vibrational level of S1, followed by the general decay to the highest vibrational levels of S0. Thus, resulting in the loss of the excitation energy in the form of thermalisation required for the excess vibrational energy; and hence the shift in the emission peak to longer wavelengths. The Stokes shift is also contributed by solvent effects, excited-state reactions, complex formation, and/or energy transfer.

2.1.4 X-ray Photoemission Spectroscopy (XPS) or Electron Spectroscopy for Chemical Analysis (ESCA)

When an organic molecule is bombarded with MgKα or AlKα radiations, in a vacuum chamber, electrons are ejected from the carbon 1s orbitals and the spectrum of energies in these ejected electrons can be recorded as a direct measure of the core binding energies for C 1s orbitals. (Figure 2.2) Thus the fundamental on which the ESCA or XPS is based on is that the *different elements have different binding energies* (B.E.) and each element in a molecule can be detected from the ESCA spectrum; also, atoms of the same element which are in different environments within a molecule, have different core B.E. giving rise to *chemical shifts* in the ESCA spectrum. It is a highly sensitive technique and as explained, it is based on the principle of the photo-electric effect. The kinetic energy (K.E.) distribution of the emitted photoelectrons is measured and a photoelectron spectrum is obtained.

$$\text{K.E.} = h\nu - \text{B.E.}$$

The B.E. of electrons in various energy levels in the solids are conventionally measured with respect to the Fermi level, rather than the vacuum level. This involves a small correction to the above equation in order to account for the work function (Φ) of the solid:

$$\text{K.E.} = h\nu - \text{B.E.} - \Phi$$

Electrons traveling through a material have a relatively high probability of experiencing inelastic collisions with locally bound electrons as a result of which they suffer energy loss and contribute to the background of the spectrum rather than a specific peak. However, XPS signals are recorded in the form of peaks only from those photo-emitted electrons, which successfully reach the surface without undergoing inelastic collisions. Since the fraction of such electrons decrease significantly with distance, XPS cannot provide information beneath a certain distance (< 100 Å) and hence XPS is known to be a surface-sensitive technique.

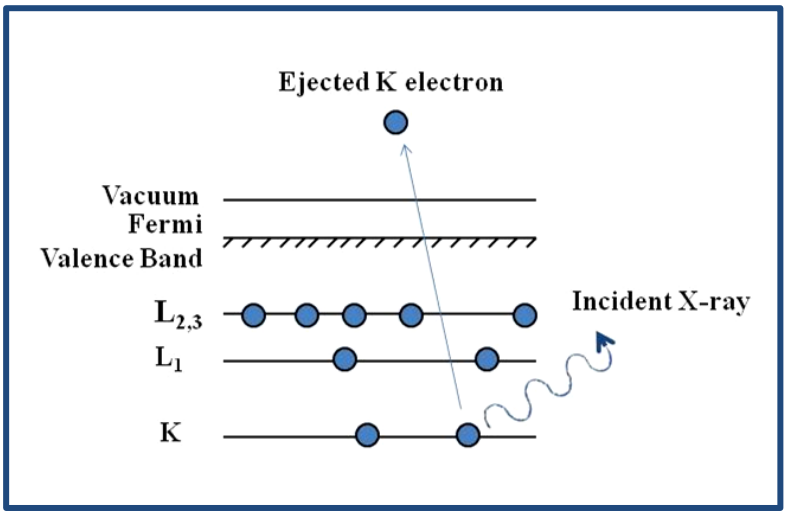

Figure 2.2. Schematic diagram of the XPS process showing photo ionization of an atom by the ejection of a 1s electron.

For the work described in this thesis, the XPS spectra of various core levels were recorded and their binding energies were aligned with respect to C 1s B.E. of 285 eV. Samples for XPS in this study were prepared by drop-coating on the Si substrates. A VG MicroTech ESCA 3000 instrument at a pressure of < 1 x 10^{-9} torr with an overall resolution of 1 eV was used. The spectra were recorded with

unmono-chromatic Mg Kα radiation (photon energy = 1253.6 eV) at a pass energy of 50 eV and an electron take-off angle (angle between the electron emission direction and the surface plane) of 60°.

2.1.5 Nuclear Magnetic Resonance (NMR) Spectroscopy

Felix Bloch and Edward M. Purcell shared the Noble prize in Physics in 1946 for their independent studies on proton NMR. NMR spectroscopy is study of differences in the magnetic properties of the various magnetic nuclei present in a molecule and to deduce in large measure what the positions of these nuclei are within the molecule. The different kinds of environment and the different kinds of atoms present in a molecule could be deduced. Also the number of atoms present can be known.

The nucleus of the hydrogen atom (the proton) possesses both an electric charge and a mechanical spin; thus, it generates a magnetic field. Upon the effect of an external magnetic field, the proton aligns either with the field (lower energy state) or opposed to the field (higher energy state), in accordance with the quantum restrictions. The spinning proton acting like a spinning magnet precesses around the axis of the applied external magnetic field. The spinning frequency of the nucleus does not change but the speed of the precession does.

The *precessional frequency, ν,* is directly proportional to the strength of the external magnetic field (B_o).

$$\nu \alpha B_o$$

The exact frequency is given by

$$\nu = (\gamma Bo) \div (2\pi)$$

where, γ is the magnetic-gyric ratio, being the ratio between the nuclear magnetic moment, μ, and the nuclear angular momentum, **I**; γ is also called the gyro magnetic ratio.

If the precessing nuclei are irradiated with a beam of radiofrequency, the low-energy nuclei may absorb this energy and move to a higher state. The precessing proton will only absorb energy from the radiofrequency source if the precessing frequency is the same as the frequency of the radiofrequency beam; the nucleus and the radiofrequency are then in resonance, hence the term *nuclear magnetic resonance*[1].

The only nucleus that exhibit the NMR phenomenon are those for which the spin quantum number I is greater than 0. The precessional frequency of all protons in the same external applied field is not same and the precise value for any one proton depends on a number of factors. Because these shifts in the frequency depend on the chemical environment, it is called the chemical shift. The factors influencing the chemical shifts in a NMR spectrum are: electro negativity (shielding and deshielding), van der Waals deshielding and anisotropic effects.

In this thesis work, the entire ^{1}H NMR spectra were taken using a 400 MHz Bruker AVANCE instrument using a broad band probe with a z-gradient coil. Chemical shifts (δ) are quoted in ppm and are referenced to respective solvents as the case maybe.

2.2 X-Ray Diffraction (XRD)

Wilhelm Conrad Röntgen discovered the X-rays in 1895. XRD is a fingerprint characterization of crystalline materials and determination of their structure based on the diffraction pattern produced by the set of atoms in the crystal when X-rays of known wavelength are incident upon them. Crystalline materials are characterized by the orderly periodic arrangements of atoms. The atoms in a crystal are a periodic array of coherent scatterers and thus can diffract light. (Figure 2.3)

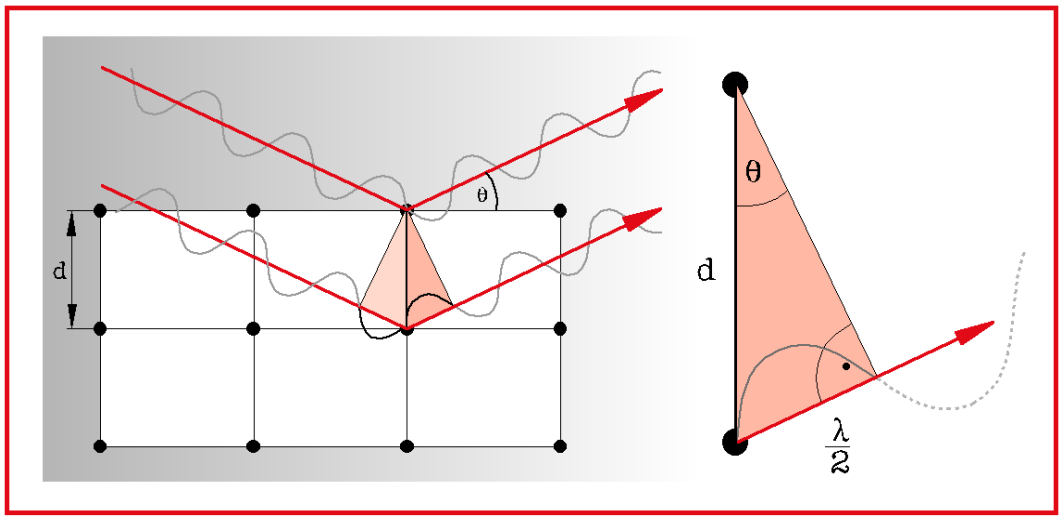

Figure 2.3. Schematic showing diffraction of X-ray from scattering centers (atoms) in the crystal.

The sample is usually in a powder form, consisting of randomly oriented fine grains of crystalline material. When the diffraction pattern is recorded, it shows concentric rings of scattering peaks corresponding to various inter-planar spacing in the crystal lattice. The positions and the intensities of peaks are used to identify the underlying crystal structure of the material.

W.H. Bragg (father) and William Lawrence Bragg (son) developed a simple relation for scattering angles, now call Bragg's law:

$$d = \frac{n\lambda}{2 \sin \theta}$$

where d is the spacing between the planes,

λ is the wavelength of the X-rays and

θ is the angle (See figure).

Constructive interference only occurs for certain θ's correlating to a (*hkl*) plane, specifically when the path difference is equal to *n* wavelengths.

Scherrer's Formula is used to calculate the thickeness or the size of the crystallite:

$$t = \frac{K \times \lambda}{B \times \cos \theta}$$

t = thickness of crystallite

K = constant dependent on crystallite shape (0.89)

λ = x-ray wavelength

B = FWHM (full width at half max) or integral breadth

θ = Bragg angle

In this thesis work, to confirm the crystal structure of nanoparticles, the samples were dropped coated onto a glass slide and were analyzed for the XRD pattern on a Philips X'pert. Iron-filtered Cu Kα radiation (λ=1.5406 Å) was used. The sample was scanned at the rate of 2θ = 2° per min. The data acquired was compared with the database (PCPDF).

2.3 Transmission Electron Microscopy (TEM)

The TEM was the first type of electron microscope to be developed and is patterned exactly on the light transmission microscope except that a focused beam of electrons is used instead of light to "see through" the specimen. It was deveopled by Max Knoll and Ernst Ruska in Germany in 1931. [See Table 2.1]

Table 2.1. Origin of the Electron Microscope (EM)

Date	Name	Events
1897	J. J. Thompson	Discovers the electron
1924	Louis de Broglie	Defines the wave nature of electrons
1926	H. Busch	Magnetic or electric field acts as lenses for electrons
1929	E. Ruska	Doctoral thesis on magnetic lenses
1931	Knoll & Ruska	First electron microscope built
1931	Davisson & Calbrick	Properties of electrostatic lenses
1934	Driest & Muller	Surpass resolution of light microscope
1938	Von Borries & Ruska	First practical EM 10 nm resolution
1940	RCA	Commercial EM with 2.4 nm resolution

The classical Rayleigh criterion for light microscopy states that the smallest distance that can be resolved, δ, is given approximately by

$$\delta = \frac{(0.61\ \lambda)}{(\mu \sin \beta)}$$

where λ is wavelength of the radiation,

μ is the refractive index of the medium, and

β is the semi-angle of collection of the magnifying lens.

So, the resolution of green light (550 nm) in a good light microscope is about 300 nm. This is the limit of the light microscopy. For a 100 keV electron, the wavelength is about 4 pm (0.004 nm), much smaller than the diameter of an atom, and thus using electrons as the probe in a microscopy increased the resolution to as small as 0.2 nm (2 Å).

Being small and charged particles they interact considerably with atoms and molecules which will produce the specimen information like contrast in TEM image, chemical composition by X-ray crystallography, diffraction pattern etc.

Usually the electrons that undergo elastic scattering contribute to imaging in TEM; however, the electrons that undergo inelastic scattering but do not significantly lose their energy can also participate in the imaging of an object. As a result, based on the interaction of falling electrons with different elements in the object, differences in

light intensity (contrast) are created in the final image, which relates to areas in the object with different scattering potentials. This fact can be deduced from the Rutherford formula, which describes the deflection potential of an atom:

$$K = \frac{-e.eZ}{r^2}$$

where *K* is the deflection potential,

e is the electron charge,

z is the positive charge and

r is the distance between electron to nucleus.

As the atomic number of interacting element increases, their scattering efficiency also increases. In TEM, the great depth of focus provides the high magnification of the sample. Thus, in addition to the size, shape and arrangement of particles, crystallographic information (the arrangement of atoms, degree of order, detection of atomic defects in composition of sample) and compositional information can be obtained.

Samples for TEM imaging were dropped coated onto carbon-coated copper TEM grids. TEM measurements were performed on a JEOL model 1200EX instrument operated at an accelerating voltage of 120 kV for images in Chapter 3. TEM micrographs shown in Chapter 4 & 5 are obtained on a Tecnai F30 HRTEM from FEI Inc., equipped with field emission source operating at 300 kV.

The ability to determine crystallographic orientations locally (down to the nm level) gives TEM its great advantage over SEM and visible-light microscopes.

SAD (Selected Area Diffraction)

Electron Diffraction is an indispensable part of TEM. The Diffraction Pattern (DP) from the SAD of a specimen provides information on the crystalline or amorphous nature of the specimen, if it is crystalline, then the crystallographic characteristics (lattice parameters, symmetry, etc.) of the specimen, the grain morphology, grain-size distribution, orientation of the specimen or of individual grains with respect to the electron beam, and if there are more than one phase present in the specimen. The use of electron diffraction for materials studies began around 1930s. Here, electrons are diffracting from a set of planes of spacing *d* such that we have both constructive and destructive interference. The SAD patterns are sharply focused spot patterns.

The differences in using electrons from X-rays are:

- Electrons have a much shorter wavelength
- Electrons are scattered more strongly because they interact with both the nucleus and the electrons of the scattering atoms through Coulomb forces
- Electrons beams are easily directed because electrons are charged particles[7]

2.4 Scanning Electron Microscopy (SEM)

Charles Jatley is the pioneer of scanning electron microscope (1965). SEM is able to provide 3–dimensional images of the objects, since it does not record the electrons passing thorough the specimen (as in TEM); on the other hand, it records the secondary electrons that are released from the sample as a result of interaction with falling electron beam. The broad magnification range of the SEM, coupled with the ease of shifting magnification makes its operation easy, in order to zoom a gross image to a final image showing finer details. The surface of the material is sputter coated with a thin-layer of gold or another conductive material and is scanned by a thin beam of electrons. When the electron beam strikes the sample, some of the electrons interact with the nucleus of the atom. The negatively charged electrons are attracted towards the positively charged nucleus, however if the angle is just right, instead of being captured by the nucleus, these electrons (backscattered electrons) encircle the nucleus and come back out of the sample without slowing down and form an image. In addition, beam electrons also interact with the specimen electrons, which slow down the beam electrons. Beam electrons, in turn push the specimen electrons out of the sample surface and these specimen electrons are called secondary electrons. Unlike the backscattered electrons, the secondary electrons move very slowly while they leave the sample. A positively charged detector pulls in the slow moving secondary electrons from a wide area and from around the sample corners. The ability to pull in secondary electrons from around the corners gives secondary electron image a 3–D look. The detector also counts the secondary electrons ejected from sample and hence image contrast is created based on the intensity of electrons emitted from each spot on the sample[8].

SEM images presented in the thesis were carried out on a Leica Stereoscan – 440 instrument. Samples were prepared either by drop coating samples on Si (100) wafers.

2.5 Atomic Force Microscopy (AFM)

Antonie Philips van Leeuwenhoek is deservedly called the Father of Microscopy; he ground and prepared his own lens through which he observed and reported the live, microscopic single celled organisms that he called animalcules. However, the AFM is no where related to the conventional light microscope, where lens are primarily used to focus and procure an image. Nonetheless a microscope it is.

Atomic Force Microscopy is a development of STM (Scanning Tunneling Microscopy) that was awarded the Nobel Prize in the year 1986 to Gerd Binnig and Heinrich Rohrer[9, 10]. The STM itself is very similar to an instrument called the Topografiner, invented by Young, only that the STM has very high resolution. Binnig, Quate and Gerber replaced the electron tunnelling from a fine wire of the STM with the cantilever approach and invented the AFM, in 1986[11].

Scanning Probe Microscopes (SPMs) are based on the concept of "near-field microscopy," which overcomes the problem of the limited diffraction-related resolution inherent in conventional microscopes because the probe, located in the immediate vicinity of the sample itself (usually within a few nanometers), records the intensity and not the interference signal, and this greatly improves the final resolution. SPMs represent a new family of microscopes that are specifically dedicated to the investigation of surface morphology and provide details of unprecedented resolution without the need for complicated sample preparation. The AFM consists of a microscale cantilever with a sharp tip/probe (radius of curvature of the order of nanometers) at its end that is used to scan the specimen surface. When the tip is brought into proximity of a sample surface, forces between the tip and the sample lead to a deflection of the cantilever according to Hooke's law. Depending on the situation, forces that are measured in AFM include mechanical contact force, van der Waals forces, capillary forces, chemical bonding, electrostatic forces, magnetic forces, solvation forces etc. AFM is a recently developed technique that has extended the use of SPMs to the observation of nonconductive surfaces and that has thus opened up unexpected possibilities for the surface analysis of various specimens.

Some of the techniques available are:

Contact AFM—Measures topography by sliding the probe's tip across the sample surface.

Tapping Mode AFM— Measures topography by tapping the surface with an oscillating tip. This eliminates shear forces which can damage soft samples and reduce image resolution.

Phase Imaging—Provides image contrast caused by differences in surface adhesion and visco-elasticity.

Non-contact AFM—Measures topography by sensing van der Waals attractive forces between the surface and the probe tip held above the surface.

Magnetic Force Microscope (MFM)—Measures magnetic force gradient distribution above the sample surface. It is performed using Lift Mode to track topography.

Electric Force Microscope (EFM) — Measures electric field gradient distribution above sample surfaces. It is performed using Lift Mode to track topography.

Force Modulation—Measures relative elasticity/stiffness of surface features. Force modulation is only one of several types of force imaging which are possible.

Electrochemical Microscopy (ECSTM and ECAFM)—Measures the surface structure and properties of conducting materials immersed in electrolyte solutions with or without potential control.

Lithography—Use of a probe tip to mechanically scribe or indent a sample surface. It may be used to generate patterns, test surfaces for micro-hardness, etc.

The atomic force microscopy measurements were performed using a Multimode scanning probe microscope equipped with a Nanoscope IV controller from Veeco Instrument Inc., Santa Barbara, CA. Both contact mode and tapping modes were used in the study for obtaining good images.

2.6 Dynamic Light Scattering (DLS) study

The dynamics of non-interacting colloidal particles can be characterized as a stochastic process, the so-called Brownian motion[12]. Dynamic Light Scattering (DLS) measures the temporal autocorrelation of scattered light arising from the Brownian motion of the dispersed particles. DLS (sometimes referred to as **P**hoton **C**orrelation **S**pectroscopy or **Q**uasi-Elastic **L**ight **S**cattering) is a technique for measuring the size of particles typically in the sub micron region. The larger the particle, the slower the Brownian motion will be. Smaller particles are "kicked" further by the solvent molecules and move more rapidly. The speed at which the

particles are diffusing due to Brownian motion is measured by the rate at which the intensity of the scattered light fluctuates when detected. The rate at which the intensity fluctuations occur will depend on the size of the particles (See Figure 2.4).

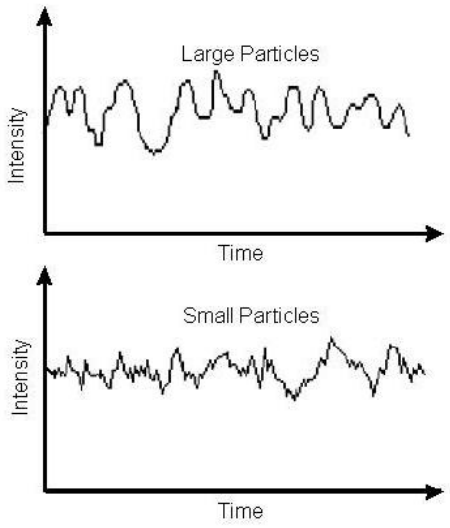

Figure 2.4. Schematic graph showing typical intensity fluctuations for large and small particles.

The small particles cause the intensity to fluctuate more rapidly than the large ones. The intensity fluctuations arising from the Brownian motion of particles are compared with itself at a particular point of time and a time much later, then for a randomly fluctuating signal it is obvious that the intensities are not going to be related in any way, i.e. there will be no correlation between the two signals. (Figure 2.5) This is done using a digital auto correlator, which basically a signal comparator. The correlator compares the scattering intensity at successive time intervals to derive the rate at which the intensity is varying. Size is obtained from the correlation function by using various algorithms.

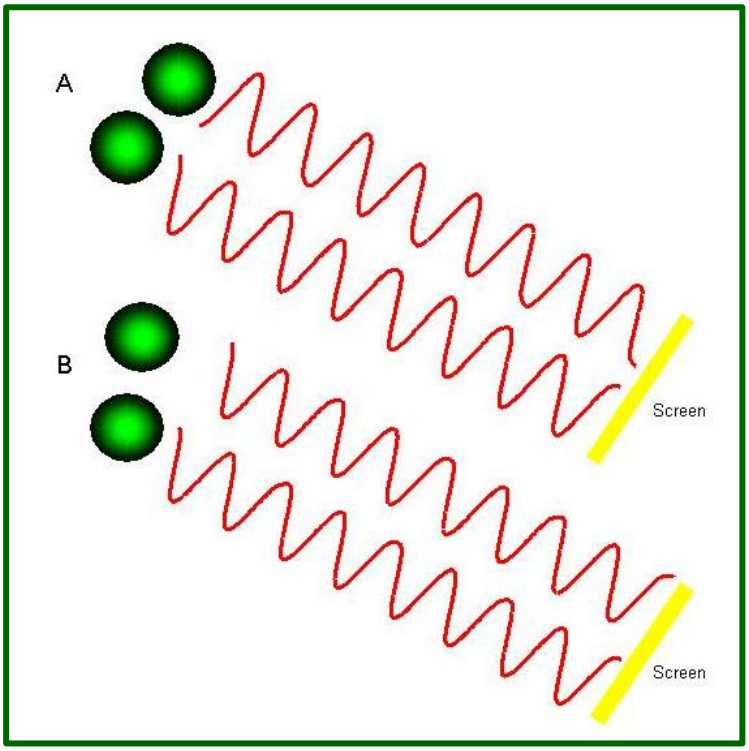

Figure 2.5. Schematic showing two beams that interfere destructively (**A**) and constructively (**B**) as the particles fluctuate.

For a large number of mono-disperse particles in Brownian motion, the correlation function is an exponential decaying function of the correlator time delay. For further explanation, please refer experimental details in Chapter 4.

DLS measurements were performed using a Zetasizer Nano S (Malvern Instruments Ltd., UK) with a 3 mW He-Ne laser operating at λ) 633 nm. The unit collects light back-scattered at an angle of 173°. All samples were filtered in a laminar flow prior to collecting the data.

2.7 HPLC

Chromatography involves the column resolution of a pulse (or small batch) of flowing, multi-component fluid into separate fluid volumes of (nearly) pure solute solutions. Biological molecules such as proteins, antibiotics, etc. have varying tendencies to adsorb onto such materials as starch, diatomaceous earth, and polyacrylamide gel. As a result, when a solution containing proteins, for example, is passed over such a phase, each protein moves at an effective velocity which decreases as the protein's propensity to adsorb increases. There are also different

types of chromatography, based on the column and method used, such as molecular-sieve (or gel-filtration or gel-permeation) chromatography, ion-exchange chromatography and affinity chromatography.

For example, in analyzing mixtures of sugars such as maltose and glucose, the different affinities of these sugars for the primary amino groups on the surface of the support material in a commercially prepared carbohydrate column is used to separate the sugars in an HPLC (High Performance Liquid Chromatography) apparatus. The different sugars emerge from the column at different times, and they are then detected and quantified separately using a refractive index detector[13]. Separations based on HPLC are useful in resolving mixtures of related components before their individual quantification. The HPLC chromatogram and its analysis used in the work are stated in Chapter 5. The data was collected on the HPLC system- Delta 600 series from Waters Corporation and 425 nm wavelength was used for detection. The elution was carried out with gradient solvent systems with a flow rate of 1.0 mL/min at ambient temperature. The compounds were analyzed using HP ChemStation software.

2.8 Thermo gravimetric analysis (TGA)

In the thermo gravimetric analysis (TGA), the sample is subjected to a controlled temperature program and based on the temperature difference between the sample and a standardized reference cell, the physical property is measured and calculated. The determination of changes in chemical or physical properties of material and information about its phase transformation as a function of temperature can be obtained by TGA. TGA is based on the measurement of weight loss of the material as a function of temperature. TGA curve provides information concerning the thermal stability of the initial sample, intermediate compounds that might form and of the residues, if any. In addition to thermal stability, the weight losses observed in TGA can be quantified to predict the pathway of degradation or to obtain compositional information. The experimental data offers more sophisticated understanding of reactions occurring at materials heating. In this thesis, TGA was performed to find out the contribution of biomolecules in the metal nanostructures, using TA instruments, SDT Q 600 thermal analysis system operated under nitrogen flow in the temperature range of 50-800 °C with a heating rate of 20 °C/min. The

dialysed nanoparticles sample in solution was first lyophilized to remove the water and properly dried to remove any moisture content. The fine powder was then weighed and heated under inert atmosphere (nitrogen gas). The loss is measured until there is no change (upto 900 °C). Untreated biomolecules is used as a control in each case.

2.9 Electrophoresis

Electrophoresis is the movement (*phoresis*) of a charged species under the influence of an applied electric field. The steady velocity u_E achieved by a particle of charge q in the field under the influence of the electric field of strength E is found from the momentum balance:

Fluid drag on particle = electrostatic force = qE

For globular particles, Stokes law can be used for the drag on the sphere moving in a Newtonian liquid viscosity[13]. In this study, electrophoresis is used to determine the charge on the particles under the applied electric field.

2.10 Contact Angle measurements

Contact angle measurement is a simple way to investigate surface character of any substrate by measuring the angle made by a drop of water or other liquid in contact with the surface.

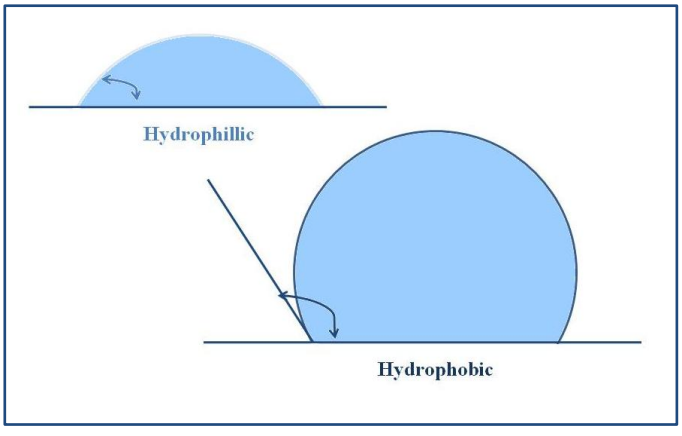

Figure 2.6. Schematic representation of water droplet on a hydrophilic and hydrophobic surface. The arrow represents the angle measurement made for determining the contact angle in both the cases.

Hydrophobic surfaces will repel a water droplet and generate a high contact angle. Conversely, on a hydrophilic surface, the water droplet will suspend on the surface and give rise to a low contact angle. (Figure 2.6)

The values are measured by means of a telescope mounted parallel to the surface. Air is generally considered to be a hydrophobic medium. Contact angles are extremely useful to for understanding both adhesion and biomedical compatibility. In this work, contact angles are primarily made to check the cleanliness of silicon wafers used as substrates for various purposes such as FTIR spectroscopy and sample preparations for AFM imaging, where the substrate has to be spotless to avoid artifacts in the acquired data.

2.11 References

1. Kemp, W. (1991) *Organic spectrosocpy*. Palgrave
2. Coates, J. (2000) *Encyclopedia of Analytical Chemistry*. John Wiley & Sons Ltd
3. Herschel, S.J. (1845) *Phil Trans Roy Soc (London)* 135, 143
4. Martin BR, R.F. (1979) *Quart Rev Biophys* **12**, 181
5. Lakowicz, J.R. (2006) *Principles of Fluorescence Spectroscopy*. Springer
6. Stokes, G. (1852) *Phil Trans R Soc (London)* 142, 463
7. Williams, D.B., and Carter, B.C. (1996) *Transmission Electron Microscopy*. Plenum Press
8. Oatley, C.W. (1972) *Scanning Electron Microscope: The Instrument*.
9. Binnig, G., *et al.* (1982) *Physical Review Letters* 49, 57
10. G. Binnig, H.R. (1986) *IBM Journal of Research and Development* 30
11. Binnig, G., *et al.* (1986) *Physical Review Letters* 56, 930
12. Einstein, A. (1905) *Ann. Phys. (Leipz.)* 17, 549
13. Bailey, J.E., and Ollis, D.F. (1986) *Biochemical Engineering Fundamentals*. McGraw-Hill Book Company

SURFACE FUNCTIONALISATION OF NANOPARTICLES USING BIOMOLECULES

Chapter 3

We report a novel synthesis route where we used an antibiotic cephalexin to reduce chloroauric acid. In this method colloidal gold capped by antibiotic in aqueous solution is readily prepared by a facile one-pot protocol. We have shown by a detailed investigation based on nuclear magnetic resonance and X-ray photoemission spectroscopy results, that the sulfur moiety present in the beta lactam is responsible for the dual role of reducing and capping (stabilizing) the gold nanoparticles. Interestingly, in this method, we could control the morphology of the gold nanoparticles from quasi-spherical to flat triangular flakes and finally to truncated triangles and hexagons by increasing the concentration of gold ions correspondingly. We believe that this synthesis route is a perfect model system to study the growth of the gold nanoparticles, which is elaborated in following chapter. In addition, antibiotics like cefaclor and ampicillin are also shown for their potential to form stable and active gold nanoparticles.
Also, in a different study of functionalisation, chemically synthesized iron oxide nanoparticles are functionsalised using the commercially important enzyme Penicillin G acylase as a means for immobilization and ease of separation after reaction with the substrate.

A part of the work presented in this chapter is published:

1. **Ramya Jagannathan,** Pankaj Poddar, &Asmita Prabhune. "Cephalexin-Mediated Synthesis of Quasi-Spherical and Anisotropic Gold Nanoparticles and Their in Situ Capping by the Antibiotic" *The Journal of Physical Chemistry C* **2009**, 111, 6933-6938.

Metal-ligand interactions are generally strong and result in robust entities.[1] Moreover, the incorporation of metal centers increases the scope of the functional properties of the nano-architectures that are designed allowing us to use various strategies based on their unique properties discussed in chapter 1. With the advent of advanced methods to synthesize various nanomaterials with excellent control over shape and size, finding their possible applications in biology and medicine has attracted growing attention. However, interfacing the nanomaterials such as metals, semiconductor quantum-dots, magnetic materials and their composites comes full of challenges and opportunities of exploring new methods to bind the nanoparticle surfaces with small molecules such as drugs, proteins, genes, etc. and to deliver them.[2, 3] Recently, semiconductor nanocrystals, originally researched for the use in electronic devices have found use as fluorescent probes in biological staining[4, 5] and diagnostics.[6] Similarly, magnetic nanoparticles, that were explored for their applications as magnetic storage devices, magnetic random access memories, etc. (since the last 6 decades) have also found excellent use in biomedicine as contrast enhancement agents for magnetic resonance imaging (MRI),[7] drug delivery,[8, 9] selective nano-probes for biomolecular interactions [10] and cell sorters.[11] (see Part II of this chapter)

This chapter is divided into two parts: Part 1 comprises of functionalisation of gold nanoparticles using cephalosporin antibiotics as an *in situ* reducing and capping agents, and Part 2 deals with the surface functionalisation of iron oxide nanoparticles with the enzyme Penicillin G acylase. The synthesis, characterization and their biological applications are studied. Specifically, the unique synthesis of the gold nanoparticles by cephalexin is studied in detail, which is explained in the following chapter 4.

3.1. Part 1: Synthesis of gold nanoparticles using antibiotics

Binding gold nanoparticle surfaces with drug molecules is attractive for several biomedical applications. Metal nanoparticles and their bioconjugates have already proved their potential in several biomedical applications. However, so far the processes of conjugating drug molecules, especially antibiotics, on metal nanoparticles remain a complex chemical synthesis involving multiple steps such as formation of metal nanoparticles, their surface modification and finally the capping

of drug molecules. In the present study, we have overcome these challenges by demonstrating a single-pot synthesis route as well as conjugation of the drug molecule at the nanoparticle surfaces without the use of unwanted chemicals.

Among several drug molecules, conjugation of a vast variety of antibiotics opens up a new field. This is especially interesting, as at present, this field is full of several challenges such as increasing the shelf life of these drugs, enhancing the chemical stability (especially at room temperature) and enhancing bioactivity against different microorganisms. Usually, the amount in which the antibiotics are administered into the body is very high, and efforts are undertaken to control their release (dose) and interaction with bacterial cells. However, until now, there are very few studies of binding antibiotics at metal nanoparticle surfaces and their efficient antimicrobial properties. [12] The interest in this field has especially grown in the past 3-4 years. Though it is well known that silver metal nanoparticles exhibit good anti-microbial activity[13], it was shown recently that vancomycin-capped Au nanoparticles show enhanced antibacterial activities and act as a rigid polyvalent inhibitor of vancomycin-resistant enterococci.[14] In this study, Gu et al devised a chemical route to produce Au@Van nanoparticles, which exhibit enhanced activities against VRE strains and Gram-negative bacteria. (See Figure 3.1) A similar result was reported for ciprofloxacin conjugated with Au/SiO2 core/shell NPs.[15]

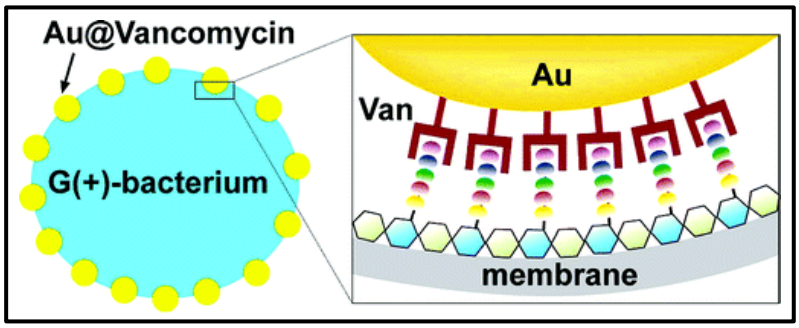

Figure 3.1. Schematic representation of vancomycin capped gold nanoparticles [From ref [14]]

"The energy with which surfactant molecules present in the growth medium adhere to the surfaces of growing nanocrystals is one of the most important parameters influencing crystal growth. The adhesion energy needs to be such that it allows dynamic solvation at the growth temperature: the surfactant needs to be able to exchange on and off the growing crystals, so that regions of the nanocrystal surface

are transiently accessible for growth, yet entire crystals are, on average, monolayer-protected to block aggregation. The classic paper of Murray, Norris and Bawendi[16] introduced this concept for the growth of CdSe nanocrystals in trioctylphosphine oxide (TOPO)." In this study, we have used a surfactant in a similar fashion; only that the surfactant is also acting as a reducing agent in the first phase to reduce the metal ions, and then these nucleate (small clusters), form seeds (with a single-crystal, singly twinned, or multiply twinned structure) and then the clusters aggregate to grow into nanocrystals in the presence of the surfactant that is acting as a capping agent in this phase of reaction.(see Figure 3.2) The role of the surfactant used here is an antibiotic. The applications of using an antibiotic is already listed above, in a previous study by Gu *et al.*[14]

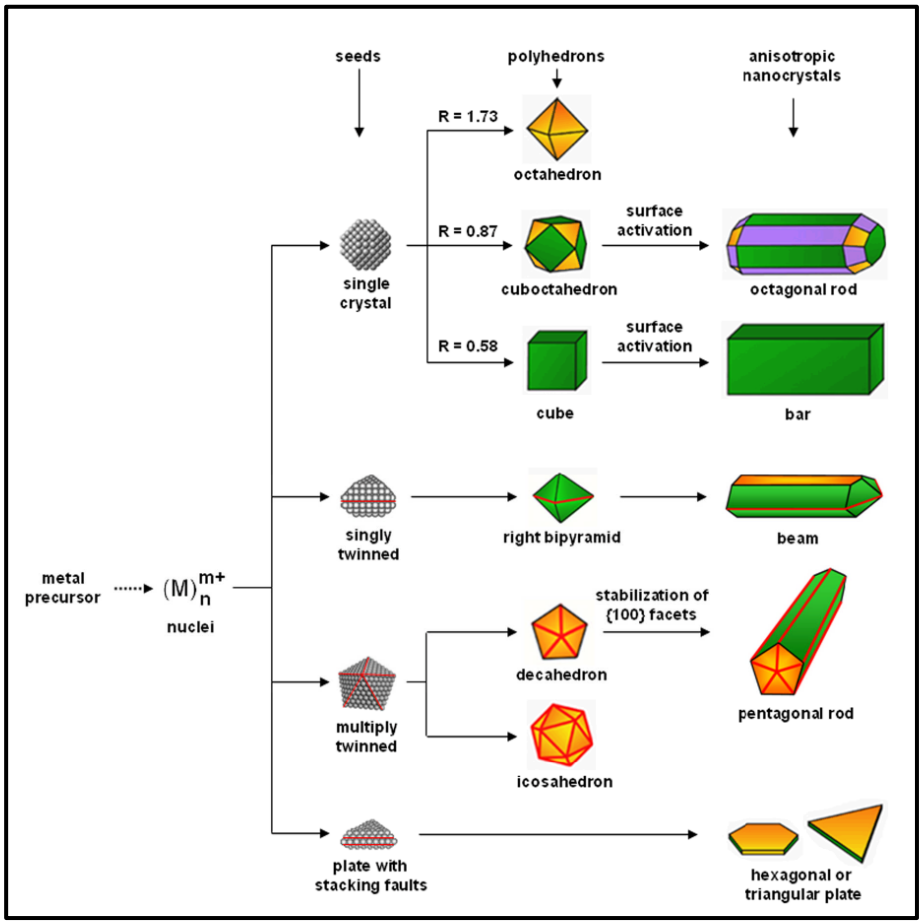

Figure 3.2. A schematic illustration of the reaction pathways that lead to fcc metal nanocrystals having different shapes. The green, orange, and purple colors represent the {100}, {111}, and {110} facets, respectively. Twin planes are delineated in the drawing with red lines. The parameter R is defined as the ratio between the growth rates along the <100> and <111> directions [Copied from ref[17]]

However, using antibiotics *in situ* is reported for the first time, and with the preliminary results that we have obtained, it seems promising for producing a tight controlled morphology of the particles, with good tuning of the kinetic and thermodynamic control parameters. For our study, we have used β-Lactam antibiotics.

Structurally, β-lactam antibiotics are based upon the four-membered nitrogen-containing beta-lactam ring that gives these agents their antibacterial activity. They can be divided into four groups - penicillins, cephalosporins, carbapenems and monobactams - on the basis of the molecular structures surrounding and supporting this active site. β-lactam antibiotics exert their antimicrobial activity by interfering with the enzymes specifically involved in peptidoglycan metabolism. These enzymes regulate cell walls, cell division, septation, elongation and cell shape and thus alter the surface morphology and structure of the bacteria.[18] Thus, β-lactam antibiotics, though bind to the bacteria through different modes, are very effective in their mode of action. Each β-lactam antibiotic has its own binding affinity for these enzymes, called penicillin-binding proteins, and these penicillin-binding proteins also vary among different bacterial species.

In this work, we have selected cephalexin, cefaclor and ampicillin, β-lactam antibiotics, as model systems to demonstrate a simple single pot synthesis of metal nanoparticles as well as their capping without the use of any unwanted chemicals. Cephalexin, cefaclor and ampicillin, the antibiotics used in this study have good activity against Gram-positive and Gram-negative microorganisms. Many Gram-positive microorganisms release relatively large amounts of β-lactamase into the surrounding medium, which can destroy the β-lactam antibiotics by hydrolysis of the β-lactam ring; this is the most prevalent mechanism of resistance.[19] The antibiotics that we have chosen are relatively resistant to these enzymes and have shown to interact with metal ions.[20] Cephalexin and cefaclor belong to a class of antibiotics called cephalosporins; they are similar to penicillin in action and side effects. They stop or slow the growth of bacterial cells by preventing bacteria from forming the cell wall that surrounds each cell. The cell wall protects bacteria from the external environment and keeps the contents of the cell together. Without a cell wall, bacteria are not able to survive.

While choosing a proper candidate for the conjugation of antibiotic with metal nanoparticles among various nanomaterials, gold is a very promising and useful element. Various factors affect the physical and chemical nature of the material; most importantly, the properties of gold depend on the size of the assembly of atoms. While every element is unique in some respects, gold occupies a position at one extreme of the range of metallic properties, and its legendry chemical inertness in bulk and activity in nano, is attributable to chemical features that are not surpassed by any other metal. Gold is a particularly excellent candidate for conjugation as its cytotoxic effects are relatively better documented[21] and these particles are capable of binding readily to a range of biomolecules such as amino acids, proteins/enzymes and DNA and expose large surface areas for immobilization of biomolecules.[22-26] At today's pace of nanoscience and nanotechnology, gold nanoparticles (Au NPs) have served as a versatile platform for exploring many facets of basic science. An important aspect of Au NPs has been the breadth of their impact; applications range from photonic device fabrications, to sensing of organic molecules and biomolecules, to charge storage systems. Although gold has been known to be inert for centuries, it was an exciting discovery then when Haruta and Hutchings simultaneously and independently[27, 28] showed that gold could be very active, in particular, for the heterogeneous low-temperature oxidation of CO. After detailed electron microscopy studies, it was found that the catalysis was due to some small gold nanoparticles, approximately 2-4 nm in diameters.

Au NPs offer surfaces that can be selectively passivated. Though the reasons are unclear, this offers ease of engineering as per our need. Figure 3.3 shows the controlled synthesis of various shapes of Au NPs for various uses. A myriad of research articles and work is present on Au NPs today. This is in large due to the unique and often tunable properties of Au nanocrystals that include Localized Surface Plasmon Resonance (LSPR), biocompatibility, and easy surface modification.

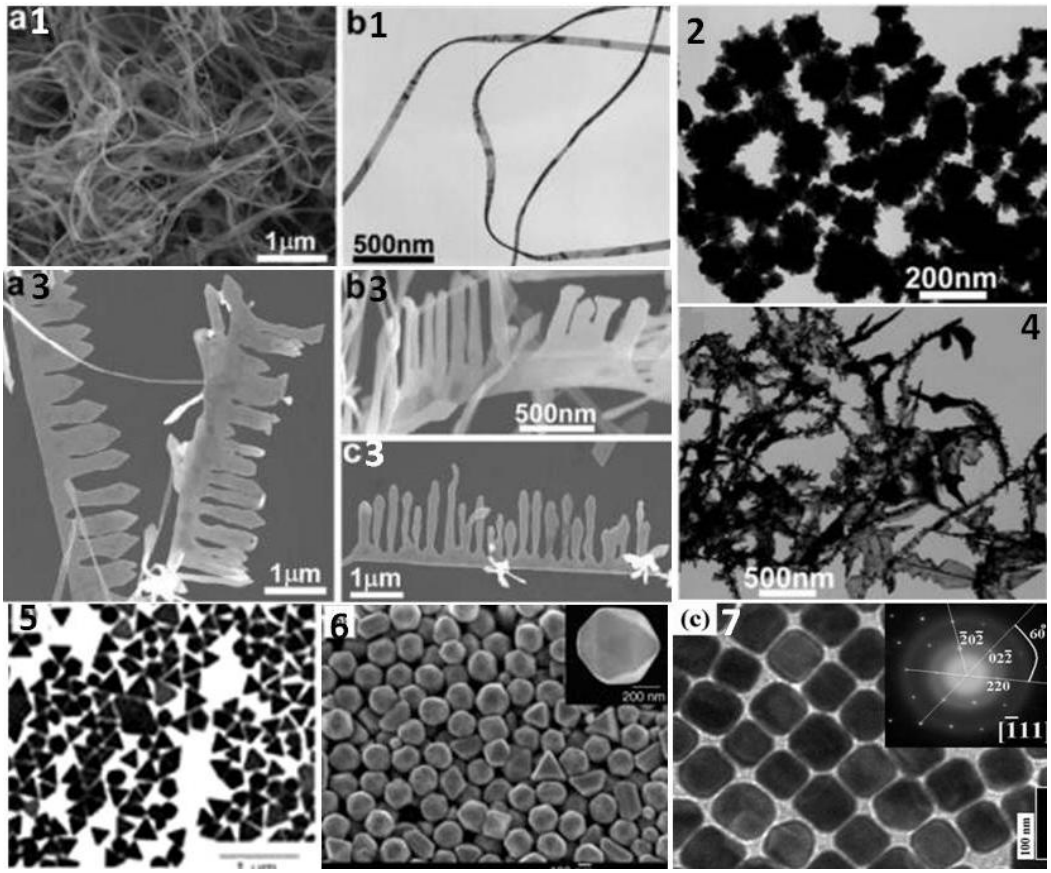

Figure 3.3. Different shapes of gold nanoparticles. **(1a)** and **(b1)** shows representative SEM and TEM images of the gold product obtained at 4 °C consisting of very flexible, 1D belt-like single crystal grown along <110> direction from ref [29]; **(2)** TEM images of gold nanostructures obtained at 4 °C in aqueous solutions of single Surfactant 1.0 mM SDSn;[29] **(a3) (b3) (c3)** SEM images of gold nanocombs obtained by a two-step process with temperature changing from 4 to 27 °C from ref [29]; **(4)** TEM image of gold nanostructures synthesized similar to **(2)** with surfactant of 6.5 mM CTAB; **(5)** TEM image of truncated tetrahedral gold nanocrystals and **(6)** Icosahedral nanocrystals showing clearly all (111) facets of a typical icosahedron. from ref [30] and **(7c)**TEM image of gold nanocube obtained electrochemically; inset shows the SAED pattern of individual nanocube by directing the electron beam perpendicular onto one of its square faces.[31]

When combined together, Au nanocrystals represent an ideal platform for chemical and biological sensing as well as applications in nanomedicine. For example, the immune-Au NPs, with antibodies as the coating, serve to probe the presence and position of antigens on cell surfaces as well as to potentially deliver therapeutic agents selectively. The cytotoxicity and immune-toxicity effects of Au NPs are also well-established. [21, 32]

3.1.1. Synthesis of gold nanoparticles using cephalexin

We herein report the reduction of gold ions using antibiotics such as cephalexin to form a stable suspension of eco-friendly gold nanoparticles in aqueous medium at room temperature. Cephalexin (MW 347.39) (8-(2-amino-2-phenyl-acetyl)amino-4-methyl-7-oxo-2-thia-6- azabicyclo[4.2.0]oct-4-ene-5-carboxylic acid), a β-lactam antibiotic, is relatively resistant to these β-lactamases and has also shown to interact with metal ions.[12] In our study, the antibiotic readily reduces choloauric acid into gold nanoparticles. We believe that these results enhance numerous possibilities of conjugation chemistry wherein we can tag our desired drug molecule onto the nanoparticle surface. We have performed detailed NMR and XPS studies to analyze the functional groups responsible for binding and reduction of gold ions. To the best of our knowledge, this is the first time that an antibiotic has been used to perform a controlled synthesis of gold nanoparticles.

3.1.1.1. Experimental details

For the synthesis of gold nanoparticles, we tried the reduction of various concentrations of chloroauric acid by adding a broad range of concentrations of cephalexin (a kind gift to us from Lupin Laboratories, India), which helped us in determining the optimum concentration of both chloroauric acid and cephalexin for the formation of gold nanoparticles by measuring the absorbance in the UV-NIR region at different time intervals. We observed that at room temperature (30 °C), the reduction of chloroauric acid at the concentrations of 1×10^{-4}, 1.5×10^{-4}, and 2×10^{-4} M, after adding 10^{-5} M (working concentration) cephalexin, takes place in an hour. The particle solution was quite stable without aggregation or precipitation. All chemicals and materials were obtained from Sigma-Aldrich Chemicals and used as received unless otherwise mentioned. After the addition of antibiotics and aging the colloidal gold solutions for 1 h, we dialyzed the solution to remove any unbound antibiotic molecules as well as unreduced gold ions by using a cellulose tube (MW cutoff 12 400 D) against 1 L of deionized water for 9 h at 30 °C. We repeated the dialysis process to make sure the removal of unbound antibiotic molecules as well as unreduced gold ions was complete. To estimate the amount of antibiotic in the dialyzed water, we used the standard curve of absorbance at 262 nm (due to the ð-ð*

transitions of phenyl ring) of different concentrations of cephalexin in solution as an indicator.

3.1.1.2. Results and Discussions

We show time-dependent UV-vis-IR spectra of the antibiotic capped gold hydrosol in the top, middle and bottom panels of Figure 3.1, prepared at three different concentrations of chloroauric acid: 1 x 10^{-4}, 1.5 x 10^{-4}, and 2 x 10^{-4} M, respectively. The reactions were carried out at room temperature (30 °C). From the top panel (Figure 3.4A) it is clear that all the curves show well-defined sharp absorption peaks at 545 nm, which do not shift significantly even after 5 h of reaction (curve 5). Additionally, it can be noticed that after the initial 1 h of reaction, there is an abrupt rise in the peak intensity. However, after 2 h of reaction, further increment in the peak intensity is not so prominent. The absence of longitudinal surface plasmon resonance peaks indicates isotropic morphology of the particles at this concentration (1 x 10^{-4} M). We further observed that the cephalexin-reduced gold nanoparticles are very stable and do not aggregate even after several days. Additionally, the dried nanoparticles are re-dispersible in water indicating the presence of capping molecules at their surface.

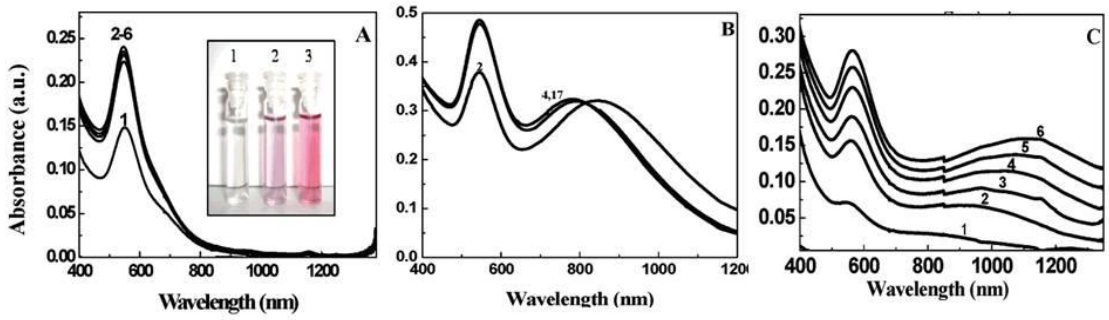

Figure 3.4. Time-dependent UV-vis-NIR spectra of cephalexin reduced gold nanoparticles from various concentrations of chloroauric acid (e.g., curves 1-6 correspond to 0-5 h, respectively, at each 1 h interval): top panel, 1 x 10^{-4} M; middle panel, 1.5 x 10^{-4} M; bottom panel, 2 x 10^{-4} M. The inset of the top panel: sample 1 is chloroauric acid, sample 2 is cephalexin-reduced gold nanoparticles (Au salt concentration = 2 x 10^{-4} M), and sample 3 is 7-amino cephalosporinic acid (7-ACA)-reduced gold nanoparticles (Au salt concentration = 2 x 10^{-4} M).

To further explore the dependence of reaction kinetics on concentration, we tried the synthesis with an increased concentration of gold ions (1.5×10^{-4} M). The results are presented in Figure 3.4B. In contrast to the curves shown in Figure 3.4A, it should be noticed that another broad peak is observed in the near-IR region, which was absent in the previous case. This peak becomes more prominent with the increase in the reaction time. The peak in the near-IR region indicates the presence of anisotropic gold nanostructures giving rise to longitudinal modes of surface plasmons. In Figure 3.4C, we have presented the absorption spectra for the gold nanoparticles synthesized with 2×10^{-4} M gold ions. Here we observed that near-IR peaks are shifted and broadened as compared to the peaks for the particles synthesized with 1.5×10^{-4} M gold ions.

In Figure 3.5, we have presented representative TEM micrographs of cephalexin-reduced gold nanoparticles for various concentrations of gold ions. Images presented in the top panels (Figure 3.5, parts A and B) show the particles corresponding to the synthesis with 1×10^{-4} M gold ions. The particles in these images are predominantly quasi-spherical with particle sizes in the range from 20 to 70 nm. The middle panel (Figure 3.5, parts C and D) shows images corresponding to 1.5×10^{-4} M. Here, it is interesting to notice the presence of a few anisotropic structures (mostly triangles), along with the quasi-spherical particles, which is consistent with the UV-vis-IR spectra.

We have shown the images of particles corresponding to 2×10^{-4} M concentration of Au ions in the bottom panels (parts E and F) of Figure 3.5, where the following features can be noticed in contrast to the particles synthesized using the lower concentrations of gold ions: (a) bimodal particle size distribution, with a broad coexistence of smaller particles (size range 50-80 nm) and much bigger particles (size range 120-200 nm), (b) spherical particles that are much larger in size in comparison to the nanoparticles shown in Figure 3.5, parts A and B, and it is noticed that almost all of these particles are faceted, thereby losing their spherical morphology, unlike the particles synthesized by smaller concentrations of gold ions, (c) the presence of truncated triangles and hexagons, and (d) the presence of larger particles with lighter contrast indicating that the larger particles are plate-like with well-defined sharper facets. Overall we observe that for all the concentrations, the particles are well separated and stabilized. The mechanism of bimodal distribution of

particles is well explained in the literature, which is known to be highly concentration dependent.[33] The bimodal distribution is generally achieved when the nucleation and growth occur in parallel. Usually, by allowing a fast nucleation or the Ostwald ripening process, a uniform distribution of particles is achieved.

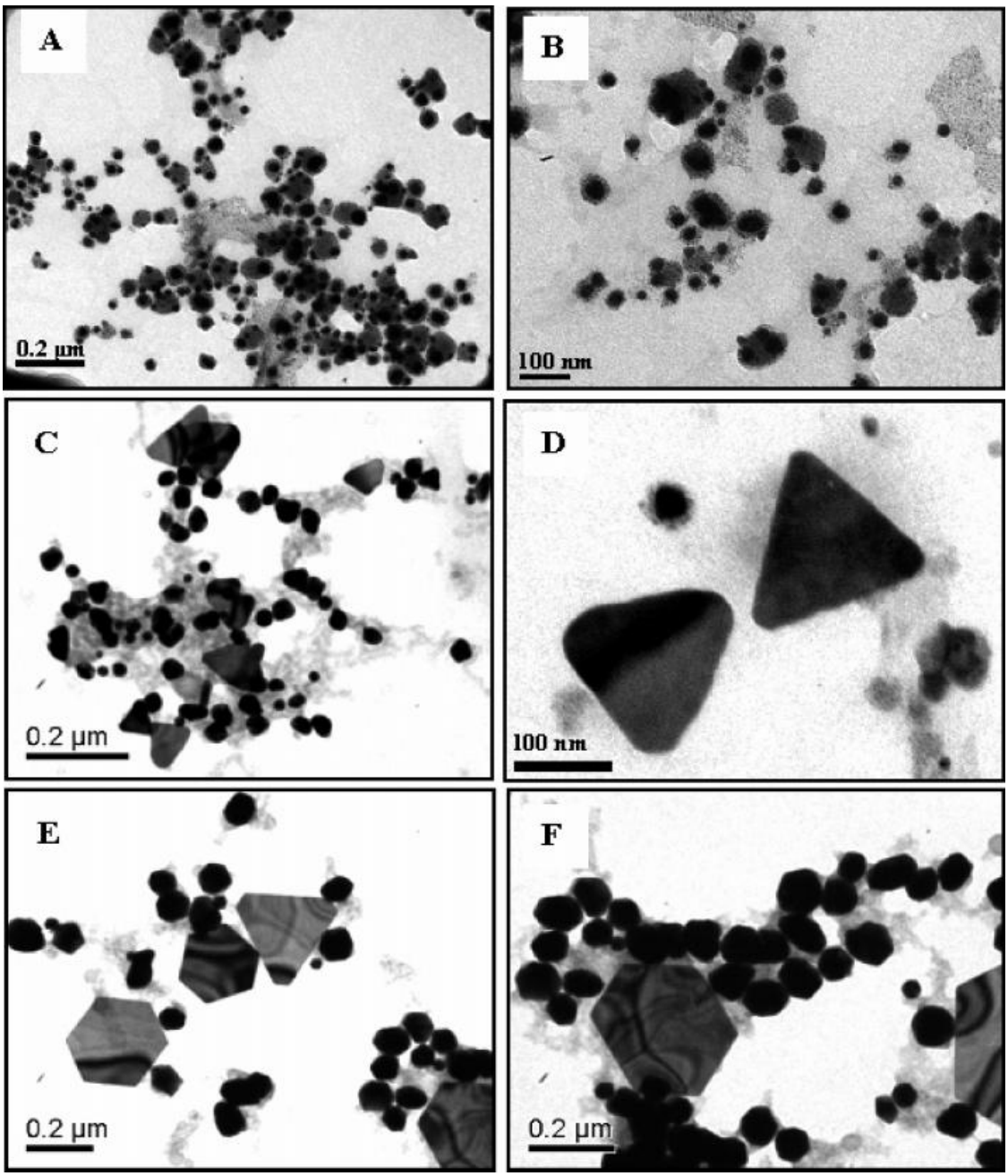

Figure 3.5. Transmission electron micrograph of as-synthesized Au nanoparticles. Images in the top, middle, and bottom panels show the particles synthesized with Au ion concentrations of 1 x 10^{-4}, 1.5 x 10^{-4}, and 2 x 10^{-4} M, respectively.

On the other hand, if the process of nucleation is kept controlled at the initial stage (by stopping it after some time), allowing only the growth of already formed nuclei, we can achieve better size distribution. The concentration-dependent synthesis of faceted spherical particles and other anisotropic structures, in our case, is also quite interesting. It is known from previous studies that particle shapes are dependent on various reaction parameters such as gold ion concentration, surface binding with different ligands and temperature.[34] It is also known that a faster reduction yields dominantly spherical particles; on the other hand slower reduction yields anisotropic or faceted structures in the form of rods, triangles, hexagons, etc. The reaction rate, itself, is known to be directly influenced by the concentration of gold ions. However, the contribution of other parameters such as type of ligands binding to initially formed nuclei (which may promote or restrict the growth of specific lattice planes resulting in the formation of anisotropic structures) is also important. The pH change during the reaction at room temperature was measured and found that no observable change is detected. It could thus, also be inferred that the changes in size and shape of the gold nanoparticles, at various concentrations and temperatures, while studying the nucleation and growth is not remarkedly affected by the pH change, at a constant temperature. It is also known that the crystallographic phase of the nuclei formed governs the final shape of the nanocrystals.[34]

In Figure 3.6, we have plotted the XRD data as obtained on 2 x 10^{-4} M, which shows the most intense peak at 2Θ = 38° corresponding to (111) planes. Other peaks are nonexistent, which in fact provides a clear indication that particles are single crystalline with plate-like structures.

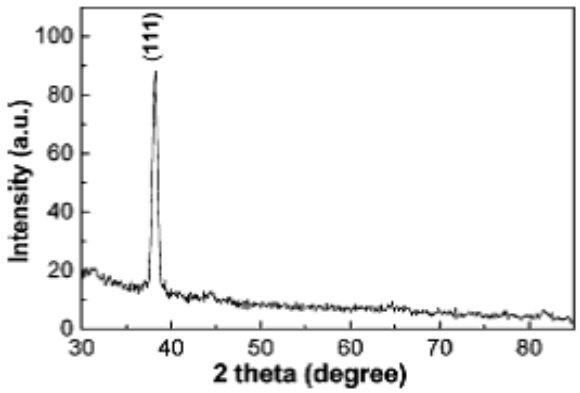

Figure 3.6. X-ray diffraction pattern of as-synthesized gold nanoparticles.

These observations are consistent with TEM images (Figure 3.5, parts E and F). Here it is quite interesting to explore the following aspects: (i) the reason behind the stability of the particles, (ii) the functional groups in cephalexin responsible for the reduction of gold ions, (iii) the origin of the presence of anisotropic structures with increasing concentration of gold ions, and (iv) the functional groups responsible for binding with the surface. To explore the role of the presence of surface charge at the as-synthesized gold nanoparticles, we performed gel electrophoresis measurements, which confirmed that the cephalexin capped nanoparticle surfaces are negatively charged.

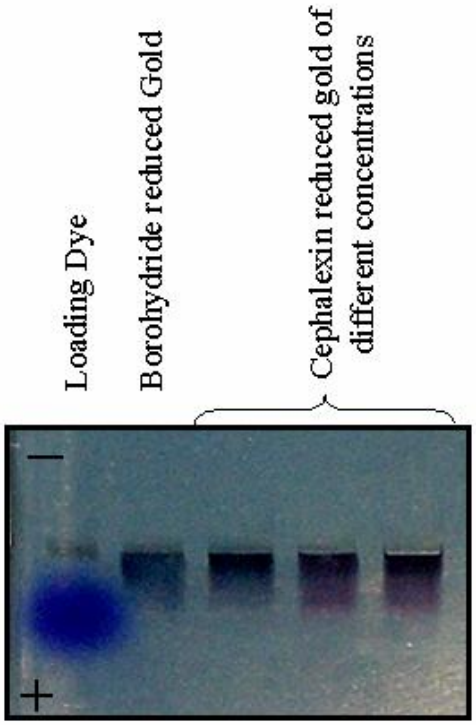

Figure 3.7. Electrophoresis of nanoparticles.

Any metal nanoparticle in solution (colloids, metal sols, regardless of the metal, and semiconductor nanoparticles) have double layers with ionic surface excesses on the solution side that reflect any net electronic charge residing on the metal nanoparticle surface (or its capping ligand shell). Therefore, the nanoparticles were concentrated by centrifuging and were subjected to electrophoresis (0.8% agarose gel) in 1X TAE buffer. The Figure 3.7 below shows the migration of the nanoparticles towards anode after 90 min under an electric field at 30 V (with respect to the bromophenol blue dye reference) showing that they are negatively charged.

In the light of this observation, we believe that surface charge and/or surface capping might be playing a role in the stabilization of these particles. It should also be noted here that these particles are fairly re-dispersible in water from dried powder. To further study the mechanism in detail, as a preliminary test, we also tried to synthesize these particles by using two precursor molecules of the semi-synthetic antibiotic cephalexin (Figure 3.8A): 7-ACA (7-amino cephalosporinic acid) and phenyl glycine, whose structures are shown in Figure 3.8, parts B and C, respectively.

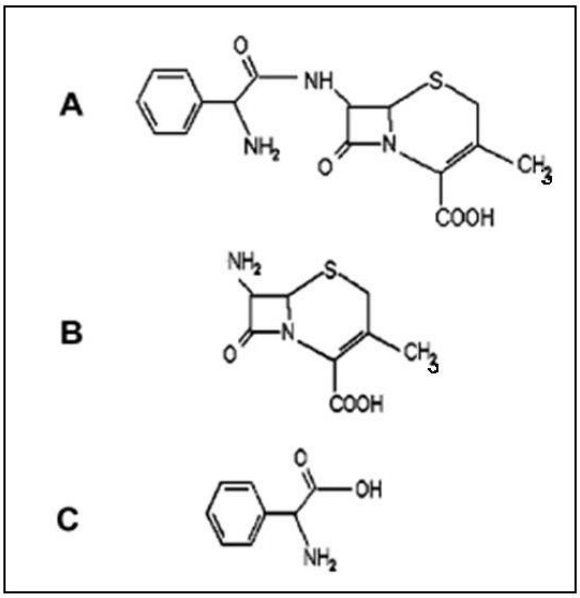

Figure 3.8. Chemical structure of (A) cephalexin, (B) 7-amino cephalosporinic acid (7-ACA), and (C) phenyl glycine molecules.

We noticed that the gold ions are reduced into a ruby-red suspension (Figure 3.4A inset, vial 3) of highly stable gold nanoparticles with 7-ACA alone (Figure 3.9), but phenyl glycine does not reduce the gold ions in the same concentration used for cephalexin.

From these observations, it could be inferred that the primary amine group present in the cephalexin may not be responsible for the reduction. Here it seems that the sulfur moiety which is present in both 7-ACA and cephalexin but absent in phenyl glycine might be playing a role in the reduction process.

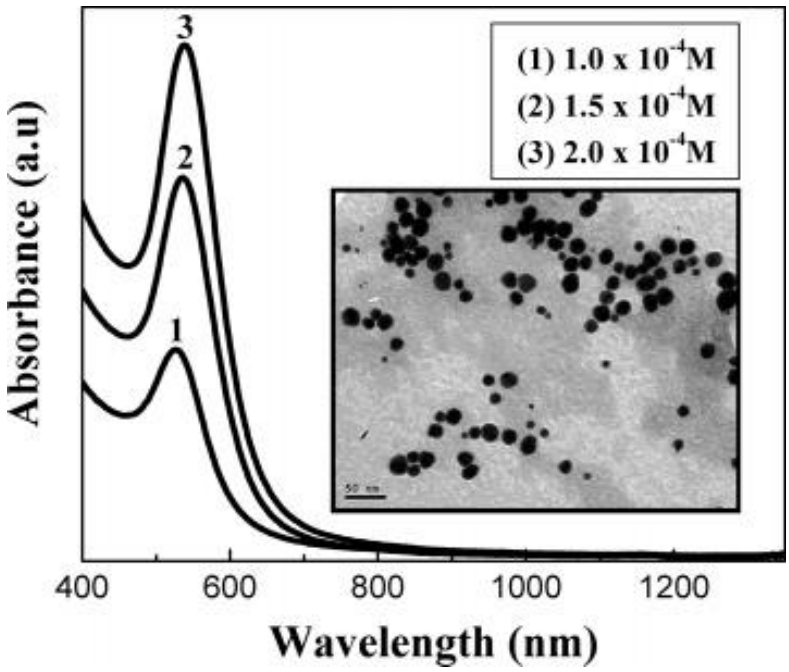

Figure 3.9. UV-vis-NIR absorption spectra of various concentrations of gold ions reduced by 7-amino cephalosporinic acid (7-ACA). The inset shows the TEM micrograph of the as-synthesized particles.

Vibrational spectroscopy was obtained for the samples; however, conclusive data could not be obtained from the IR-spectrum (Figure 3.10) because of weak bands due to low concentration of the biomolecule on the metal nanoparticle. A number of bands can be clearly seen in curve 1. The carbonyl group in the β-lactam ring occurs as a broad band centered at ca. 1780 cm^{-1}, free carboxyl group at 1700 cm^{-1} and the carbonyl in amide linkage at 1650 cm^{-1} respectively. However, we observed a remarkable change in the FTIR spectra after the formation of gold particles.

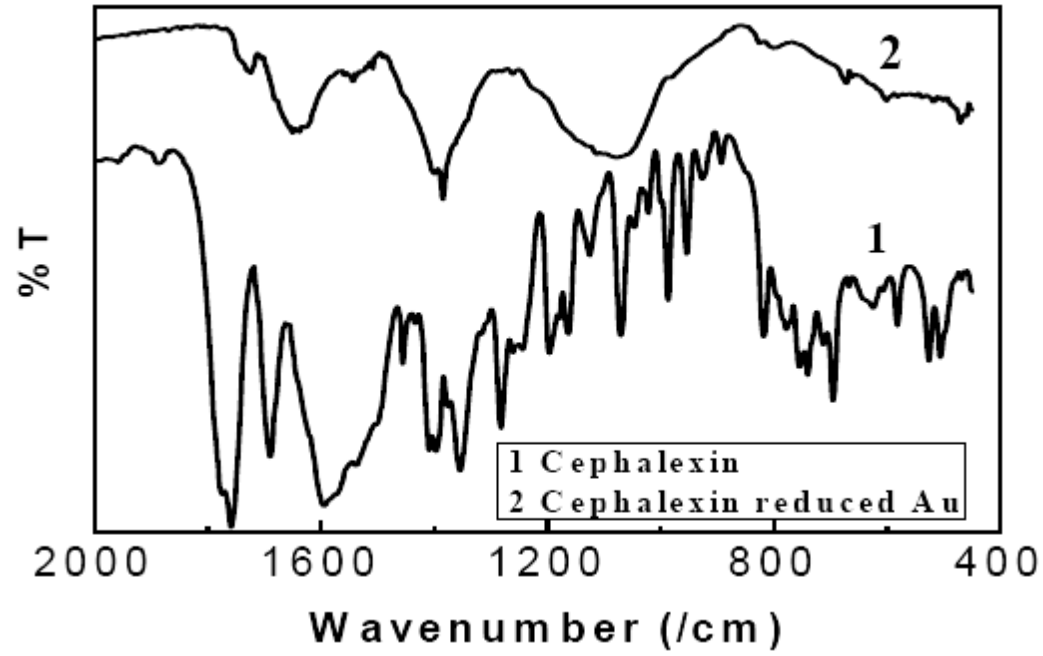

Figure 3.10. FTIR spectra of (1) cephalexin (2) gold nanoparticles bound with cephalexin.

The characteristic features of cephalexin are not evident which may be because of extremely low working concentration of the molecule, cephalexin on the nanoparticle or the molecule may be broken as a result of the oxidation of the lactam ring. The data from this FTIR is not conclusive. In an effort to further analyze the mechanism and also to see the effect of oxidizability of the lactam ring, we took ^{1}H NMR spectra of the nanoparticles as well as cephalexin. In the ^{1}H NMR spectra of cephalexin (Figure 3.11), we could assign all the peaks of the molecule as listed: ^{1}H NMR (400 MHz, D_2O): δ 1.86 (s, 3H), 3.03 (d, 1H, J = 17.95 Hz), 3.46 (d, 1H, J = 17.86 Hz), 5.05 (d, 1H, J = 4.29 Hz), 5.22 (s, 1H), 5.65 (d, 1H, J = 4.29 Hz), 7.54 (m, 5H).

As evident from the above NMR spectrum, the cephalexin used in the study is pure and free from any other contamination. In Figure 12, we have shown ^{1}H NMR spectra of the reduced gold nanoparticles, and the peaks of the oxidized cephalexin bound gold nanoparticles are assigned as below: 1H NMR (400 MHz, D_2O): δ 2.03 (s, 3H), 3.23 (1H, broadened), 3.59 (1H, broadened), 5.25 (1H), 5.70 (1H), 7.56 (m, 5H). The oxidizability of the lactam ring, present in cephalexin (which has been

well-studied earlier[35]), could be responsible for this reduction of chloroaurate ions into anisotropic nanoparticles.

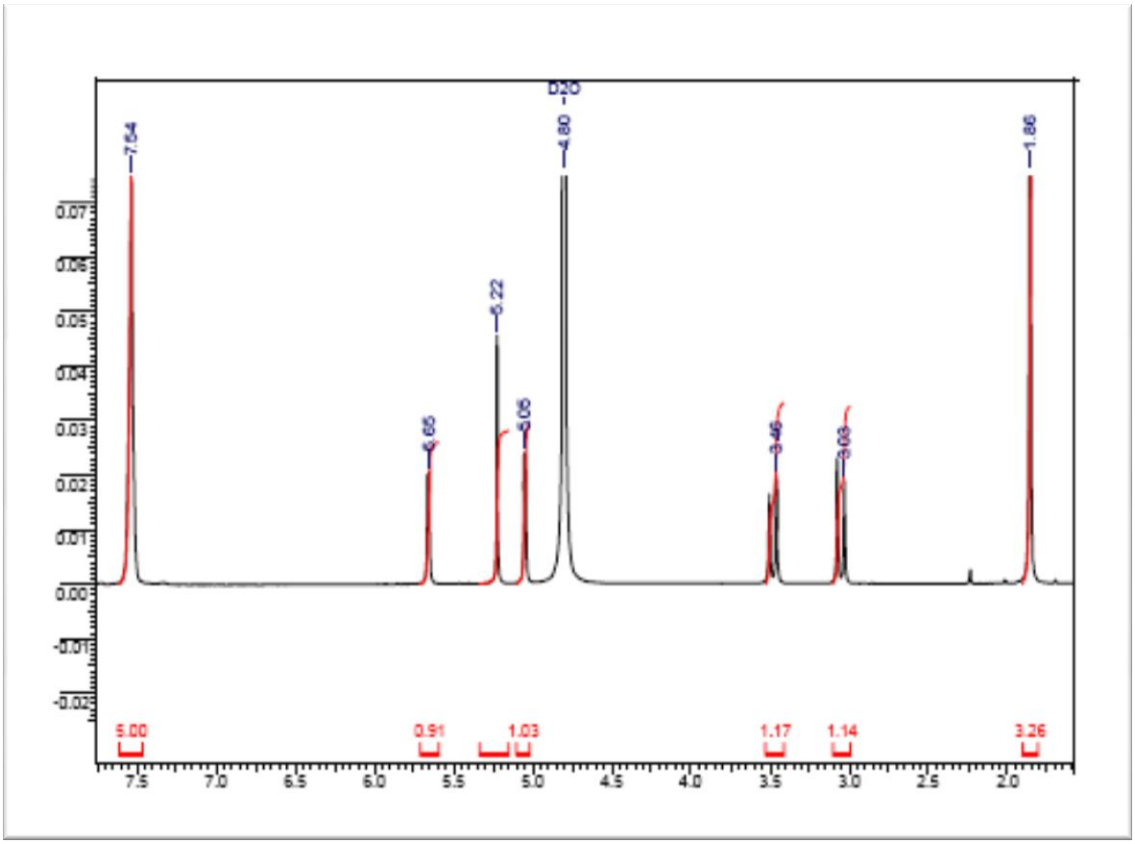

Figure 3.11. ^{1}H NMR spectrum of cephalexin.

This assumption is supported by the observation that the ^{1}H NMR spectra of oxidized cephalexin with nanoparticles shows an absence of an active proton signature (R to the N atom in the lactam ring), which gives a doublet at around 5.05 ppm in the cephalexin ^{1}H NMR. The broadening of 3.03 ppm (S-CHH) and 3.46 ppm (S-CHH) can be attributed to their presence near the sulfur atom that is known to bind readily with Au nanoparticles formed *in situ*.

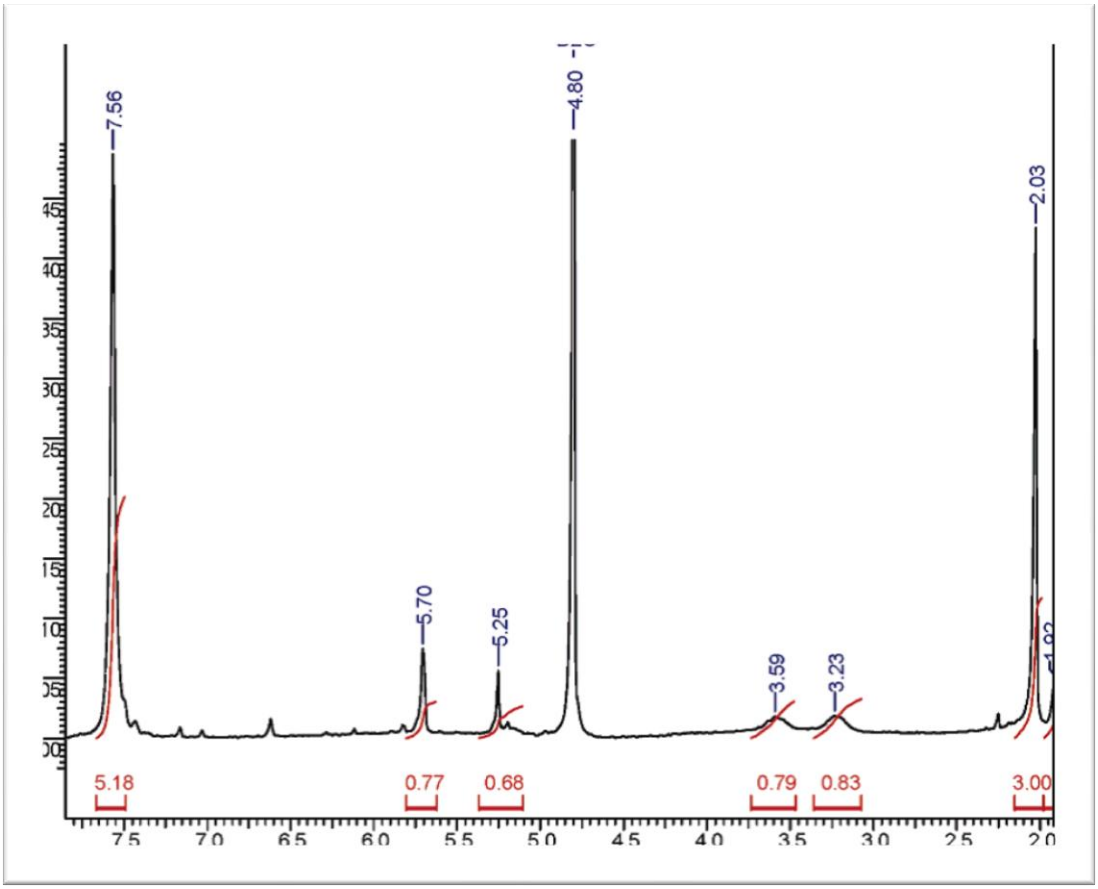

Figure 3.12. ^{1}H NMR spectrum of gold nanoparticles reduced by cephalexin.

However, by using ^{1}H NMR, we could not establish the amine's role in stabilizing nanoparticles, owing to the exchange reaction taking place in solvent D_2O where amine-proton signatures are not seen. Further chemical analysis of cephalexin-reduced gold nanostructures was performed by XPS and compared with the XPS spectra of cephalexin. The results are presented in Figure 3.13, where the panels in the left column (A-D) represent spectra for C 1s, N 1s, O 1s, S 2p obtained from cephalexin alone. Panels in the right column (E-I) in the same figure show spectra corresponding to C 1s, N 1s, O 1s, S 2p, and Au 4f core levels, respectively. As-obtained XPS core level spectra were background corrected using the Shirley algorithm, and chemically distinct species were resolved using a nonlinear least-squares fitting procedure. The core level binding energies (B.E.) were aligned with the carbon B.E. of 285 eV. As is clear from Figure 3.13, parts A and E, the C 1s core level spectra could be resolved into four components situated at around 283, 285, 286.5, and 288.6 eV B.E. Here the peak at 285 eV is due to electrons from saturated

hydrocarbons, whereas the peaks at 286.5 and 288.6 eV can be assigned to –COOH groups and R-carbon bound to -COOH and -NH_2 groups present in the cephalexin molecule, respectively. The peak with the smallest intensity situated at 283 eV is assigned to carbon present in the aromatic ring. Figure 3.13, parts B and F, shows the spectra from the O 1s core level situated at 532 eV without any change, which indicates that even after the reaction the electronic environment of O atoms in the cephalexin molecule is not changed. In Figure 3.6, parts C and G, we have plotted N 1s core level spectra, which show two peaks each situated around 400 and 401.6 eV, respectively, which may be due to two different N atoms in the cephalexin molecule with different electronic environments. As we did not observe any significant shift in the B.E.'s of peaks corresponding to N 1s before and after the reaction, we conclude that nitrogen may not be responsible for binding with the gold nanoparticles in the present case. In Figure 3.13, parts D and H, we have presented S 2p core level spectra.

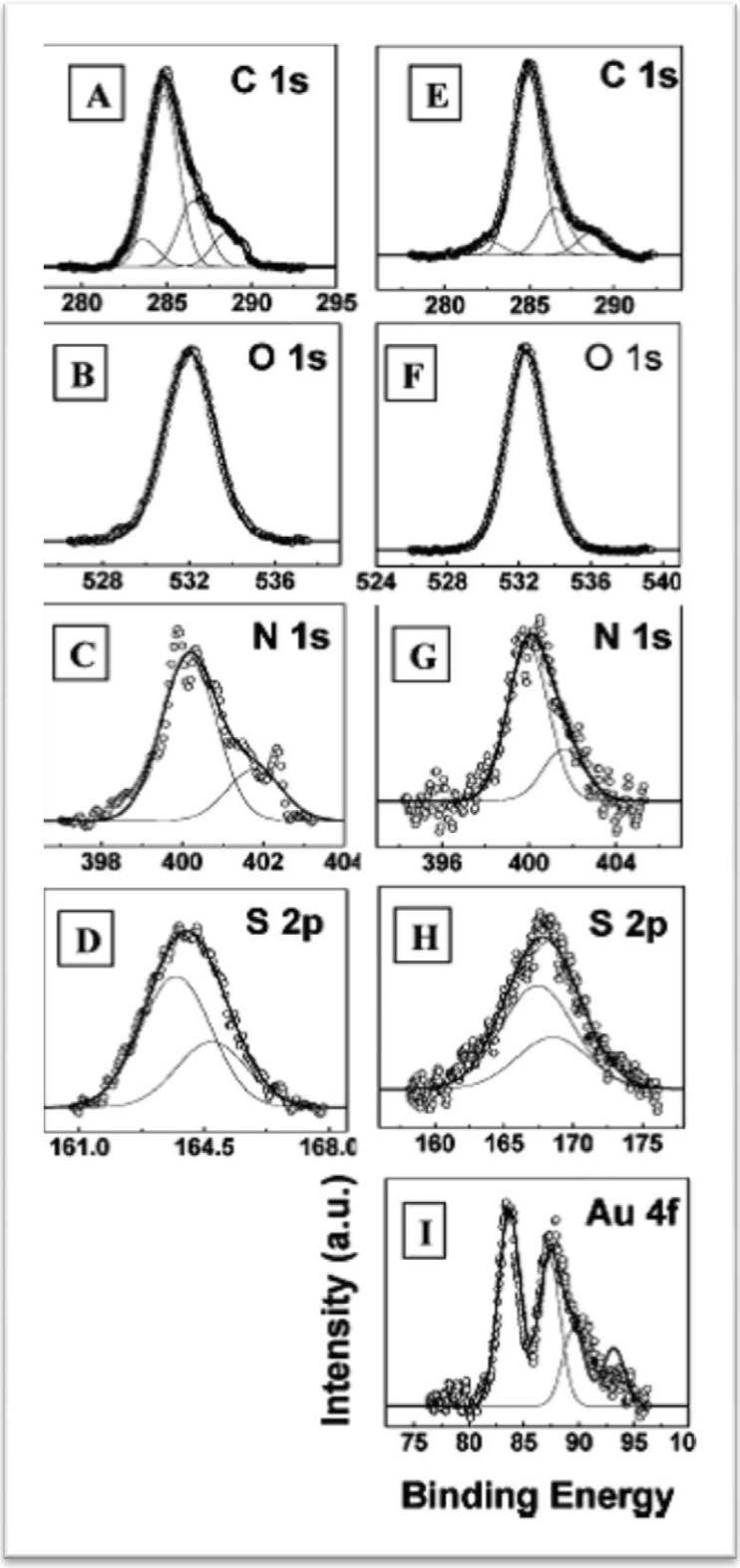

Figure 3.13. X-ray photoelectron spectroscopy data for cephalexin (panels A-D) and cephalexin-reduced gold particles (panels E-I).

In Figure 3.13D (for cephalexin), the main peak at a B.E. of 164 eV could be resolved into two peaks situated at 163.7 and 164.7 eV assigned to $2p_{3/2}$, and $2p_{1/2}$, respectively. On the other hand, for the gold nanoparticles bound with cephalexin, the peak corresponding to the S 2p core level is situated at 168 eV and could be resolved into two peaks at 167.5 and 168.5 eV, also assigned to $2p_{3/2}$, and $2p_{1/2}$, respectively. The large shift toward higher B.E.'s for sulfur indicates possible oxidation at this site after the synthesis of gold nanoparticles indicating that sulfur (instead of nitrogen) might be playing a significant role here in the reduction/binding process. These results obtained from the N 1s and S 2p core level spectra are consistent with our previous observations based on the synthesis using 7-ACA and phenyl glycine molecules that the amine group may not be responsible in synthesis/binding. In Figure 3.13I, we have presented the Au 4f core level spectrum which shows four peaks situated at 83.7, 87.5, 89.6, and 93.1 eV. The peaks at 83.7 and 87.5 eV are attributed to $4f_{7/2}$ and $4f_{5/2}$, respectively, from Au^0. The peaks situated at higher B.E. with relatively lower intensity are probably due to the unreduced Au ions. Here, we took additional care to remove unreacted gold ions by dialyzing the particles; however, the trace amount of gold ions still present in the solution might give rise to this peak. In the light of the fact that ions themselves may be responsible for the antimicrobial activity, it should be noted that it is important to completely remove them to observe the activity from the gold nanoparticles capped with cephalexin. It is generally known that amine derivatives[36-40] and thiol groups[41-43] have strong binding to the gold surface, but our XPS analysis and other experiments do not support the fact that amine group might be playing role here.

We next addressed whether these nanoparticles showed any anti-bacterial activity *per se*. This is included in section 1.4.

3.1.2. Synthesis of gold nanoparticles using cefaclor

Here, we have used cefaclor, (MW 367.80) ((6R, 7R)-7-[(2-amino-2-phenylacetyl)amino]-3-chloro-8-oxo-5-thia-1-azabicyclo[4.2.0]oct-2-ene-carboxylic acid) a potent antibiotic, similar to cephalexin, except with a chlorine atom instead of the methyl group in the 3rd position of the lactam ring. In the previous case of Au NP synthesis by cephalexin, we had shown that the sulfur moiety in cephalexin is responsible for the formation of stable Au NPs. However, cefaclor, though

homologous, shows a presence of an –I group (Cl) instead of +I group (CH_3). (See Figure 3.14) Due to –I effect of Cl, the electrons on the sulfur would be less available for the reduction. This makes it an interesting study of cefaclor as a potent candidate for synthesizing Au NPs. It would not only be challenging, but also provide a good platform for a comparative study of the morphology of particles formed in both cases. Moreover, cefaclor belongs to second generation cephalosporins; whereas cephalexin is in the first generation (classification of generation is on the basis of activity difference, increasing activity relates to increasing order of generation).

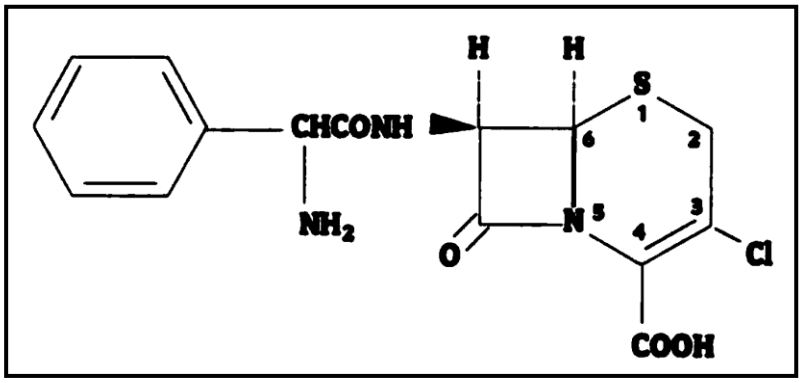

Figure 3.14. Structure of cefaclor.

Concentration dependent studies of cefaclor synthesized gold nanoparticles showed unique morphologies of the particles. In solution phase, the shape of the product formed during the nanocrystals growth drastically changes temporal and spatioselective manner. This deviation from the predicted morphologies can be attributed to a number of scenarios that may include:

i) the equilibrium condition never being reached during synthesis;

ii) the surface energies for various facets being different due to anisotropic interactions with the capping agent, impurity, or solvent;

iii) twin defects being included during nucleation and growth to form shapes such as decahedron and icosahedron with a total free energy lower than that of the Wulff polyhedron[44] (a truncated octahedron, in an inert gas or vacuum i.e. strictly speaking only valid at 0K); and

iv) use of an elevated temperature for the synthesis.

For these reasons, it is not hard to understand why solution-phase syntheses are inherently more powerful and versatile (at the same time, more complicated) than vapor-phase methods for generating metal nanocrystals of different shapes.[17]

It is well known that the final shape of the nanoparticle depends on the internal structure of the seed, where structure fluctuation is no longer possible, and the binding affinity of the capping agent. Although many mechanisms explain how different shaped nanocrystals are formed[45-48] other growth mechanism needs to be explained as unique morphologies are observed in our study.

3.1.2.1. Experimental details

The experimental details are as described in case of cephalexin, except the concentrations vary in each case, as mentioned.

3.1.2.2. Results and Discussions

Figure 3.15 shows the UV-visible spectrum of gold nanoparticles synthesized at different concentrations of cefaclor and chloroauric acid, similar to the spectrum shown for cephalexin reduced gold nanoparticles. Here also we observe evolution of anisotropy as the concentration of gold ions is increased from Figure 3.15 (A) to (C). As described before, it is known that anisotropic gold nanoparticles normally exhibit two principle surface plasmon resonance (SPR) absorption peaks characteristic of the short (transverse band) and long (longitudinal band) axes.[49]

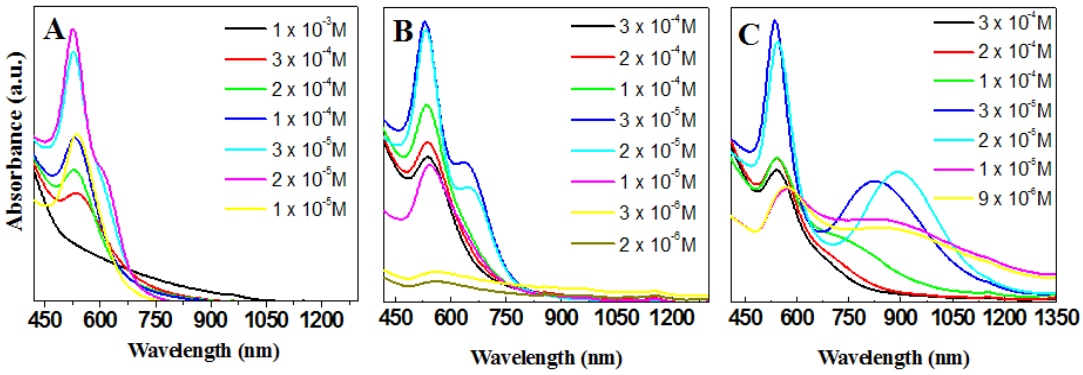

Figure 3.15. UV-visible spectrum of gold nanoparticles synthesized at different concentrations of cefaclor and chloroauric acid. Chloroauric acid concentration is constant in each graph, at (A) 1 x 10^{-4}M, (B) 1.5 x 10^{-4}M and (C) 2 x 10^{-4}M. Varying concentrations of cefaclor are given in each case.

The color due to surface plasmon resonance was observable within 1 h of the reaction at a temperature of ~ 30 °C; more quickly so at non-anisotropic growths. At other concentrations, which are not shown here, the gold nanoparticles did not form / showed absence of the surface plasmon resonance. At constant concentration of cefaclor and varying concentrations of chloroauric acid showed the following results. (Figure 3.16)

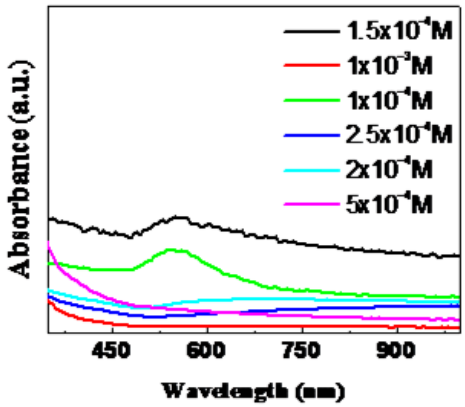

Figure 3.16. UV Visible spectrum of cefaclor reduced gold nanoparticles at cefaclor concentration of 1 x 10^{-5}M and varying concentration of gold nanoparticles, as shown in the graph.

The absorption spectrum of the gold nanostructures suspended in water (Figure 3.16) show a peak around 520 nm at low concentrations of chloroauric acid, due to the transverse plasmon band and an absorption increasing into the near-IR region; at higher concentrations of chloroauric acid, the longitudinal plasmon mode without indication of leveling off.[50] For further characterization of this interesting behavior at higher concentrations, TEM micrographs at these concentrations were obtained, which showed very unique results. (See Figure 3.17) It is important to note that the bluish-tinged nanoparticles formed at higher concentrations of chloroauric acid formed at slower growth rates and were not very stable for long; they soon settled down as black precipitates.

Upon observation of the TEM micrographs and noting the surface plasmon absorbance, it is well known that the position and intensity of the longitudinal band depend largely on the size and aspect ratio of gold nanocrystals.[47-49, 51] Notably, the SPR absorption due to the longitudinal plasmon band is not apparent, although an

absorption increase can be observed in the near-IR region. This result could be attributed to the poly-dispersity in the length, width, and thickness of the nanostructures.

The non-uniformity in the aspect ratio of these nanostructures could result in a longitudinal plasmon band with the position lying in a wide range of wavelengths, and the observed absorption spectrum may represent a contour combining the absorption spectra of gold nanoparticles with varied aspect ratios. The partial overlapping between the transverse band and the longitudinal band could also lead to the apparently weak intensity of the SPR bands, in the case of absence of sharply resolved transverse and longitudinal modes. Such structures as observed in our TEM micrographs have been observed previously from this lab,[52] wherein different unique structures are formed. Triangular nanoribbon-like structures are formed (Figure 3.17 M, N, P & Q). The dark bands observed in the structures of these micrographs are due to strains in the ribbons from buckling during growth. Anita Swami *et al.* observed the serrated gold nanoribbons formed at longer reaction times and attributed it to the template growth process rather than assembly of smaller subunits.[52] However, they have observed such structures at Langmuir monolayers, we report it in solution phase.

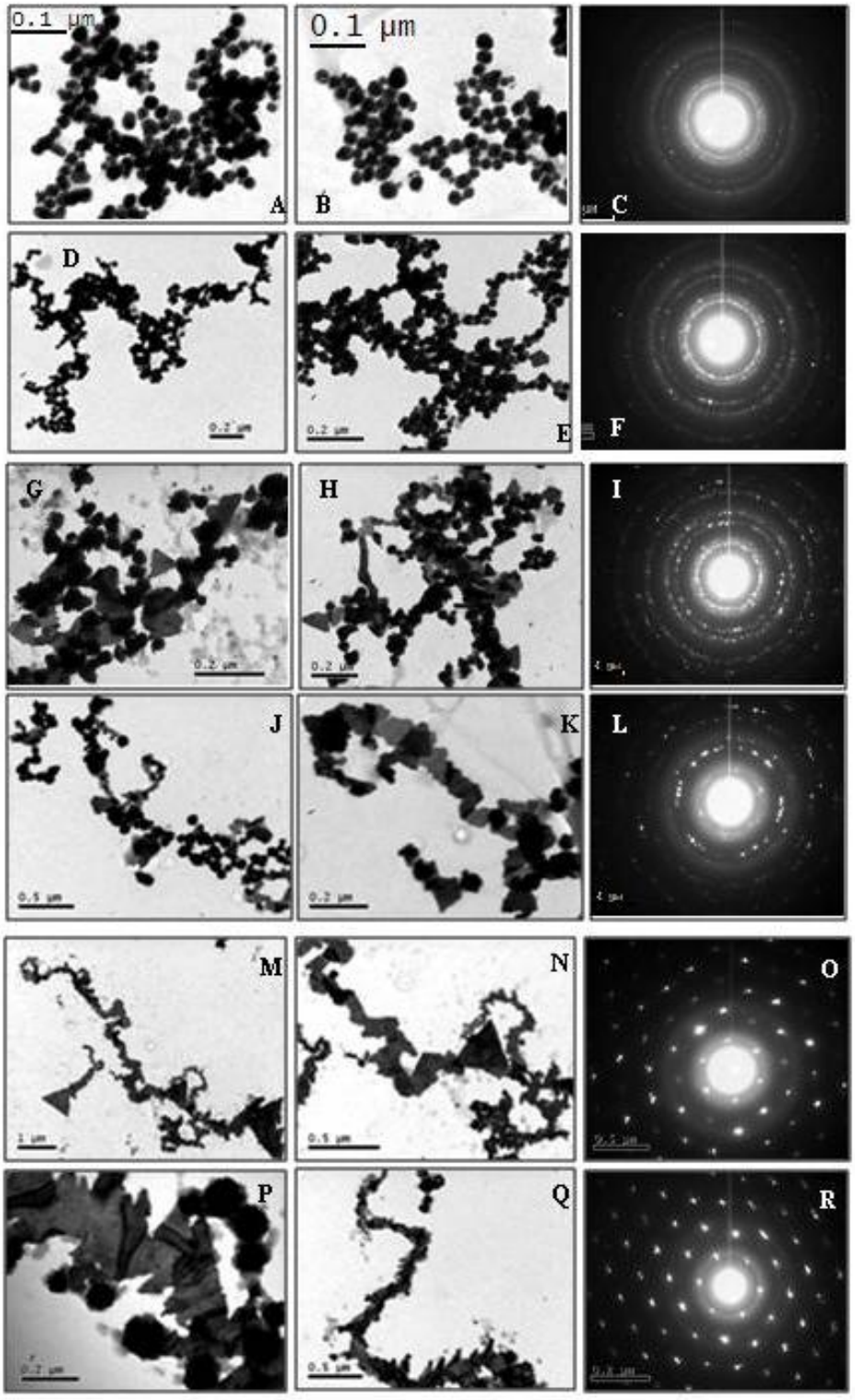

Figure 3.17. TEM micrographs and SAED pattern of cefaclor synthesized gold nanoparticles, at constant cefaclor concentration of 1 x 10^{-5}M. The varying chloroauric acid concentrations are **(A-C)**: 1 x 10^{-4}M, **(D-F)**: 1.5 x 10^{-4}M, **(G-I):** 2 x 10^{-4}M, **(J-K):** 2.5 x 10^{-4}M, **(M-O):** 3 x 10^{-4}M and **(P-R):** 4 x 10^{-4}M.

The XRD pattern shown in Figure 3.18 exhibits reflections characteristic of face-centered cubic (fcc) Au; The XRD pattern shows primarily the (111) Bragg reflection of fcc gold,[37] indicating a highly oriented growth in the presence of the antibiotic. The other reflections are weak and broader, relative to the (111). When the reduction rate is substantially slowed, structures such as Au nanoplates will be produced. When a mild reducing agent is used, kinetic control at room temperatures can be achieved.

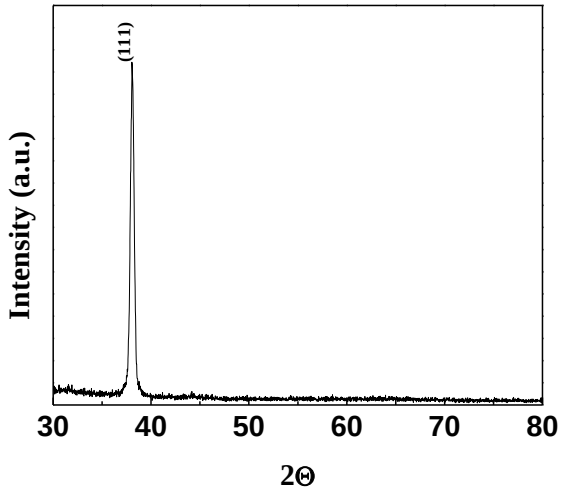

Figure 3.18. X-ray diffraction pattern of cefaclor (1 x 10^{-5}M) synthesized gold nanoparticles (4 x 10^{-4}M).

This kinetic control gives rise to nanoplates usually with hexagonal or triangular profiles. Since the concentration of Au ions is low enough to facilitate seeds, they cannot be thermodynamically controlled. Instead, the Au atoms appear to aggregate into small clusters, which then can agglomerate into larger nanocrystals.[53] As a result of this aggregate assembly, twin defects or stacking faults are introduced, which favor Au nanoplate formation. This explains the structures that we see in the TEM images. It is also known that if stacking faults are introduced, the plate-like seeds will be formed.[17] These seeds might also induce the self-assembly of structures that we observe in the TEM images. However, further detailed study using advanced experimental techniques is required for the mechanism of formation of such elongated Au poly-nanotriangles.

3.1.3. Synthesis of gold nanoparticles using ampicillin

Ampicillin (MW 339.79) ((2S, 5R, 6R)-6-([(2R)-2-amino-2-phenylacetyl]amino) -3,3-dimethyl-7-oxo-4-thia-1-azabicyclo[3.2.0]heptane-2- carboxylic acid) is a penicillin beta-lactam antibiotic used in the treatment of bacterial infections caused by susceptible, usually gram-positive organisms. The structure of ampicillin is shown in Figure 3.19. By binding to specific penicillin-binding proteins (PBPs) located inside the bacterial cell wall, ampicillin inhibits the third and last stage of bacterial cell wall synthesis. Cell lysis is then mediated by bacterial cell wall autolytic enzymes such as autolysins; it is possible that ampicillin interferes with an autolysin inhibitor. The structure of ampicillin is as shown below.

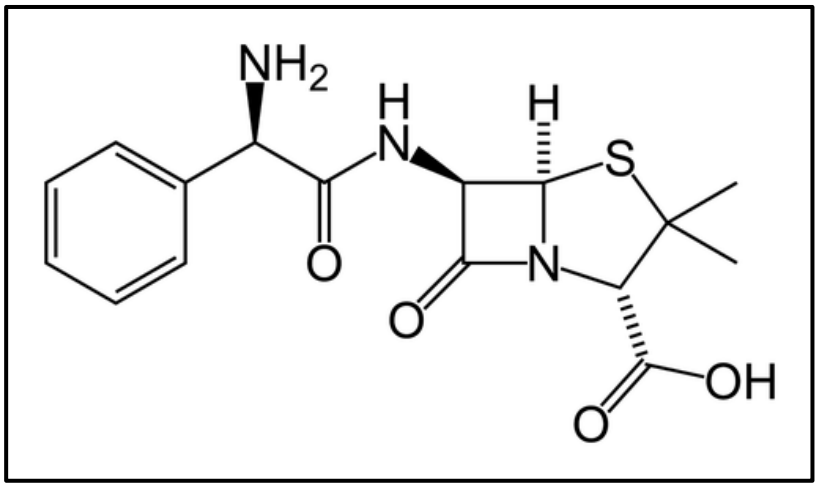

Figure 3.19. Structure of ampicillin

Similar to the synthesis of gold nanoparticles by cephalexin and cefaclor, ampicillin also forms gold nanoparticles. And akin to the bimodal distribution observed in the cephalexin synthesized gold nanoparticles, (see the following chapter), ampicillin also shows remarkable bimodal distribution.

3.1.3.1. Experimental details

The experimental details are as described in case of cephalexin, except the concentrations vary in each case, as mentioned.

3.1.3.2.Results and Discussions

The synthesis and surface plasmon resonance spectrum are similar as explained above. The TEM micrographs, clearly showing the bimodal distribution are depicted below. (Figure 3.20)

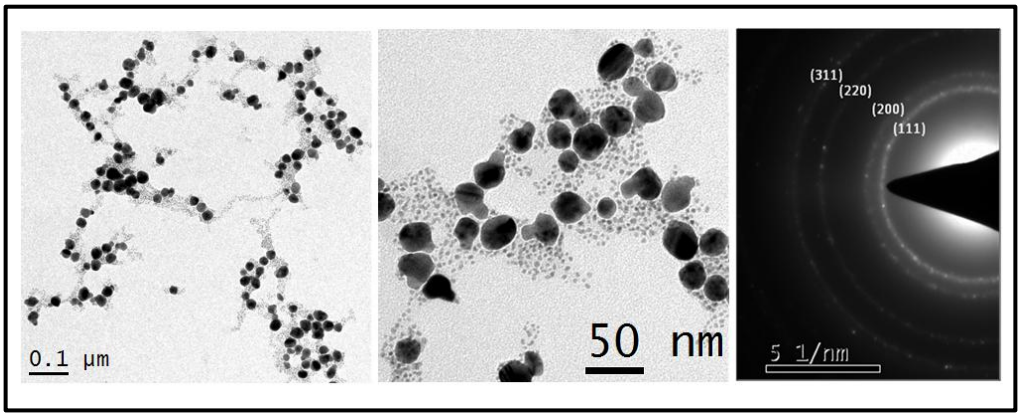

Figure 3.20. TEM micrographs of ampicillin (1 x 10^{-5} M) reduced gold nanoparticles (1 x 10^{-4} M).

To take a closer look at the smaller particles, if they are gold or unreacted/leached out antibiotic, HRTEM imaging of the nanoparticles are done. It is very clearly seen from the crystal planes, in Figure 3.21, that the background spotting is from small gold crystals and not any organic molecule. The lattice spacing matches with that of gold ~0.24 nm. The HRTEM image of the larger gold nanoparticle shown in Figure 3.22 also exhibits clear fringes with a spacing of ~ 0.24 nm, which agrees well with the spacing of Au crystal. Thus, we see, that ampicillin also produces stable gold nanoparticles, exhibiting bimodal distribution, which has further scope of study for understanding the process of nucleation and growth in facile systems.

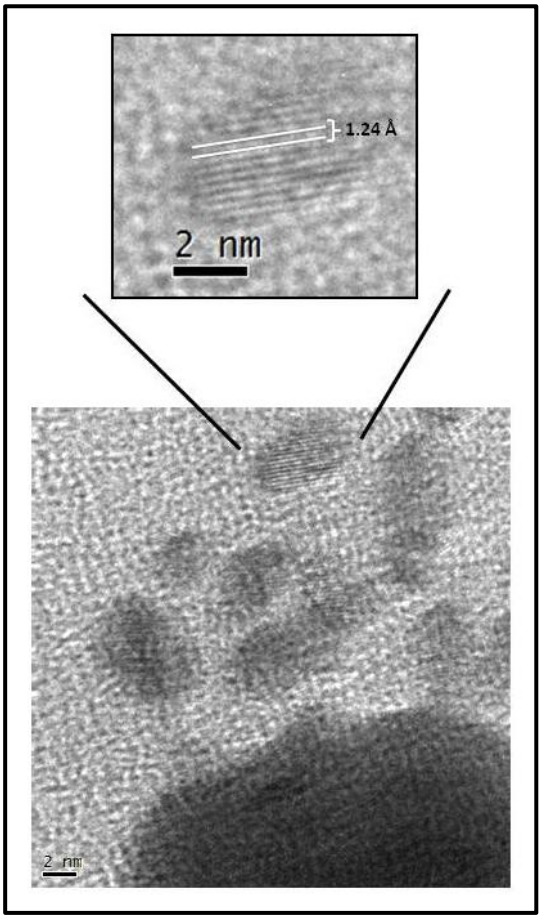

Figure 3.21. HRTEM of ampicillin reduced gold nanoparticles, taking a closer image of the smaller nanoparticles as shown above.

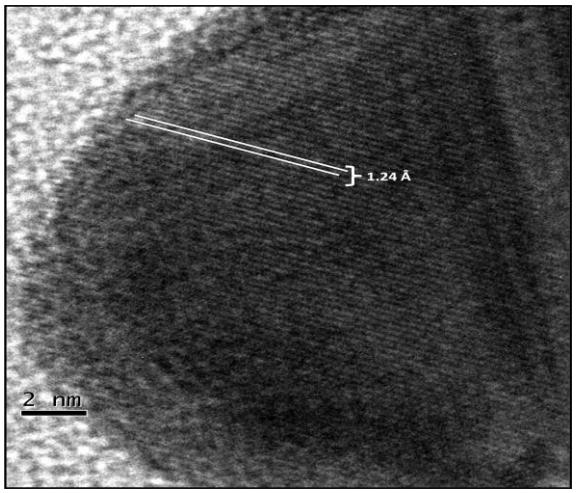

Figure 3.22. HRTEM of larger ampicillin reduced gold nanoparticles

3.1.4. Anti-bacterial activity of gold nanoparticles synthesized by antibiotics

Previous reports have expressed the need for capping the antibiotics to have effective enhancement in anti-bacterial activity.[54] The suggestion made is that a necessary condition for increase of antibacterial activity is the preparation of stable conjugates of NPs coated with the antibiotic molecules. In an effort to test the functionality of the antibiotics synthesized gold nanoparticles, different methods of anti-bacterial activity study were conducted.

We have reported the qualitative data, of testing the anti-bacterial activity of these samples, since the concentration window of the synthesis of gold nanoparticles by antibiotics is very narrow and thus accurate estimation of the capped bio-molecule was not error free. Moreover, since the antibiotic itself participated in the reaction to form gold nanoparticles, an exact quantitative control of the antibiotic is not possible; the capping agent now is an oxidized form of the antibiotic. Nonetheless, we observed good preliminary activity, which could be further used for combating issues such as multi-drug resistance and tagging desired molecule for targeted drug delivery.

The anti-bacterial test was done by pre-incubating the culture with the sample and then spread-plating an aliquot. Bore-plate method was not very effective owing to the reasons of Diffusional hindrance of Au NPs encountered in the agar medium. Due to which, the lack of activity could be a false negative data. Thus, spread-plate method proved useful in our study. The plates were incubated at 37 °C, overnight, after which the colonies were counted. The graphs depicting the growth curve, based on the colony count is shown below. Enumeration of colonies is plotted against the time taken for their growth.

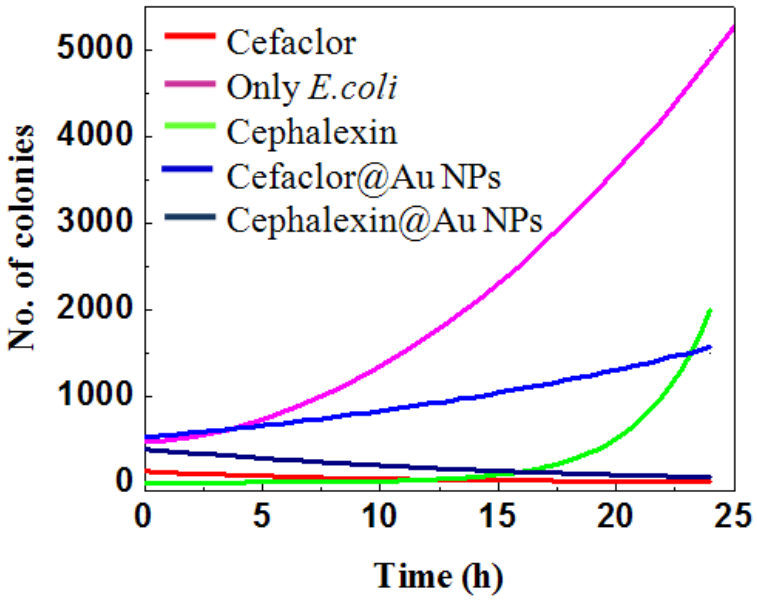

Figure 3.23. Growth curve of *E.coli* (NCIM no. 2931) culture

We see that though there is no complete inhibition of growth in either of the above two cultures, there is mild temporal anti-bacterial activity in cefaclor synthesized Au NPs and very good anti-bacterial activity in cephalexin synthesized Au NPs. However, in case of *Bacillus subtilis* (NCIM no. 2063) we observe converse results, as seen in the plates shown in Figure 3.25.

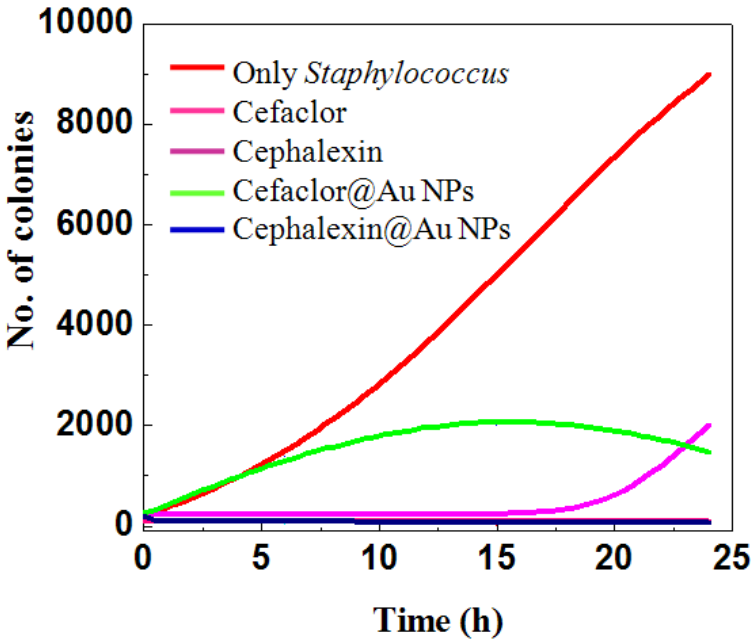

Figure 3.24. Growth curve of *Staphylococcus* (NCIM no. 2079) culture

It is interesting to note that in this case of Bacillus growth, there is complete inhibition of bacterial growth by cefaclor synthesized Au NPs. (See Figure 3.25D) However, it is very important to note that sodium borohydride reduced Au NPs (Figure 3.25B) also exhibit anti-bacterial activity. Though it is already proven that Au NPs themselves do not affect bacterial growth or functional activity,[55] this may be attributed to the unreduced Au ions still in sample, either due to electrostatic interactions or from steric-trapping within the capping agent. These present interesting results and further scope of future research work.

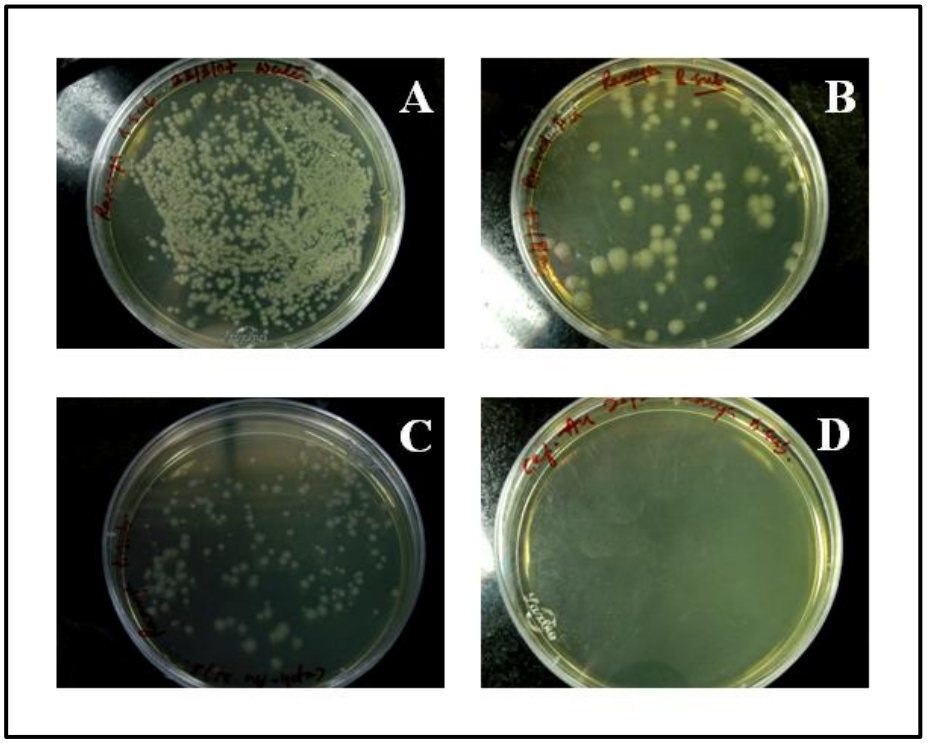

Figure 3.25. Anti-bacterial activity shown on spread plates of *B. subtilis* (NCIM no. 2063) culture. **(A)** Only culture, **(B)** Sodium borohydride reduced Au NPs, **(C)** Cephalexin synthesized Au NPs and **(D)** Cefaclor synthesized Au NPs.

3.1.5. Conclusions

Differently shaped gold nanoparticles have been produced in this simple synthesis using antibiotics. The capping agent, in this study, a by-product of the reaction of reduction of metal ions, is a very important moiety in the synthesis of nanoparticles. The use of a capping agent to dictate the shape of nanocrystals should be considered a thermodynamic means of controlling the shape as it makes some facets

thermodynamically more favorable by reducing their interfacial free energies through chemisorptions, where highly controlled morphologies are produced. Despite the importance of surface capping in controlling the shape of a nanocrystal, its explicit role(s) and mechanism(s) are poorly defined and a full understanding is still elusive. One technical barrier is the lack of experimental tools capable of resolving the molecular structure of a capping agent on a nanocrystal surface.[17] In this study we have used a few spectroscopic techniques to confirm the presence of the capping molecules (cephalexin) and analyse the spectrum that is obtained. However, resolving the configuration and packing of the molecules is not done. The sulfur moiety of the β-lactam ring is responsible for binding onto the Au NP, making the system stable.

In conclusion, we have reported for the first time, an *in situ* facile controlled synthesis of quasi-spherical and anisotropic gold nanoparticles at room temperature using cephalexin, cefaclor and ampicillin as the reducing agent as well as the capping agent separately in each case. The plate-like gold nanoparticles can be used for biomedical applications such as to slice through the cells after surface functionalisation with drugs or labeling the particles with various desired carrier biomolecules. Additionally, the infrared absorption of the anisotropic particles could be utilized for hyperthermia in various therapeutic treatments like for cancer[56, 57] and in architectural applications such as infrared-absorbing optical coatings.[58] This also offers a good system to evaluate the contribution of conformational entropy in the binding that is occurring in situ, as the nanoparticle is formed.

Additionally, it will also be quite interesting to investigate the size- and shape dependent cellular uptake and cytotoxic studies of the anisotropic gold nanostructures. Though the nanoparticles are stabilized, owing to reduction and binding by cephalexin, the potential self stability of cephalexin has to be established. The possible enhanced antimicrobial activity of oxidized antibiotic-bound nanoparticles is underway. This paves a new mode of delivering the antibiotics and combating the highly resistant bacteria. In all the cases, we have synthesized highly stable nanoparticles by cephalexin, cefaclor and ampicillin, which are well-dispersed over a couple of years and which offer a promising system for future research.

3.2. Functionalisation of iron oxide nanoparticles with Penicillin G acylase

Nanotechnology offers opportunities to interface with biology in new ways and with unprecedented precision. Considerable attention is given to nanoparticles made of magnetic materials. Magnetic nanoparticles are well-studied systems that offer:

i. controlled size,
ii. ability to be manipulated externally, and
iii. enhancement of contrast in magnetic resonance imaging (MRI)[59]

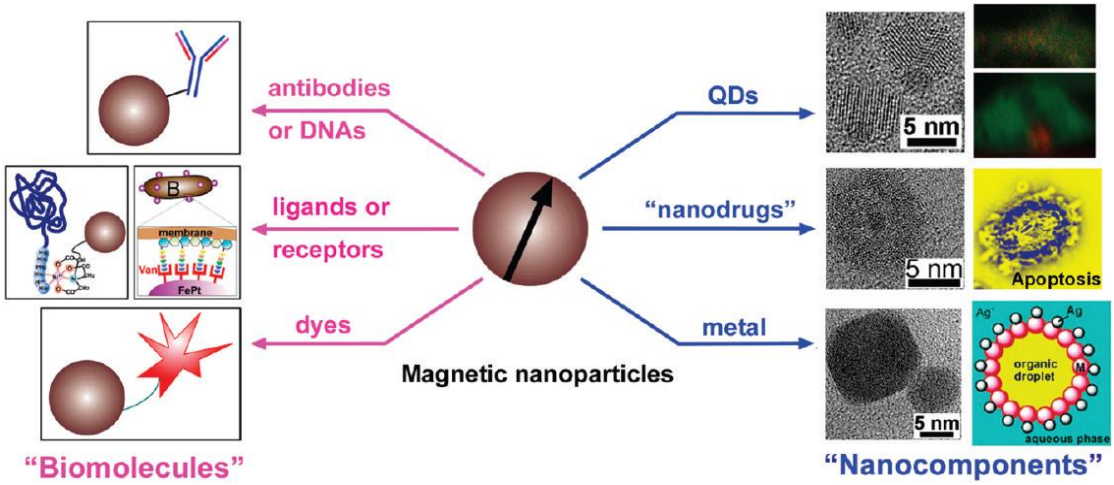

Figure 3.26. Schematic representation of facets of use of magnetic nanoparticles. [Adapted from ref[59]].

With the increasing demand for functional nanoparticles, that could act as nano-devices, nano-sensors, nano-carriers, etc in different thrusts of areas. The application of the nanostructures stems from two key materials: (1) the unique properties displayed by the core nano-material and (2) the capping molecule on the surface of the nanomaterials. As explained previously, the former aspect determines what property of the nanoparticle is required in the application. Here, in this study, we are making use of magnetic nanoparticles as the core nano-material. The use of magnetic nanoparticles has paved a plethora of specializations in biomedical and diagnostic applications such as cell-separation techniques, cell-labeling and targeting[60], magnetic resonance imaging[61], drug delivery, magnetofection, etc. Magnetic nanoprobes have the answer to the lacking technology to assess the molecular targets of biomolecules in living cells. Jaejoon Won *et al.* developed MAGIC (Magnetism-based interaction capture) that identifies targets in living cells on the basis of induced

movement of superparamagnetic nanoparticles.[10] The magnetic nanoparticles are abundantly used in biotechnological applications such as enzyme immobilsation[62], drug delivery [63], or separation techniques.[64] These are exploited enormously also due to their reported low toxicity and high biocompatibility.[63, 65] Also, the latter aspect of a proper capping molecule on the surface of the nanoparticle is more important from the functionality point of view; the molecules at the surface determine what the nanoparticle sees in the *nanocosm* and the macrocosm, and hitherto how it functions.

In this work, we suggest a general approach towards fabricating the surface of the magnetic nanoparticle to act as an immobilization substrate, so as to form a simple enzyme-substrate interaction and release the product. The objective, as shown in the schematic (Figure 3.27) was to study the activity of the enzyme capped on the magnetic nanoparticle in solution. The advantage of using magnetic nanoparticles is in the ease of separation after the reaction is over and washing is done. This idea of using magnetic nanoparticles for the separation of biomolecules and cells is already in the market; thus, if the enzyme activity in our system is not affected, it would prove to be very useful to immobilize the enzyme onto these nanoparticles.

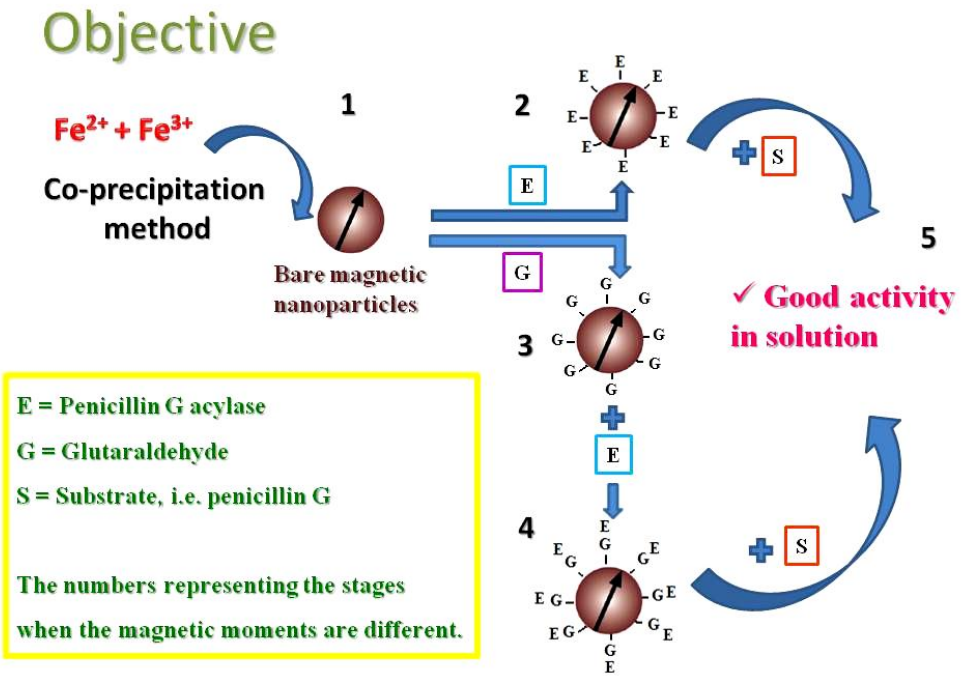

Figure 3.27. Schematic representation of the objective in this study. Step 1 is the synthesis of magnetic nanoparticles, step 2 and 3 comprises of capping the bare nanoparticles with enzyme and glutaraldehyde respectively, step 4 is immobilizing enzyme onto the glutaraldehyde capped nanoparticles and step 5 involves determining the activity of the enzyme conjugated to these nanoparticles.

3.2.1. Synthesis of iron oxide nanoparticles and capping by enzyme Penicillin G acylase

Certain nanomaterials are attractive probe candidates because of their

(1) small size (1-100 nm) and correspondingly large surface-to-volume ratio,

(2) chemically tailorable physical properties, which directly relate to size, composition and shape (Figure 3.26),

(3) unusual target binding properties and

(4) overall structural robustness.[66]

It also presents some fresh perspectives for designing nanoparticles for industrial applications. As-synthesized nanoparticles, typically produced by wet-chemical methods or physical vapour deposition, are in most cases disordered solid solutions with a face centred- cubic (fcc) structure. The iron oxide nanoparticles synthesized in this work are chemically synthesized. And the enzyme that is used in our study is

Penicillin G acylase. Penicillin acylases (Penicillin amidohydrolases, PAs, EC 3.5.1.11) are a subclass of the β-lactam antibiotic acylase superfamily. These enzymes hydrolyse the relatively stable amide bonds in penicillins producing the β-lactam nucleus, 6-aminopenicillanic acid (6-APA) and the corresponding side chain. It is estimated that more than 85% of 6-APA is obtained enzymatically from PGA activity (in the form of immobilized PGA) and the remaining from penicillin V acylase.[67] They are of great importance to the pharmaceutical industry for the production of semi-synthetic β-lactam antibiotics via the key intermediates 6-APA and 7-amino-3-deacetoxycephalosporanic acid (7-ADCA).[68, 69] Penicillin acylase with broad substrate specificity is exploited for the commercial production of semi synthetic penicillins as well as cephalosporins.[70] Because efficient recovery and reuse of the biocatalyst is a prerequisite for a viable process, much attention has been focused on the immobilization of penicillin G acylase. Thus we have chosen this enzyme as a model system to show possible activity upon immobilization onto nanoparticles.

Apart from mainly being used for the hydrolysis of natural β-lactams, penicillin acylases are also used for catalyzing the acylation of the amino group of key intermediates by appropriate esters or amides leading to the formation of semi-synthetic β-lactam antibiotics.[71] Penicillin G acylases are also useful for various other applications such as peptide synthesis[72, 73] removal of protecting groups[74, 75] and kinetic resolution of racemic mixtures.[72, 76]

In this work, the immobilized enzyme shows good activity, thus promising a potential system for industrial applications.

3.2.1.1. Experimental details

Synthesis of iron oxide nanoparticles

The iron oxide nanoparticles were formed by the popular co-precipitation method. The co-precipitation technique is probably the simplest and most efficient chemical pathway to obtain magnetic particles. Iron oxides (either Fe_3O_4 or γFe_2O_3) are usually prepared by an aging stoichiometric mixture of ferrous and ferric salts in aqueous medium. Ferric and ferrous salts were taken at a ratio of 2:1 (Fe^{3+}:Fe^{2+}) to have a total concentration of 10^{-2}M. The mixture was heated at 80 °C for 1 h with continuous stirring under non-oxidising environment.[77] Then, 5 mL of ammonium

hydroxide (30% w/w) was added rapidly and the mixture was vigorously stirred for another 1 h, after which it was cooled to room temperature. The precipitates were washed with hot water repeatedly for five times and separated by decantation before use. The considerably large numbers of nanoparticles are synthesized with good size-control.

Immobilization of penicillin G acylase

The Enzyme penicillin G acylase (PGA) used in this study was purified from the gram-positive bacteria *Arthrobacter viscosus* (ATCC 15294) in our lab. The enzyme was produced extracellularly in the culture broth. The cells were separated by centrifugation, and the clear broth was used for further purification by passing it through alumina column followed by hydrophoric interaction chromatography (octyl sepharose) and anion exchange chromatography (Q-sepharose). Purity of the enzyme was checked by native gel electrophoresis and was used as such for further studies.
The iron oxide particles were capped with glutaraldehyde (2%), by incubating at 4 ° C, on shaking for proper mixing. After incubation, excess glutaraldehyde was washed off using ample phospahate buffer (pH 8). Further, the iron oxide nanoparticles, with and without glutaraldehyde capping, were suspended in phosphaste buffer (pH 7.2) and varying concentrations of penicillin G acylase (3.32 IU/mL) was added. The mixtures were incubated a shaker at 4 °C for 1 h, after which excess enzyme was washed off using the same buffer. The immobilized penicllin G acylase nanoparticles were stored in the same phosphate buffer at 4 °C. The supernatant was assayed for unbound enzyme. The quantity of enzyme bound is the difference between the amount of enzyme added to the nanoparticle sol and the amount of enzyme remaining free in the supernatant. The immobilised penicllin G acylase nanoparticles were also processed for activity determination.

Enzyme activity test

The protocol for determination of PGA activity (both soluble and immobilized)[78] is as follows. The enzyme activity of Penicillin G acylase (PGA) was determined by measuring the amount of 6-APA produced in a 1 ml reaction mixture containing enzyme sample and 20 mg ml^{-1} Penicllin G (pen G) in 0.1 M phosphate buffer, pH 7.0, when incubated at 40 °C. [79] Penicillin G was obtained from KDL Biotech. The

reaction was stopped by adding 1 ml of citrate phosphate buffer (pH ~2.5). The 6-APA produced was estimated spectrophotometrically at 415 nm, after reaction with p-dimethylaminobenzaldehyde (PDAB), according to the protocol by Bomstein and Evans [80], modified by Shewale. [81] 0.1 g of PDAB was dissolved in 17 mL of methanol. One unit of PGA activity is defined as the amount of enzyme required to produce 1 μmole of 6-APA in one minute under the assay conditions (40 ^{o}C and pH 7.0).

Enzyme activity, expressed in international units (IU), is defined as the quantity of the enzyme required to liberate 1 μmol of 6-APA (which corresponds to an O.D. of 0.81) produced per minute under conditions of assay.

$$Activity = \frac{\Delta O.D.}{0.81} \times \frac{1}{t} \times D.F. \times \frac{1}{vol.of\ enzyme\ (mL)}$$

where, $\Delta O.D.$ is the different in the optical density of the sample and the background,

t is the time of incubation during the activity test, and

D.F. is the dilution factor while measuring the absorbance.

3.2.1.2. Results and Discussions

The iron oxide nanoparticles synthesized by co-precipitation method was index matched (JCPDS 190629) and shown in Figure 3.28. The morphology of these nanoparticles was obtained on TEM micrographs shown in Figure 3.29. The particles synthesized were roughly around ~ 20 nm in size.

After incubation with glutaraldehyde and the enzyme PGA, the samples were tested for activity against the substrate pen G, as explained in the experimental details section.

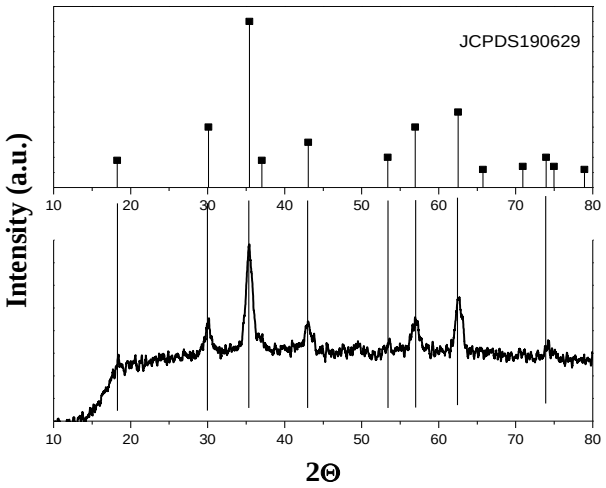

Figure 3.28. X-ray diffraction pattern of iron oxide nanoparticles synthesized by co-precipitation method.

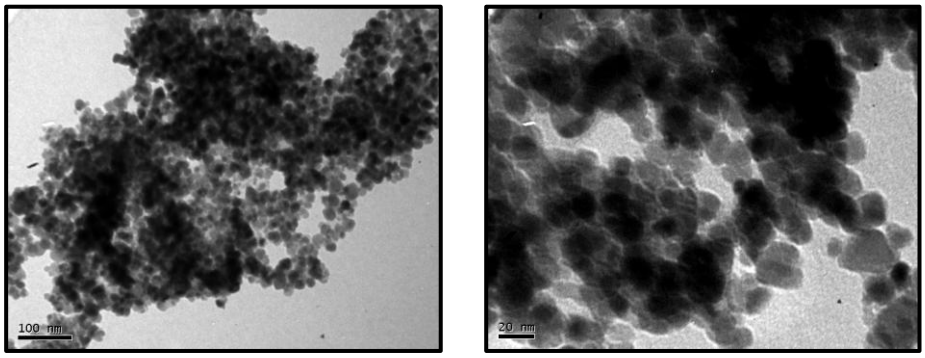

Figure 3.29. TEM micrographs of iron oxide nanoparticles.

The Figure 3.30 clearly shows that glutaraldehyde serves to be a good cross-linking agent, enabling better binding of the enzyme onto the nanoparticle surface than the enzyme bound directly onto the bare nanoparticle.

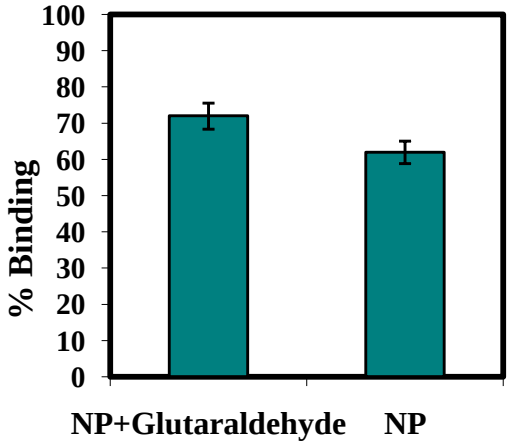

Figure 3.30. Comparision of binding percentage between enzyme immobilized on glutaraldehyde capped nanoparticles and bare nanoparticles.

Hence, for further estimation of enzymatic studies, we have taken the enzyme immobilized on the glutaraldehyde capped iron oxide nanoparticles. The AFM image is shown in Figure 3.31.

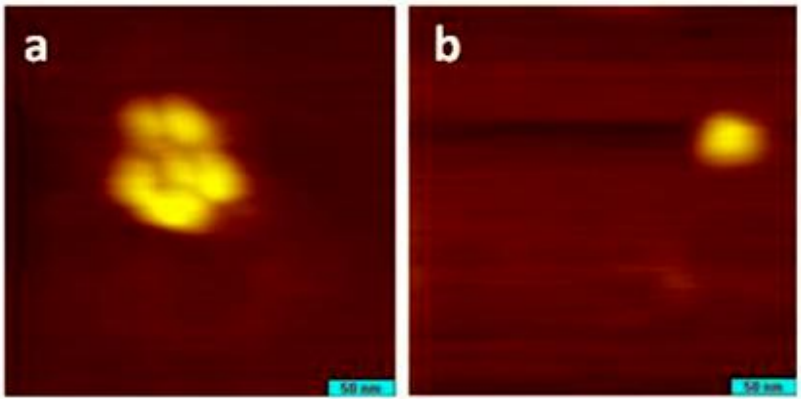

Figure 3.31. AFM contact-mode image of **(a)** unbound iron oxide nanoparticles and **(b)** enzyme bound glutaraldehyde capped iron oxide nanoparticles. A soft cantilever of spring constant = 0.2 N/m from budget sensor is used. The force set point was .03 nN.

The bare iron oxide nanoparticles are seen to be larger in size as compared to the TEM micrographs data. Clearly the lateral size of the nanoparticles imaged in AFM is large due to the convolution effect of the tip.[82] Nonetheless, a comparison of the unbound iron oxide nanoparticles and the enzyme bound glutaraldehyde capped nanoparticles exhibits a larger size in case of the latter due to the capping molecules on the nanoparticle surface. Thus the confirmation of capping from both activity

(which was clearly absent in case of bare nanoparticles and only glutaraldehyde capped nanoparticles) and imaging is seen in the above results.

Further, saturation kinetics was performed to determine the concentration at which the saturation of immobilization was taking place for a given amount of nanoparticles as shown in Figure 3.32.

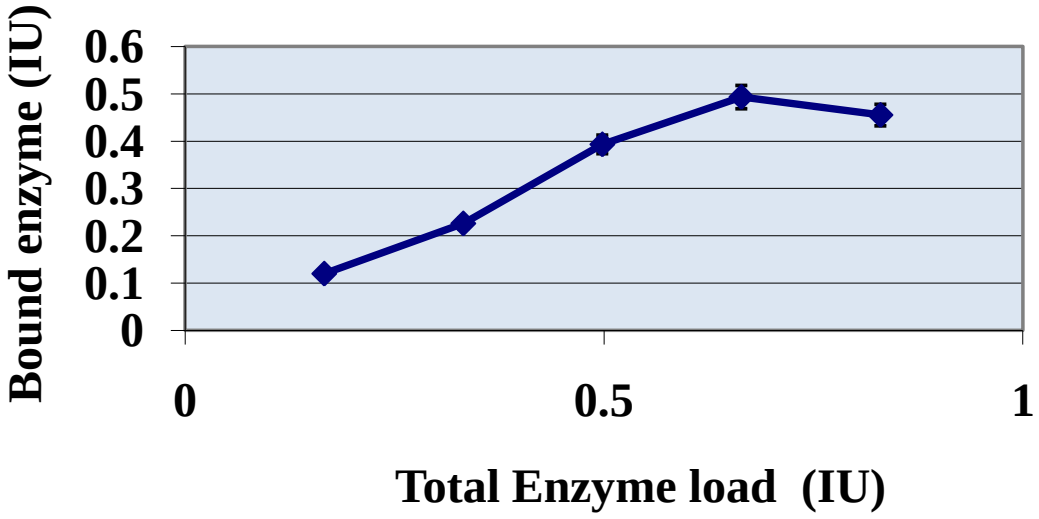

Figure 3.32. Saturation kinetics of PGA binding on nanoparticles.

We observe a linear increase in the binding initially; after a load of 0.5 IU of the enzyme, the plot reaches a plateau. Comparison of values for binding, immobilized enzymes (IME) activity, % expression and overall efficiency of the PGA onto glutaraldehyde capped iron oxide nanoparticles showed greater binding capacity. If the % expression values are remain same after separation and washing, this will be a potential candidate for use as a commercial carrier for immobilization of PGA.

For a given mass of nanoparticles, when incubated with different amounts of PGA (0.166 to 0.833 IU/mL), we note clear trends in enzyme binding, percent binding, and IME activity, and in the % expression as presented in Table 1. The amount of PGA bound increased from 0.120 to 0.455 IU/mL, while % binding decreased from 72 to 54%. Likewise, the activity of immobilized PGA preparation (IME activity) increased from 0.088 to 0.409 IU/mL but the % expression decreased progressively.

Table 1. Immobilisation of PGA onto nanoparticle: effect of enzyme loading on nanoparticles

Enzyme Loaded (IU/mL*)	Enzyme Bound (IU/mL*)	Binding %	IME activity (IU/mL*)	Expression %
0.166	0.120	72	0.088	73
0.332	0.226	68	0.176	78
0.498	0.393	78	0.316	80
0.664	0.493	74	0.408	82
0.830	0.455	54	0.409	90

(*1 mL contains 0.125mg of iron oxide nanoparticles); IME: Immobilized Enzyme activity

However, the decrease is not much and the error is minimal between the two percentages. The decrease in expression activity in the binding of PGA can be due to the following reasons:

i) Loss of activity due to leaching of bound enzyme

ii) Masking of the active site due to binding onto the nanoparticles

iii) Diffusional barriers for the substrate during activity

In addition to this, experimental errors, such as loss of nanoparticles bound with the enzyme during washes, are unavoidable and could be a major contributing factor in the difference of activity.

3.2.2. Conclusions

With great advantage of being able to immobilize the enzyme in its active state and efficiently form product upon reacting with the substrate at concentrations that is industrially accepted. Though further tests are needed to validate this process to the industrial level, this is a novel system where the applicability of the iron oxide nanoparticles for the immobilization and good activity has been demonstrated in the case of Penicillin G acylase. The present investigations confirm the hypothesis of the possibility of use of PGA immobilised onto glutaraldehyde capped iron oxide nanoparticles. The binding of PGA on the glutaraldehyde capped nanoparticle is due to the stable interaction of the enzyme with glutaraldehyde and this is governed by

its surface properties. Studies are underway for ascertaining the re-usuability upon magnetic separation and repeated washing, and possible leaching with time.

Further refinement of the functionalisation and magnetic studies could also prove this system to be a useful biosensor. Magnetic nanoparticles have already been tested for acting as biosensors and many uses are there in the market. Superparamagnetic nanoparticles (MNPs) are biocompatible,[63] making it safe from the environmental pollution point of view. Introducing these nanoparticles, as possible industrial application shown in our study, does not pose a threat to our environment.

3.3. References

1. Barth, J.V., *et al.* (2005) *Nature* 437, 671
2. Howarth, M., *et al.* (2005) *Proc. Natl. Acad. Sci. U.S.A.* 102, 7583
3. Park, S.A., *et al.* (2002) *Science* 295, 1503
4. Bruchez, M., *et al.* (1998) *Science* 281, 2013
5. Liu, T., *et al.* (2005) *J. Fluoresc.* 15, 729
6. Michalet, X., *et al.* (2005) *Science* 307, 538
7. Gupta, A.K., and Gupta, M. (2005) *Biomaterials* 26, 3995
8. Yoon, T.J., *et al.* (2005) *Angew. Chem., Int. Ed.* 44, 1068
9. Alexiou, C., *et al.* (2005) *J. Magn. Magn. Mater.* 293, 389
10. Won, J., *et al.* (2005) *Science* 309, 121
11. Pankhurst, Q.A., *et al.* (2003) *J. Phys. D: Appl. Phys.* 36, R167
12. Anacona, J.R., and Rodriguez, I. (2004) *J. Coord. Chem.* 57, 1263
13. Kim, J.S., *et al.* (2007) *Nanomedicine* 3, 95
14. Gu, H., *et al.* (2003) *Nano Lett.* 3, 1261
15. Rosemary, M.J., *et al.* (2006) *Langmuir* 22, 10125
16. Murray, C.B., *et al.* (1993) *J. Am. Chem. Soc.* 115, 8706
17. Xia, Y., *et al.* (2009) *Angewandte Chemie-International Edition* 48, 60
18. Spratt, B.G. (1975) *Proc. Natl. Acad. Sci. U.S.A.* 72, 2999
19. Babic, M., *et al.* (2006) *Drug Resist. Updates* 9, 142
20. Bryskier, A. (2002) *Clinical Microbiology and Infection* 8, 467
21. Shukla, R., *et al.* (2005) *Langmuir* 21, 10644
22. Mandal, S., *et al.* (2002) *Proc. Indian Acad. Sci., Chem. Sci.* 114, 513
23. Niemeyer, C.M. (2001) *Angew. Chem., Int. Ed.* 40, 4128
24. Gole, A., *et al.* (2001) *Langmuir.* 17, 1674
25. Alivisatos, A.P., *et al.* (1996) *Nature* 382, 609
26. Kanaras, A.G., *et al.* (2003) *Angew. Chem., Int. Ed.* 42, 191
27. Torres Sanchez, R.M., *et al.* (1997) *Journal of Catalysis* 168, 125
28. Hashmi, A.S.K., and Graham, J.H. (2006) Gold Catalysis *Angewandte Chemie International Edition* 45, 7896
29. Zhao, N., *et al.* (2008) *Langmuir* 24, 991
30. Franklin, K., *et al.* (2004) Platonic Gold Nanocrystals *Angewandte Chemie International Edition* 43, 3673

31. Huang, C.J., *et al.* (2006) *Journal of the Electrochemical Society* 153, D129
32. Connor, E.E., *et al.* (2005) *Small* 1, 325
33. Burda, A., *et al.* (2005) *Chem. Rev.* 105, 1025
34. Lee, S., *et al.* (2003) *Adv. Mater.* 15, 441
35. Lanska, B. (1997) *Angew. Makromol. Chem.* 252, 139
36. Newman, J.D.S., and Blanchard, G.J. (2006) *Langmuir* 22, 5882
37. Leff, D.V., *et al.* (1996) *Langmuir* 12, 4723
38. Kumar, A., *et al.* (2003) *Langmuir* 19, 6277
39. Selvakannan, P.R., *et al.* (2004) *J. Colloid Interface Sci.* 269, 97
40. Aslam, M., *et al.* (2004) *J. Mater. Chem.* 14, 1795
41. Brust, M., *et al.* (1994) *J. Chem. Soc., Chem. Commun.*, 801
42. Weisbecker, C.S., *et al.* (1996) *Langmuir* 12, 3763
43. Brust, M., *et al.* (1995) *J. Chem. Soc., Chem. Commun.*, 1655
44. Wulff, G. (1901) *Zeitschrift Fur Krystallographie Und Mineralogie* 34, 449
45. Murphy, C.J., and Jana, N.R. (2002) *Adv. Mat.* 14, 80
46. Gao, J.X., *et al.* (2003) *Langmuir* 19, 9065
47. Murphy, C.J., *et al.* (2005) *J. Phys. Chem. B* 109, 13857
48. Murphy, C.J., *et al.* (2006) *Inorg. Chem.* 45, 7544
49. Chen, J.Y., *et al.* (2007) *Langmuir* 23, 4120
50. Zhang, X.J., *et al.* (2006) *Angewandte Chemie-International Edition* 45, 3112
51. Wiley, B., *et al.* (2005) *Mrs Bulletin* 30, 356-
52. Swami, A., *et al.* (2002) *Chem. Mat.* 15, 17
53. Besson, C., *et al.* (2005) *J. Am. Chem. Soc.* 127, 8179
54. Burygin, G., *et al.* (2009) *Nanoscale Res. Lett.* 4, 794
55. Williams, D., *et al.* (2006) *J. Nanobiotechno.* 4, 3
56. Loo, C., *et al.* (2004) *Technol. Cancer Res. Treat.* 3, 30
57. Hirsch, L.R., *et al.* (2003) *Proc. Natl. Acad. Sci. U.S.A.* 100, 135491
58. Shankar, S.S., *et al.* (2005) *Chem. Mater.* 17, 566
59. Gao, J.H., *et al.* (2009) *Acc. Chem. Res.* 42, 1097
60. Ben-David Makhluf, S., *et al.* (2006) *Langmuir* 22, 9480
61. Chun, A.L. (2009) *Nat Nano* 4, 698
62. Valdeì□s-Soliì□s, T., *et al.* (2009) *Chem. Mat.* 21, 1806
63. Jain, T.K., *et al.* (2008) *Mol. Pharmaceu.* 5, 316

64. SchÃ¶nfeldt, V.v., *et al.* (1999) *Biol. Reproduc.* 61, 582

65. Marchal, G., *et al.* (1989) *American Journal of Roentgen* 152, 771

66. Rosi, N.L., and Mirkin, C.A. (2005) *Chem. Rev.* 105, 1547

67. Vandamme, E.J. (1988) *Immobilized biocatalysts and antibiotic production: biochemical, genetical and biotechnical aspects.* Elsevier

68. Parmar, A., *et al.* (2000) *Biotech. Adv.* 18, 289

69. Sudhakaran, V.K., *et al.* (1992) *Proc. Biochem.* 27, 131

70. Shewale, J.G., and Sivaraman, H. (1989) *Proc. Biochem.* 24, 146

71. Hernandez-Justiz, O., *et al.* (1999) *Enzyme and Microbial Technology* 25, 336

72. van Langen, L.M., *et al.* (2000) *Tetrahedron-Asymmetry* 11, 1077

73. van Langen, L.M., *et al.* (2000) *Tetrahedron: Asymmetry* 11, 4593

74. Alvaro, G., *et al.* (2000) *Biocat. Biotransform.* 18, 253

75. Waldmann, H., *et al.* (1996) *Tetrahedron Lett.* 37, 8725

76. Fadnavis, N.W., *et al.* (1999) *Tetrahedron-Asymmetry* 10, 3675

77. Jolivet, J.P., *et al.* (2004) *Chem. Comm.*, 481

78. Bahulekar, R.V., *et al.* (1993) *Polymer* 34, 163

79. Balasing.K, *et al.* (1972) *Biochimica Et Biophysica Acta* 276, 250

80. Bomstein, J., and Evans, W.G. (1965) *Analytical Chemistry* 37, 576

81. Shewale, J.G., *et al.* (1987) *Biotechnology Techniques* 1, 69

82. Ebenstein, Y., *et al.* (2002) *Nano Letters* 2, 945

NUCLEATION AND GROWTH OF GOLD NANOPARTICLES

Chapter 4

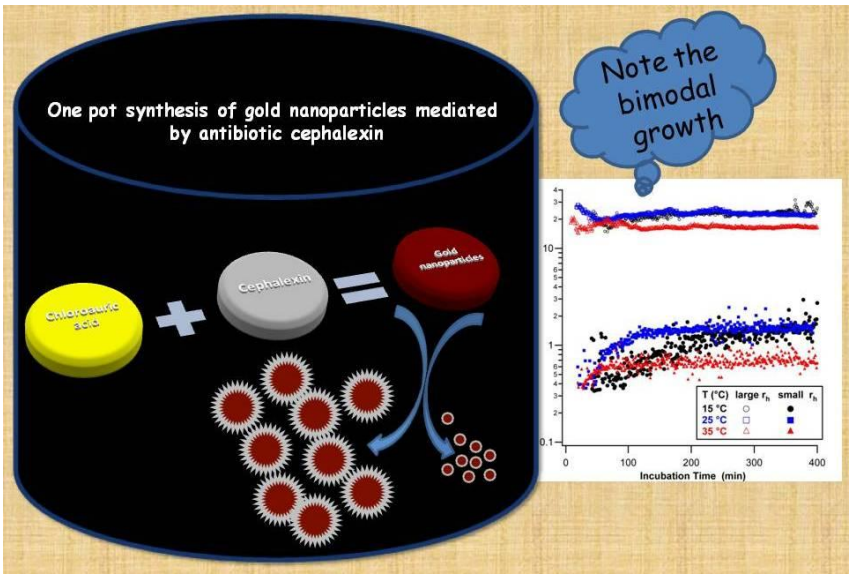

The unusual nucleation and growth kinetics of gold nanoparticles synthesized in the presence of the antibiotic cephalexin using *in situ* static and dynamic light scattering in conjunction with *in situ* UV-vis absorption measurements and transmission electron microscopy is reported in this chapter. Following a brief latency period, two well-separated populations of gold nanoparticles, with average sizes of 1-2 nm versus several tens of nanometer, respectively, nucleate simultaneously. For either size regime, the total number of particles increased rapidly, while their mean size and relative frequency remained essentially constant over a growth period of 5 h. With increasing temperature, the morphology of the larger nanoparticles became increasingly spherical, as indicated by the noticeable blue shift of the plasmon frequency for these particles. The detailed morphology for either particle population was confirmed with TEM. This is the first observation of simultaneous growth of two distinct populations of crystalline nanoparticles in the solution phase. The coupled growth of two distinct populations of nuclei, their tight control of size but rapid increase in overall numbers present novel and intriguing facets of this antibiotic-mediated solution-growth of gold nanoparticles. The size evolution of the Mie-frequency exhibits a noticeable blue shift as the temperature increases, correlating with the roundness of the particle/bimodal distribution.

Part of the work presented in this chapter has been published:

1. **Ramya Jagannathan**, Avanish Singh Parmar, Suguna Adyanthaya, Asmita Prabhune, Martin Muschol, and Pankaj Poddar, "In Situ Observation of Antibiotic Mediated Concurrent Growth of Two Distinct Homogeneous Populations of Gold Nanoparticles in Solution Phase"*J. Phys. Chem. C*, **2009**, 113 (9), 3478-3486.

4.1.Introduction

The properties of colloidal gold, silver and other such similar metals have been of interest for centuries with an extensive scientific research going back to Michael Faraday in 1857 on the colloidal gold samples.[1] In 1908, Mie presented a solution to Maxwell's equations that describes the extinction (absorption and scattering) of spherical particles of arbitrary sizes.[2] The exact theory of light scattering based on Mie theory is very complicated and limited to a small number of particle shapes. The calculated extinction, scattering and absorption spectra of a particle of size, d = 16 nm, are shown in Figure 4.1(a, b & c respectively). [3] In this chapter, the scattering and the absorption of gold nanoparticles are studied.

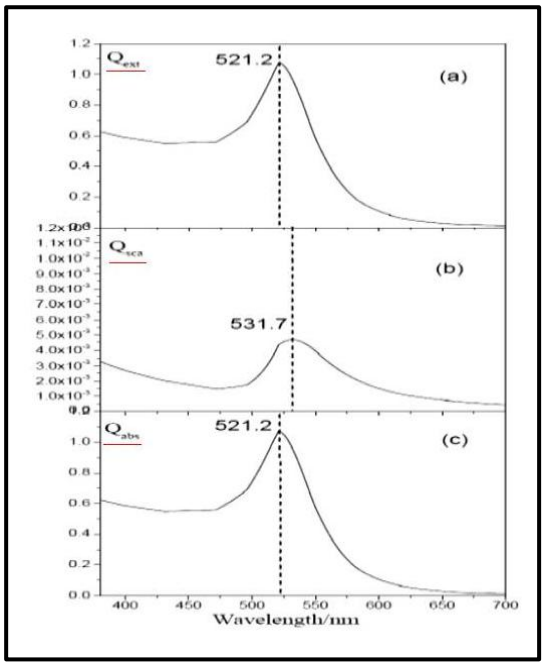

Figure 4.1. Calculated extinction, scattering and absorption spectra of a particle of size, d = 16 nm. Adapted from ref [3].

Ever since the Mie theory, there have been various models and approximations to study nanoparticles systems.[4, 5] Over the years, it has been realized that the morphology and the growth-rate of these nanostructures in the solution phase can be controlled and designed by tuning the reaction parameters. The wet chemical synthesis of nanomaterials has advanced to the level where it is possible to tailor make particle shapes, sizes, and their distributions. Different parameters and factors

affecting the process are varied to achieve a tight particle size control.[6, 7] However, to achieve control over the synthesis, it is important to understand the process of nucleation and growth of crystallites from the cluster level upward. This includes the specific roles played by various physical and chemical parameters such as temperature, concentration, pH, stirring, osmotic potential, incubation time, and so on. The mechanisms involved in the growth of nanoparticles follow different rules than those applicable to bulk materials. Over the last several decades, the mechanism of nucleation and growth processes of colloidal particles synthesized by various methods has been researched in detail. The initial swell in the nucleation and growth studies began predominantly with condensation[8, 9] and crystallization[10, 11] studies during the early twentieth century. However, mechanistic studies of colloid and cluster formation began when LaMer and Dinegar synthesized sulfur hydrosols nucleating from supersaturated solutions.[12] Uniform particle size was achieved by short nucleation and relatively long growth periods. Studies on kinetics and mechanisms of particle formation showed incompatibility with Lamer's supersaturation theory.[13, 14] Models and statistical theories began to be developed for understanding the formation of the critical nucleus and spontaneous growth which gives rises to particular sizes.[15, 16] Overbeek did extensive studies on the particle growth rate and the particle size distribution citing the possible rate-determining steps.[17] Analysis of the activation barrier in the nucleation process, studies on the parameters relevant for kinetic or thermodynamic control and factors controlling the growth process have improved our understanding of the overall process. However, the process of growth is quite complicated and difficult to study experimentally. It depends on numerous factors like:

- nucleation rates,
- cluster mobility,
- maximum cluster density,
- spatial and size distribution of clusters and
- modes of growth.

To fully understand the formation of particles at various levels, it is essential to capture and investigate the early stages of nucleation of the nanoparticles, their growth kinetics and the effect of various parameters. The chemistry and physics of gold nanoparticles has emerged as a broad new sub-discipline in the domain of

colloids. Specifically, the unique optical properties of gold nanoparticles have made this model system more useful in exploring a wide range phenomenon. This chapter describes the study undertaken during the initial stages of the reaction of chloroauric acid and cephalexin to form gold nanoparticles, the synthesis procedure and characterization of which is described in the previous chapter (Chapter 3).

Among the experimental techniques used to study and understand the kinetic and thermodynamic nature of the nanocrystal nucleation and growth, in general, are small angle X-ray scattering (SAXS),[18] UV-visible spectroscopy, X-ray photoelectron absorption spectroscopy (XPS),[19] time-dependent transmission electron microscopy (TEM),[20] and dynamic light scattering (DLS).[21] Though these techniques are highly efficient for the *in situ* measurements of particle size and shape determination, there are few problems, such as:

i. All methods obtain information about larger clusters (around >1-2 nm).
ii. The limitation on the time scale of the measurements; since nucleation and growth of the nanoparticles during laboratory syntheses proceeds quite fast.
iii. The nucleation events, in particular, are difficult to resolve since they represent a transient, meta-stable state.
iv. Complications due to the reaction setup (multistep synthesis processes, high temperature/pressure, etc.) prevent combination of light scattering with X-ray scattering for simultaneous *in situ* measurements.

Therefore, a careful investigation of nucleation and growth of nanocrystallites in the solution phase demands the synthesis process that is (1) single-step, (2) can be coupled with standard light/X-ray scattering set-ups, and is (3) slow enough reaction rate to capture the growth process.

The synthesis of gold nanoparticles using a biomolecules, such as cephalexin proved to be a suitable system for such a study due to the following reasons:

i. reaction ends over a large period (approximately 1.5 h at 28 °C),
ii. establishes the mechanism of metal synthesis by a biomolecule, specifically an antibiotic,
iii. scattering and absorption studies done using a simple system with no auxiliary chemicals or processes needed and
iv. no interference in the DLS study from micelle formation as happens in the reverse micelle-based methods.

This chapter discusses the results on the *in situ* light scattering and UV-vis measurements in combination with the transmission electron microscopy at various controlled temperatures to understand the growth mechanism. The *in situ* observation of antibiotic mediated concurrent growth of two distinct homogeneous populations of gold nanoparticles in solution phase is reported.

4.1.1. DLS theory

There are two basic methods of Light Scattering: Static Light Scattering (SLS) and Dynamic Light Scattering (DLS). "Classical" light scattering (also known as "static" or "Rayleigh" scattering [22, 23]) provides a direct measure of molecular mass. SLS is a powerful technique to estimate sizes, average molar masses of various single or assembled structures and their interaction with environment. SLS can be use to study various systems like colloids, synthetic and natural polymers in solution, including proteins and polysaccharides and to investigate oligomerization, complex formation, aggregation, stability, conformation and 2nd virial coefficient. [21]

Leon Brillouin was the first one to describe a short theoretical note describing the frequency distribution of the light scattered from thermally excited density fluctuations in an isotropic body. [24, 25] When an electromagnetic radiation is incident upon a molecule, the molecule constitutes an oscillating dipole or electric oscillator depending upon the effect of the magnitude of the polarizability of the molecule, i.e. the ease of shifting charges within the molecule. In an elastic scattering, the oscillating dipole acts as an emitter of an electromagnetic wave of the same wavelength as the incident wavelength, emitting isotropically in all directions perpendicular to the oscillator. Now, for molecules or particles larger than 20 nm, most of the oscillating dipoles created within one given particle possess a significant phase difference. Accordingly, interference of the scattered light emitted from such an individual particle of size larger than 20 nm leads to a non-isotropic angular dependence of the scattered light intensity. The interference pattern of intra-particular scattered light, also called particle form factor, is characteristic for size and shape of the scattering particle. As a consequence, it provides the quantitative means for the characterization of particles in very dilute solution by light scattering. For particles smaller than $\lambda/20$, only a negligible phase difference exists between light emitted from the various scattering centers within the given particle (See Figure

4.2A & 4.2B). Particles in solution, however, usually show a random motion (Brownian motion) caused by thermal density fluctuations of the solvent. As a consequence of the temporal changes in inter-particle positions and the corresponding temporal concentration fluctuations, the interference pattern and the resulting scattered intensity detected at a given scattering angle also change with time, reflecting the Brownian motion of the scattering particles[26] (See Figure 4.2C & 4.2D).

This phenomenon provides the basis for dynamic light scattering, an experimental procedure which yields a quantitative measure for the mobility of scattering particles in solution as characterized by their self diffusion coefficient. Most modern particle sizers, frequently used both in industry and academia nowadays to determine the (hydrodynamic) size of particles in solution, are based on this principle. The theory behind this principle is explained in the following section with reference to the system used in this study.

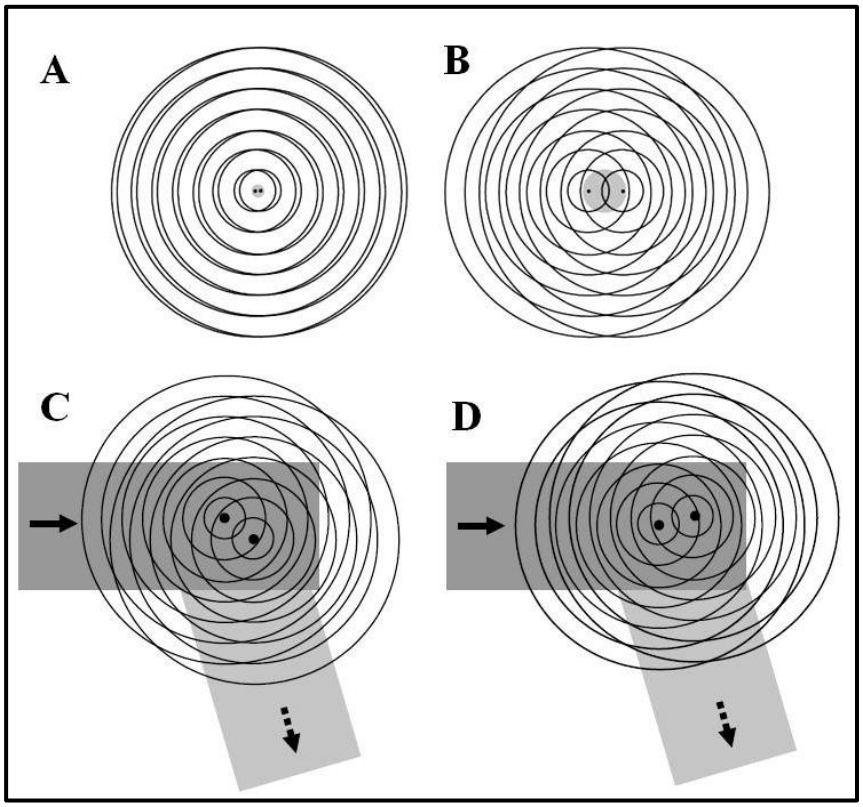

Figure 4.2. Interference pattern of light scattered from two scattering centers of small particles (**A**) and from larger particles (**B**). (**C**) & (**D**) shows the change in the interference pattern of

scattered intensity with time, caused by Brownian motion of two scattering particles. [Figure adapted from ref [26]]

The size distribution of the gold colloids scattering light and diffusing through the solution is related to the field correlation function g1(τ) of scattered light [27-29] via

$$g_1(\tau) = \int_0^\infty F(\Gamma)\exp(-\Gamma\tau)d\Gamma \quad \ldots\ldots (1)$$

indicating that the field correlation function is a linear superposition of exponential decays with decay rate Γ and relative amplitude F (Γ). [28, 29]

The field correlation function $g_1(\tau)$, in turn, is obtained from the experimentally measured intensity correlation function via the Siegert relation [28, 29]

$$g_2(\tau) = |g_1(\tau)^2| + 1 \quad \ldots\ldots (2)$$

Equations 1 and 2 are used to obtain the distribution of decay rates F (Γ) from the measured correlations of the light intensity fluctuations. The decay rates Γ themselves are related to the diffusion constants D of the diffusing particles via

$$\Gamma = Dq^2 \quad \ldots\ldots (3)$$

where, D is the diffusion constant of the scattering particle and

q is the magnitude of the scattering vector given by

$$q = (4\pi n/\lambda)\sin(\Theta/2) \quad \ldots\ldots (4)$$

where λ is the wavelength of the incident light,

n is the refractive index of the medium and

Θ is the angle at which the scattered light is detected with respect to the direction of the incident radiation.

For this system, parameters are n = 1.33 (aqueous solutions), and q = 2.64 nm^{-1}. Hence, particles with hydrodynamic radii r_h close to or below $q^{-1} \approx 38$ nm could be treated simply as isotropic Rayleigh scatterers. Finally, the distribution of diffusion coefficients can be converted into particle size distributions using the Stokes-Einstein relation

$$D = (k_B T)/6\pi\eta r_h \quad \ldots\ldots (5)$$

where k_B is the Boltzmann factor,

T is the absolute solution temperature,

η the temperature-dependent solution viscosity and

r_h is the hydrodynamic radius of the diffusing particle species.

During the nucleation studies, the amplitude of the autocorrelation functions steadily increased as nucleation and aggregation of the gold sol progressed. Correlation

functions with intercepts at $t \rightarrow 0$ smaller than 0.2 were excluded from our analysis due to their intrinsic noisiness. Otherwise, correlation functions were converted into particle size distributions using the "general purpose" inversion algorithm provided with the Zetasizer Nano S software. Particle size distribution obtained from alternative inversion algorithms yielded comparable results. There are few options for performing accurate and repeatable particle size analysis on materials in the nanoparticle range. DLS provides several advantages over electron microscopy since many more particles are actually analyzed, which provides improved precision and ability to detect small numbers of larger particles. Improvements in detector technology have led to detections of very small particles (measurements have been made up to 1 nm), particles that scatter low amounts of light and low concentrations of particles.

4.1.2. Surface Plasmon Resonance

The appearance of the ruby color in the tinted glass is explained due to the finally divided gold[1] and later on theoretically explained by Mie[2]. With this pioneering work he could trace the origin of the colours back to a resonant absorption of light by small metal spheres. The interaction of metals with the electromagnetic radiation is largely dictated by the free conduction electrons in the metal, also known as the Drude metal. This resonant absorption, which is caused by a collective excitation of the conduction band electrons in metal nanoparticles, is called *localized surface plasmon polariton resonance* (LSPPR).

According to the simple Drude model, the free electrons oscillate 180° out of phase relative to the driving electric field.

$$m_e \frac{\partial^2 \boldsymbol{r}}{\partial t^2} + m_e \Gamma \frac{\partial \boldsymbol{r}}{\partial t} = e\mathrm{E}_0 \mathrm{e}^{-\mathrm{i}\omega \mathrm{t}} \quad \ldots\ldots\ldots\ldots\ldots\ldots (6)$$

where e and m_e are the charge and the effective mass of the free electrons and

E_0 and ω are the amplitude and frequency of the applied electric field.

Due to this, most metals possess a negative dielectric constant at optical frequencies which causes, for example, a very high reflectivity. At optical frequencies, the metal's free electron gas sustains surface and volume change density oscillations called as plasma polaritons or plasmons with distinct resonance frequencies.

By definition, surface plasmons are the quanta of surface charge-density oscillations. The term "surface" stems from the fact that although all electrons are oscillating with respect to the positive-ion background, the main effect producing the restoring force is the surface polarization. The surface, thus, plays a very important role for the observation of surface plasmon resonance because it alters the boundary condition for the polarizability of the metal and therefore, shifts the resonance to optical frequencies, contributing to the beautiful color of gold nanoparticles.

The total extinction coefficient of nanoparticles is given in Mie's theory as the summation over all electric and magnetic multipole oscillations contributing to the absorption and scattering of the interacting electromagnetic radiation. The existence of plasmon is characteristics of the interaction of metal nanostructures with light. At the interface between a metal and a dielectric, the surface charge density oscillations give rise to strongly enhanced optical near-fields which are spatially confined near the metal surface. The localization at the interface is characterized by electromagnetic fields that exponentially decay with increasing distance from the interface into both half-spaces (media and the metal).

When the dimensions are reduced, boundary and surface effects become very important and thus the optical properties of small metal nanoparticles are dominated by such a collective oscillation of conduction electrons in resonance with incident electromagnetic radiation. In this case of a sub-wavelength scale particle, the overall displacement of the electrons with respect to the positively charged lattice leads to a restoring force, which in turn gives rise to specific particle-plasmon resonances depending on the geometry of the particle. (see Figure 4.3 below)

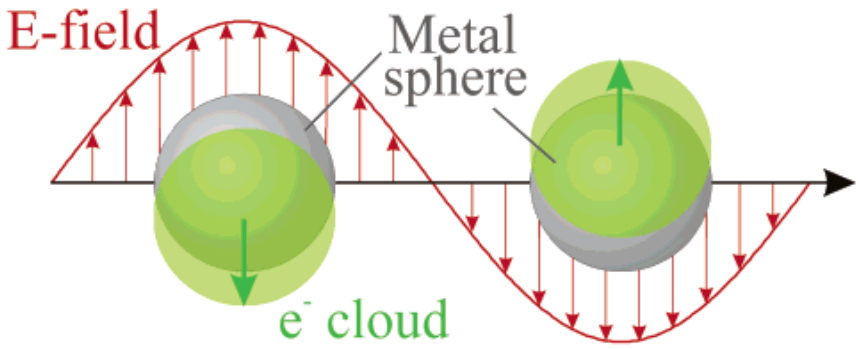

Figure 4.3. Schematic representation of the plasmon oscillation (shown in green) for spherical nanoparticles. (Image adapted from ref. 4)

In case of sharp edges or pointed shapes, extreme local accumulations occur that are accompanied by strongly enhanced optical fields. Ellipsoids and nanorods display two distinct plasmon bands related to transverse and longitudinal electron oscillations as shown in Figure 4.4, giving rise to the quadrupole and octopole absorbances. The longitudinal oscillation is very sensitive to the aspect ratio of the particles.

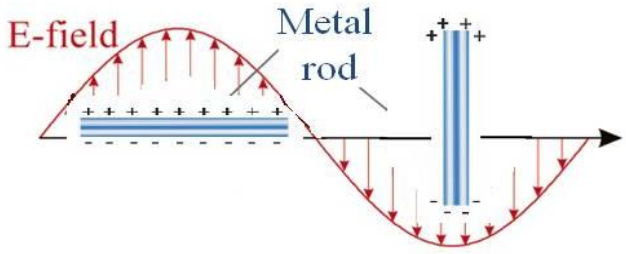

Figure 4.4. Schematic representation of transverse and longitudinal oscialltions in an anisotropic particle.

Metals, especially noble metals such as gold and silver have a large negative real part of the dielectric constant along with a small imaginary part. To account losses associated with electron scattering (ohmic losses) the imaginary part of the metals' dielectric function has to be considered[30]. Since these resonances arise from the particular dielectric properties of the metals, they can be easily modeled using the equations derived by Mie for the resolution of Maxwell equations for the absorption and scattering of electromagnetic radiation by small spheres[2] and their modification by Gans for ellipsoids.[31] According to the prediction by Mie theory[32], the expressions for the extinction cross section C_{ext} for very small particles with a frequency dependent, complex dielectric function, $\varepsilon = \varepsilon' + i\varepsilon''$, embedded in a medium of dielectric constant ε_m, this can be expressed as:

$$C_{ext} = \frac{24\,\pi^2 R^3 \varepsilon_m^{3/2}}{\lambda} \frac{\varepsilon''}{\varepsilon''^{\,2} + (\varepsilon' + 2\varepsilon_m)^2} \quad \ldots\ldots\ldots\ldots\ldots\ldots\ldots\ldots\ldots\ldots (7)$$

where R is the radius of the particle.

When condition $\varepsilon' = -2\varepsilon_m$ is fulfilled, the long wavelength absorption by the bulk metal is condensed into a single surface plasmon band. Mie theory holds true for dilute and non absorbing media as the condition expressed; for concentrated systems, the nanoparticles become closer to each other, and interactions between neighboring particles can arise, so that the models for isolated particles do not hold any longer, and different behavior of the particles are observed.

In this chapter, we observe the scattering and the absorption arising from the reaction solution comprising of chloro auric acid and cephalexin, as the gold nanoparticles are synthesized at various temperatures. The most striking finding is the evolution of a tight bimodal particle distribution. The spectra are supported by TEM micrographs where the morphology of the particles is exhibited.

4.2.Experimental Details

The one-step synthesis protocol is used as described in the previous chapter [33] to synthesize the antibiotic functionalized gold nanoparticles. A slight modification is made in this work, where 1×10^{-4} M chloroauric acid (Aldrich Inc.) was reduced by 10^{-5} M of the antibiotic cephalexin (a kind gift to us from Lupin Laboratories, India). Here, both the antibiotic and the chloroauric acid were first diluted to twice of their final concentrations into the distilled water before mixing them for the formation of nanoparticles. For the DLS studies, both the stock solutions are filtered through 0.22 μm syringe filters to remove any unwanted particles. Using DLS, both the stock solutions were checked carefully for the presence of pre-existing particle clusters (or dust particles) that might interfere with subsequent nucleation studies.[34] The 2× stock solutions were cooled to 5 °C, mixed in equal proportion to their final concentration and then placed into a quartz cuvette for light scattering measurements. The pH of the solution was monitored by using a digital pH meter (Cyberscan, Eutech Instruments). The pH was stable around ~3.7. Following the particle synthesis, the resulting colloidal gold nanoparticles suspensions remained stable without aggregation or precipitation. Glass cuvettes containing the mixed chloroauric acid/cephalexin solutions were placed inside the thermostatted sample holder of the DLS unit and were allowed to equilibrate to their set temperature (15, 25, or 35 °C) for 5 min. From then on, intensity autocorrelation functions of scattered light were collected continuously using acquisition times of 60 s per

correlation function. Throughout the experiment, the total intensity of scattered light changed dramatically due to the incessant nucleation and growth of strongly scattering gold colloids. Therefore, the measurement software protocol was set up to first measure the total scattering intensity and to adjust a variable neutral density filter in the detection arm accordingly to keep the avalanche photodiode count well below saturation. Relative scattering intensities were corrected for this variable attenuation.

4.3.Results and Discussions

4.3.1. DLS study of the system and its data analysis

In Figure 4.5A, we show the temporal evolution of the intensity correlation function of light scattered from the solution undergoing the synthesis of gold colloids at 15 °C. Due to the reduced synthesis rate, the early stages of the nucleation and growth of the colloidal gold particles are more readily resolved at T = 15 °C. Initially, no correlations are detected since the concentration fluctuations of the gold sol alone are too fast to be resolved by DLS.

Figure 4.5B displays the temporal evolution of the intercept of the intensity correlation function $g_1(\tau)$ versus the incubation time of the sample. A fit through the intercepts of $g_1(\tau)$ vs. incubation time with a simple sigmoidal functions faithfully reproduces the experimentally observed behavior, as expected for an "activated process" such as nucleation. Notice also the significant lag of the total scattering intensity compared to the upswing in the amplitude of the correlation function.

This implies that dynamic light scattering is a much more sensitive indicator of the nucleation event than static light scattering. There is a significant latency period of approximately 30 min before the onset of nucleation and growth of gold particles as detected by DLS. This latency period decreases significantly as the solution temperature is raised to 25 °C or to 35 °C. After a period of rapid increase, the $g_1(\tau)$ intercept eventually levels off around 0.78, below the theoretical limit of 1. The lower plateau value of 0.78 arises from contributions to the dynamic signal from purely static scattering off the various interfaces (air/glass/solution). Together with the zero intercepts of the intensity correlation functions, Figure 4.5B also shows the total intensity of scattered light during the synthesis of the gold colloids.

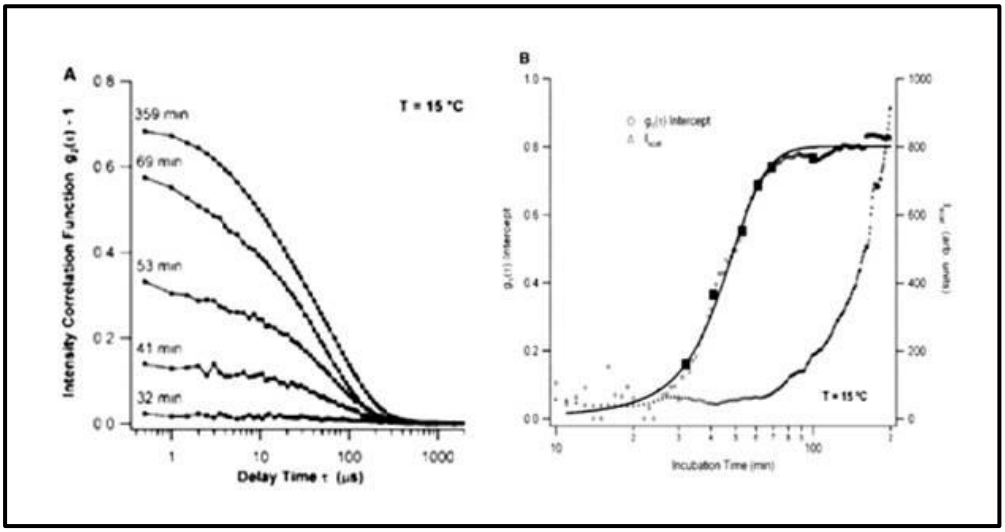

Figure 4.5. (A) Normalized temporal correlations of the intensity of scattered light, $g_2(\tau)$ - 1, vs. delay time τ obtained at different time points (see label on curve) during the synthesis of colloidal gold particles from chloroauric acid solution (10^{-4} M) in the presence of the antibiotic cephalexin (10^{-5} M), incubated at 15 °C. With increasing incubation period, the correlations of the scattered light arising from the gold colloids nucleating and diffusing in the aqueous suspension increases significantly. **(B)** Intercepts of the intensity correlation function of scattered light (O) and the overall intensity of scattered light (Δ) vs. the incubation time of the sample. The solid squares highlight the time points for most of the correlation functions displayed in (A) and their corresponding particle size distributions shown in (B).

Obviously, the rapid increase in the temporal correlations of scattered light (~30 min) significantly precedes the upswing in overall scattering intensity (~80 min), both of which are associated with the nucleation and growth of the gold colloid particles. This is an intriguing observation since increases in static scattering intensity are frequently used as indicators for the onset of nucleation events in supersaturated solutions.[35, 36] Our observations suggest that the correlation amplitude of dynamically scattered light is a much more sensitive and reliable indicator for nucleation events than "kinks" in static light scattering data. Nevertheless, DLS is unlikely to capture the actual nucleation event due to at least two complicating factors. First, the dynamic signal during the very early phases of nucleation is contaminated by contributions from residual dust and air inclusions. In addition, the shot noise of the photon detector limits resolution of very small populations of particles.

Figure 4.6A displays the particle size distributions obtained from the autocorrelation functions during the early stages of the nucleation and aggregation process (see also open squares in Figure 4.5B). Noticeably, the larger particle peak around 20-30 nm emerges ahead of the smaller aggregates near 1-2 nm, which appear only at 69 min. The particle distributions at all temperatures eventually showed two well-resolved particle peaks centered around 25 and 1 nm, respectively. At higher temperatures, the apparent delay between the emergence of the larger and smaller peak was much less pronounced. Notice that the minor contribution from the smaller colloids, which are well resolved in the correlation functions at later times, might not be readily resolved for the small intercepts and weak scattering intensities during the early stages of nucleation and growth (see Figure 4.5B).

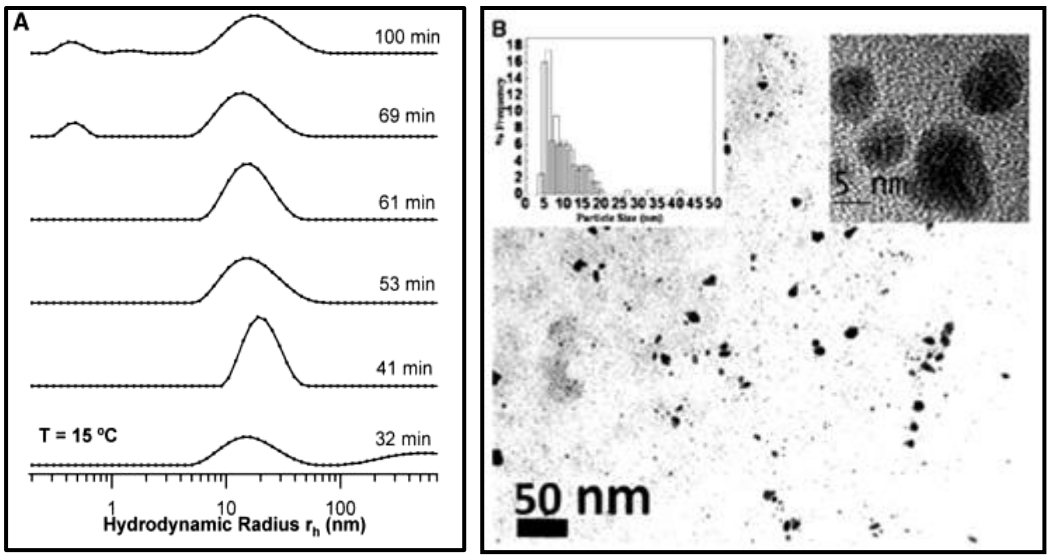

Figure 4.6. (A) Examples of particle size distributions obtained during the early phases of the synthesis of gold colloids in the presence of cephalexin during incubation at 15 °C. Figure 4.1B indicates at what point in the nucleation process these particle size distributions were obtained. In the display we also excluded third, larger peak (>500 nm) associated with dust and air inclusions present in the solutions. **(B)** TEM micrographs of the gold nanoparticles synthesized at 15 °C after 1 hour reaction time.

To further investigate this, in Figure 4.6B we have shown the TEM images on the particles pre-69 min, which essentially captures the growth behavior before 69 min. However, caution is required when interpreting this DLS result. First, as indicated by

the Stokes-Einstein relation (eq 5) and eq 4, the autocorrelation of light scattered by small 1-2 nm aggregates decays at rates of only few microseconds. Unfortunately, the correlation functions g1(t) remain rather noisy, particularly at these short delay times, until the amplitude of the zero-intercept is well above 0.5. In addition, the scattering intensity of the particles increases approximately quadratic with particle volume. As a result, a single particle of radius 25 nm will scatter one million times more light than a 2 nm particle. As is apparent from Figure 4.5B, the overall scattering intensity from the solutions remains rather weak prior to approximately 85 min into the experiment. In addition, the contribution to the scattering intensity from the small particles never exceeds 20% of the total scattering intensity (see Figure 4.8B). All these factors might collude to minimize the contributions of smaller particles to the dynamic light scattering signal during the very early stages of nucleation. In spite of these speculations, surprisingly, in Figure 4.6B, we observe that the larger particles have already formed within 60 min of reaction whereas the smaller particles (as observed in Figure 4.12B after the reaction is complete) are absent. The background spotting, observed as a lighter contrast compared to gold nanoparticles is probably attributed from the unreacted antibiotic. To confirm this we focused on the lighter contrast spots using HRTEM and we did not find any indication of crystallites unlike gold nanoparticles where strong lattice fringes were observed (inset in Figure 4.6B). The temporal evolution of the two peaks in the particle size distribution vs. the incubation time for samples at 15, 25, and 35 °C, respectively is summarized in Figure 4.7. Most strikingly, the particle distribution is bimodal with two narrow peaks located around ≈25 nm and 0.5-1.5 nm. Following a brief latency period, the two well-separated populations of gold nanoparticles emerge from the supersaturated solutions nearly simultaneously, with the larger particles slightly preceding the smaller particles particularly at the lowest reaction temperature of 15 °C. As discussed above, it is not obvious whether this apparent difference in latency of nucleation is not just a consequence of the limited detection sensitivity for the smaller aggregates. Two well-separated populations of gold colloids with surprisingly tight limits on their particle distributions emerged at all incubation temperatures. The radius for the peak of either population of gold colloids remained essentially unchanged throughout the entire observation period of several hours.

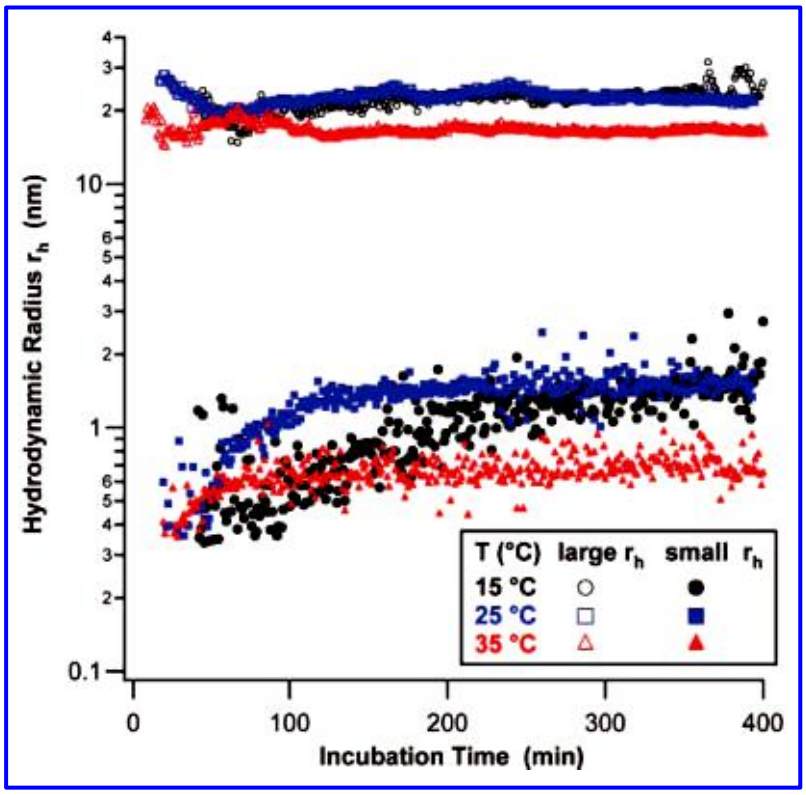

Figure 4.7. Changes in the mean particle size for both the small and the large gold colloids as a function of incubation period and solution temperature.

We are, therefore, cautiously concluding that both populations of gold nanoparticles nucleate essentially simultaneously. The observation of two different particle populations of distinct mean size are consistent with earlier observations made by the authors in a separate study (as discussed above) where the TEM micrographs showed the presence of larger particles surrounded by a large number of smaller particles.[33]

Figure 4.8A summarizes the temporal evolution of the relative scattering intensity from the solutions at T = 15 °C and 25 °C, respectively. In contrast to the relative distribution of gold colloids (Figure 4.7), the total number of colloidal gold particles rapidly increases throughout the incubation period. In addition, the synthesis clearly proceeds significantly faster at T = 25 °C than at T = 15 °C.

Following the initial lag-time for nucleation, the overall scattering intensity from these solutions rapidly increases with time, closely following a power law with exponents around 1.7. Figure 4.8B shows the corresponding changes in relative scattering intensity for the small vs the large colloidal particles over the same time

period. Similar to the overall sizes of the two colloidal gold particles, the relative populations for either peak does not appear to change throughout the nucleation and growth period shown in our data.

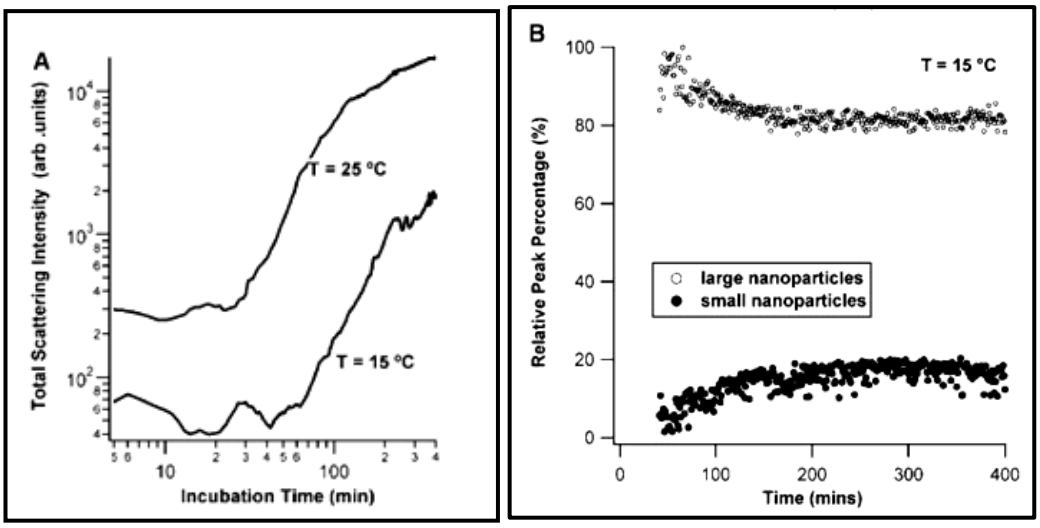

Figure 4.8. (A) Changes in the total intensity of scattered light during the synthesis of colloidal gold particles at T = 15 and 25 °C. Intensity data shown here have been corrected to account for neutral density filters inserted in front of the detector to prevent saturation. (B) Percentage of total light scattered by either population of colloidal gold particles during synthesis at T = 15 °C.

The results at T = 25 and 35 °C are comparable but have been omitted here for clarity. In stark contrast to the rapid increase in total scattering intensity, the relative contributions to the scattering intensity from either particle population remain nearly fixed at a ratio of approximately 20% for the small colloids versus 80% for the larger colloids. Again, this suggests the remarkable feature that both populations are growing at identical rates throughout the synthesis process. The chemical origin of the coexistence of two different size ranges with tight control over particle size, nucleation, and growth rates is not obvious to us, but does suggest that all three components of the synthesis are somehow tightly coupled to one another. We believe that this is the first report of simultaneous growth of two size ranges. It seems that various functional groups on the antibiotic molecules (cephalexin) might be playing a significant role in this process. We reported earlier, based on our NMR and XPS analysis, that as-synthesized particles are stabilized by the antibiotic molecules which get coated at the gold nanoparticle surfaces, helped by their sulfur moiety (Chapter 3).

4.3.2. UV-vis absorption spectroscopy data

The UV-vis absorption spectroscopy is another easy and established technique to characterize the gold nanoparticles due to their strong absorption in the visible to IR range due to the surface plasmon resonance (SPR) where the absorption peak width, intensity, and the wavelength are highly sensitive to the size, shape, and chemical environment around the gold nanoparticles. By solving Maxwell's equations with the appropriate boundary conditions for spherical particles, Gustav Mie quantitatively described the plasmon absorbance.[2] The origin of these "surface plasmon resonances" is attributed to the collective oscillation of the free conduction electrons induced by an interacting electromagnetic field.

The observation of the optical properties thus provides information about the particle size and shape. However, the measured values do not coincide quantitatively with Mie's theory.[37-39] These discrepancies are due to the fact that the idealizing assumptions are not met in reality.[40] Deriving an approximation for quasi-spherical particles and anisotropic particles obtained in a single system, therefore, is difficult.

The shape-factor, L, changes with both the size and shape of the crystals and is strongly influenced by surface defects, roughness, and the quality of facets. Gold nanoparticles made of less than 300 atoms display distinct optical and electronic properties compared to bulk. Size confinement results in new electronic and optical properties, which is a characteristic feature of noble metal nanoparticles.

Figure 4.9. Image of the vials containing gold nanoparticles synthesized by the cephalexin mediated method in aqueous medium at temperatures 15, 25, and 35 °C (vials A, B, and C), respectively.

In Figure 4.9, we have shown the image of the vials containing the gold nanoparticles synthesized at temperatures 15, 25, or 35 °C, labeled as A, B, and C respectively. The vial labeled A shows a weak purple color, whereas vials B and C show increasing trend toward the ruby red. The color of these suspensions confirms the presence of stable particles. The origin of the variation in the colors will be described in detail in the coming paragraphs. By monitoring absorption spectra, the growth and changes in the morphology of crystals can be monitored in real time[41]. There are various complicating factors affecting the optical properties of the nanoparticles like the presence of a substrate, the solvent layer and the particles that are close enough together that their electromagnetic coupling changes the spectra[4]. To understand further the growth dynamics of these particles, we carried out *in situ* UV-vis spectroscopy studies using a Cary 50 UV-vis spectrophotometer. Similar to the light scattering measurements discussed above, the absorption data was also obtained *in situ* at temperatures (15, 25, or 35 °C) at the intervals of each 15 min after placing the gold salt and antibiotic (mixed together as mentioned in the experimental section), inside the thermostatted sample holder. In this study, we showed the temporal evolution of the SPR peak of such particles at the different temperatures. Earlier studies on the temperature dependence of the SPR absorbance showed that the effect of temperature on the width, intensity and wavelength of the SPR peak is negligible, consistent with the fact that dephasing of the surface plasmon electron motion is a result of the electron-electron repulsion rather than electron-phonon interaction.[42] Hence, any difference that we observe in the SPR peak characteristic will be purely due to the change in the particle morphology itself and/or the chemical environment around the nanoparticles. In Figure 4.10, we have compared the temporal evolution of the SPR peaks in the solution phase at various temperatures (15, 25, and 35 °C) as shown in panels A, B, and C, respectively.

In each panel, we have followed the evolution of the absorbance spectra as a function of reaction time where the intensity of the surface plasmon resonance peaks increases as the number of particles grows in the solution at their respective temperatures. In panel A, we see a quite broad absorption band instead of well defined peak even after 6 h of reaction at 15 °C which is consistent with the light purple color seen in Figure 4.10A.

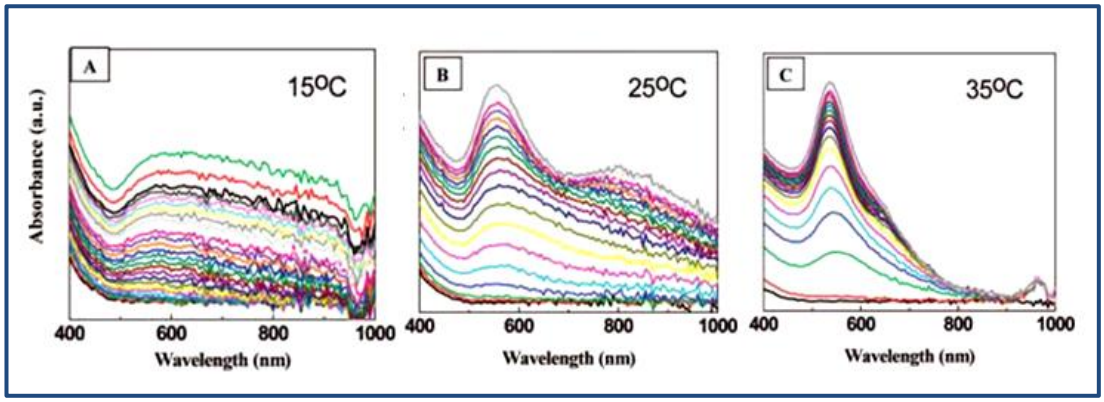

Figure 4.10. *In situ* UV-visible absorption spectroscopy measurements to demonstrate the temporal evolution of peaks due to the surface plasmon resonance absorption as the population of the nanoparticles increases in the solution. The panels A, B, and C show a group of spectra taken during the synthesis at temperatures 15, 25, and 35 °C, respectively, taken at an interval of every 15 min.

However, the DLS data shows the evolution of the two different size ranges of particles beyond 60 min (Figure 4.6A). As mentioned earlier, even though the gold nanoparticles are formed at this temperature, the reaction rate is quite slow. Here the limitation of conventional UV-vis spectroscopy in detecting the presence of lower population of the particles becomes clear. It is well known that the Rayleigh scattering is size-dependent and shape-dependent. It scales as the sixth power of the particle diameter (for a sphere); this places a lower practical limit on the size of particles that can be detected of 40-50 nm. Absorption techniques are able to measure the optical properties of particles as small as 2.5 nm[43].

Most of the studies in reporting the synthesis of gold nanoparticles rely on the UV-vis spectroscopy alone. However, the results here clearly indicate the difference in the sensitivity of both techniques. It is known that absorption spectroscopy is insensitive to the presence of gold nanoparticles less than 3 nm in size due to the quantum size effects as determined by the Kubo criterion.[44, 45] Only when the size of the particles increase beyond this limit, gold nanoparticles develop observable absorbance. Therefore, we do not expect the smaller particles shown in our DLS data to contribute to the absorption spectra in the UV visible range. In contrast, these particles are readily detected not only by DLS, as shown here, but also by TEM in our earlier published paper by Jagannathan et al.[33] Comparing the spectrum with the TEM micrographs obtained for particles at 15 °C temperature, note that for 2R > 25

nm, the extinction spectrum is dominated by quadrupole and octopole absorbance as well as scattering.[32, 46]

Though the population density of smaller particles is high, they appear to have aggregated/coalesced into larger, mostly anisotropic particles giving rise to the longitudinal mode of anisotropic absorbance in the range from 700 to 1000 nm (light purple color), which decreases as the reaction temperature is raised to 25 °C, as seen in the Figures 4.9 and 4.10 (panel B). At 35 °C this absorbance is almost absent owing to the fast reaction of the system at this temperature, consistent with the quasi-spherical particles shown in our previous studies.[33]

In Figure 4.11, we have plotted the time-dependent change in the λ_{max} (panel A) and intensity (panel B) of the transverse mode of the SPR peaks at the reaction temperatures 25 and 35 °C (obtained from Figure 4.10B and 4.10C) with the error bars (due to the broadness of the peaks). Due to the absence of the well defined transverse/longitudinal modes of the SPR peaks at 15 °C, we could not plot the peak-shift and the peak-intensity with respect to time.

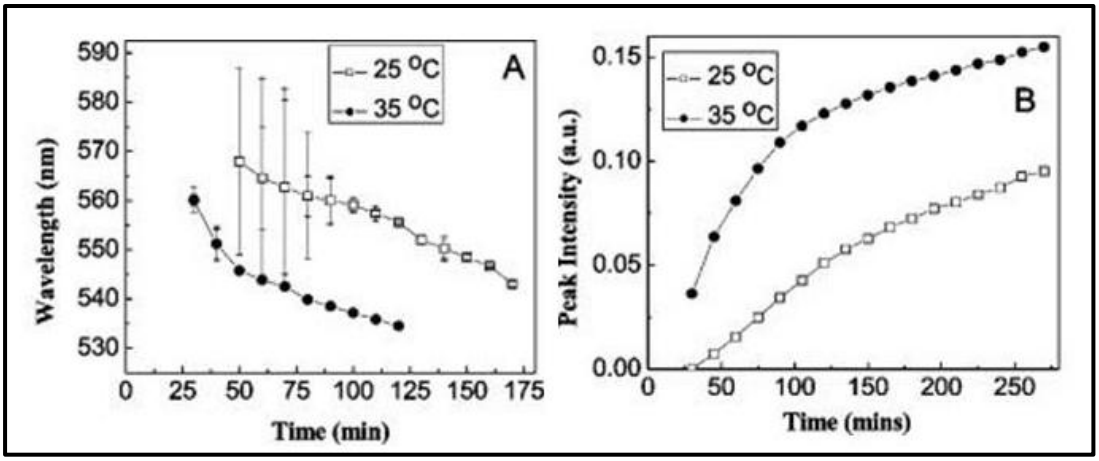

Figure 4.11. (A) Time-dependent hypsochromic shift in the wavelength of the surface plasmon resonance absorption peaks during the synthesis for reactions at temperatures 25 and 35 °C. (B) Temporal evolution in the absorption peak intensity for the reactions at 25 and 35 °C.

In panel A, we observe that the λmax shifts toward higher energies as the reaction proceed (for both 25 °C and 35 °C) which is quite significant and remarkable. At 35 °C, this hypsochromic shift is quicker and larger, which is perhaps due to the particle morphology shifting toward quasi-spherical geometry[4, 47] as the growth of the

particle proceeds at 25 and 35 °C. The increase in the SPR peak intensity with reaction time shows an increase in the population of nanoparticles, which is much faster for the reaction at 35 °C, as expected, and the growth curve reaches the flatness quite fast.

4.3.3. TEM and SAED measurements

To confirm the morphology of the particles and the presence of the bimodal distribution as predicted by the dynamic light scattering results, we obtained TEM micrographs of the samples. For this purpose, we prepared the samples by drop coating diluted cephalexin bound gold nanoparticles solution on carbon-coated copper TEM grids. The results for various temperatures are presented in the Figures 4.12, 4.13, and 4.14, where the panels represent the typical morphologies at different length scales.

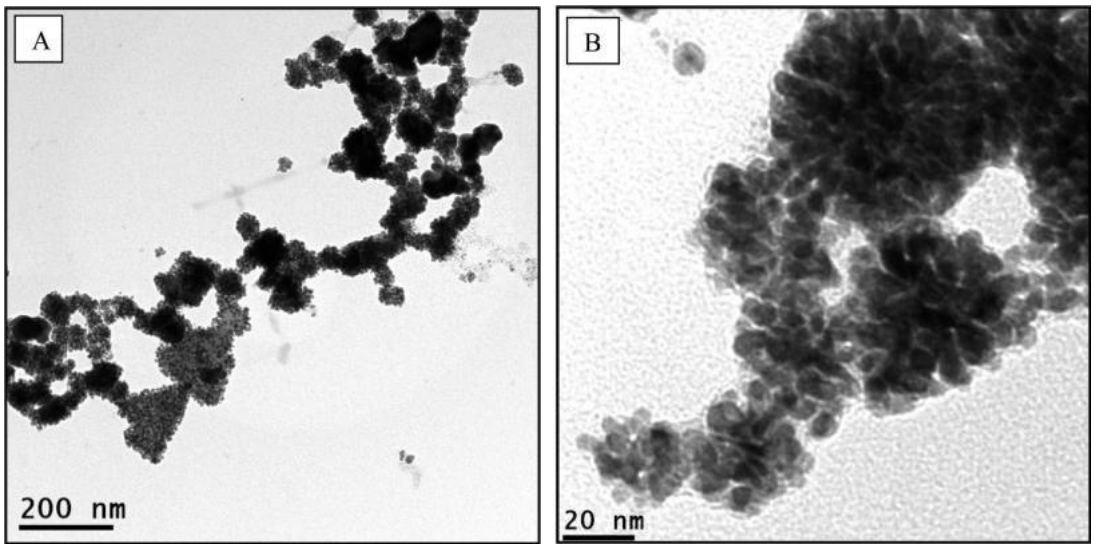

Figure 4.12. TEM micrographs of the gold nanoparticles synthesized at 15 °C (A and B represent images at different scales).

Figure 4.12A and B represents the particle morphology for the synthesis at 15 °C, where the reaction rate is quite slow. In this panel we can clearly see two different size ranges of particles. The big clusters (~30 nm) are surrounded by a large number of smaller particles. The larger clusters (average diameter ~ 30 nm) at this temperature seems to be a collection of smaller particles (~1-3 nm) and show the

broad SPR peak and light purple color due to their non-spherical morphologies. The observation of two different size ranges is consistent with the DLS results.

However, at 25 °C (Figure 4.13), the clusters of particles appear to fuse to form the particles of increasingly quasi-spherical geometrical as shown by a relatively lower intense longitudinal SPR peak and red color. At this temperature also the larger particles coexist with the smaller particles (1-2 nm). The particles though appear to be facetted and still contribute to the Near Infra-Red (NIR) peak observed in Figure 4.10B.

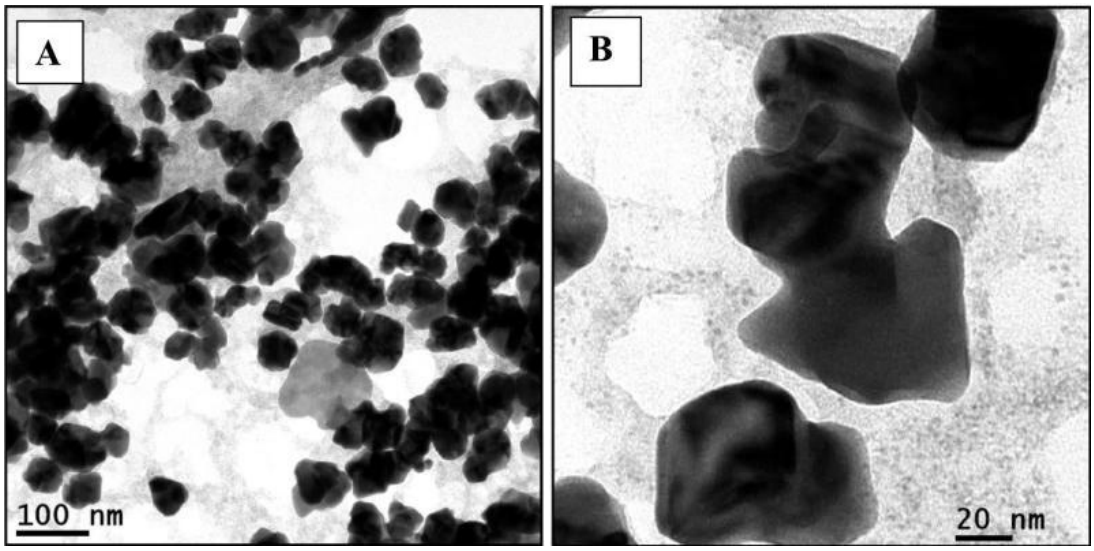

Figure 4.13. TEM micrographs of the gold nanoparticles synthesized at 25 °C (A and B represent images at different scales).

In Figure 4.14, we have shown the particles grown at 35 °C. In comparison to the particles grown at 15 and 25 °C, here the majority of the particles are spherical in shape due to faster reaction rate, which leads to the spherical shape and complete suppression of the longitudinal modes.[14]

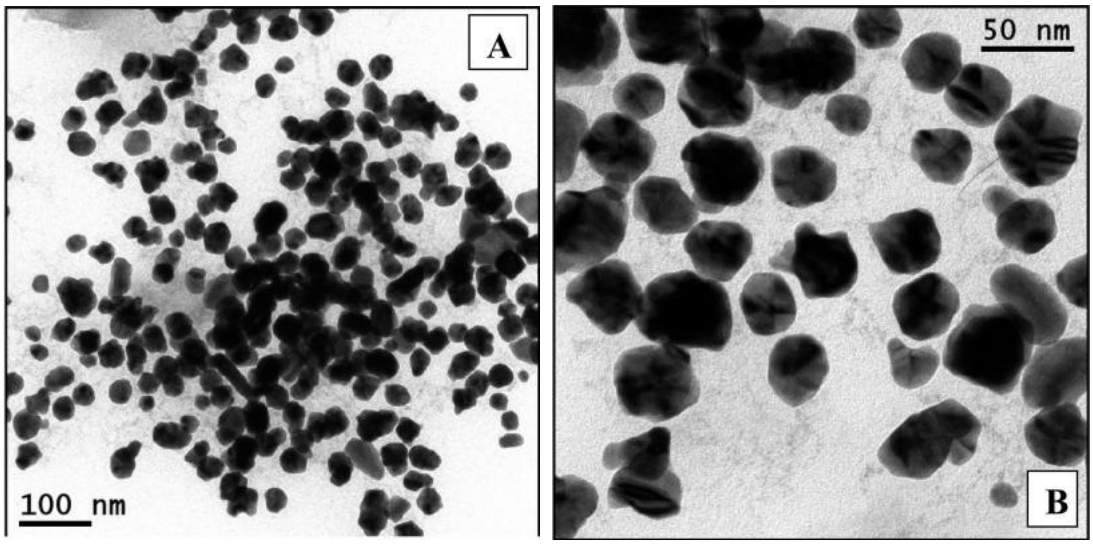

Figure 4.14. TEM micrographs of the gold nanoparticles synthesized at 35 °C (A and B represent images at different scales).

We did not pursue synthesis at temperatures higher than 35 °C as it would degrade the antibiotic. To check the crystalline nature of the as-synthesized particles, we also took the snap-shots of the selected area electron diffraction (SAED) patterns of the gold nanoparticles at respective temperatures. The results are shown in Figure 4.15, which demonstrates nice spot and ring patterns for the particles confirming the nice crystalline structure.

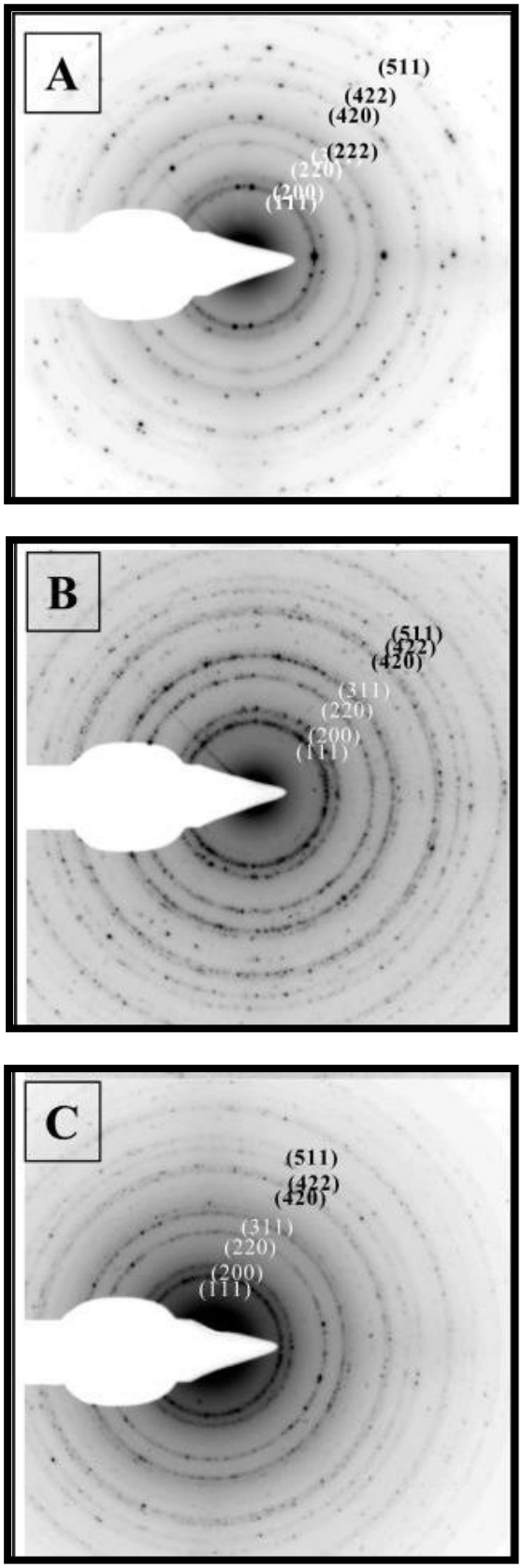

Figure 4.15. Selected area electron diffraction (SAED) patterns of gold nanoparticles synthesized at temperatures 15 °C (A), 25 °C (B), and 35 °C (C), respectively, showing nice crystallanity in all the three cases confirming the formation of crystalline gold.

4.4. Conclusion

Overall, the TEM results in combination with light scattering and absorption studies exhibit a highly unusual and surprising nucleation and growth processes for gold nanoparticles synthesis mediated by the presence of cephalexin. In addition, these two nanoparticle populations reach their respective final sizes very rapidly and then cease growth altogether. At the same time, the total number of gold colloid continues to grow rapidly, and their rate of formation is a sensitive function of incubation temperature. It is intriguing to note that, at all the temperatures, we observe bimodal distribution of particles in a homogeneous system. These observations raise important fundamental questions relating to the nucleation and growth mechanisms. Additionally, this study shows the relative importance of absorption and scattering processes, and how these affect the data acquirements. This study can be very useful to determine and optimize some of the physical properties of nanoparticles by controlling their shape and size during and after a growth process.

4.5. References

1. Faraday, M. (1857) *Philos. Trans. R. Soc.* 147, 145
2. Mie, G. (1908) *Ann. Phys.* 25, 377
3. (2006) The Research on The Theory Relation Between The Shape and Extinction Spectrum of Nanoparticles. http://supramol.jlu.edu.cn/group/Weiqing
4. Lance Kelly, K., *et al.* (2003) *J. Phys. Chem. B* 107, 668
5. Finney, E.E., and Finke, R.G. (2008) *J. Colloid Interface Sci.* 317, 351
6. Wang, T.S., *et al.* (1996) *Chem. Mater.* 8, 1161
7. Sun, Y., and Xia, n. (2002) *Science* 298, 2176
8. Becker, R., and Doring, W. (1935) *Ann. Phys.* 24, 719
9. Volmer, M., and Weber, A. (1926) *Z. Phys. Chem.* 119, 277
10. Turnbull, D. (1950) *J. Appl. Phys.* 21, 1022
11. Turnbull, D., and Fisher, J.C. (1949) *J. Chem. Phys.* 17, 71
12. LaMer, V.K., and Dinegar, R.H. (1950) *J. Am. Chem. Soc.* 72, 4847
13. Turkevich, J., *et al.* (1951) *Discuss. Faraday Soc.* 11, 55
14. Turkevich, J. (1985) *Gold Bull. (London, U.K.)* 18, 86
15. La Mer, V.K. (1952) *Ind. Eng. Chem.* 44, 1270
16. Granqvist, C.G., and Buhrman, R.A. (1976) *J. Appl. Phys.* 47, 2200
17. Overbeek, J.T.G. (1982) *Adv. Colloids Interface Sci.* 15, 251
18. Abeâ€²cassis, B., *et al.* (2007) *Nano Lett.* 7, 1723
19. Ingham, B., *et al.* (2008) *J. Phys. Chem. C* 112, 2820
20. Shankar, S.S., *et al.* (2004) *Nat. Mater.* 3, 482
21. Holoubek, J. (2007) *J. Quant. Spectrosc. Radiat. Transfer* 106, 104
22. (1972) *Light scattering from polymer solutions*. Academic Press
23. Kerker, M. (1980) *The scattering of light and other electromagentic radiation*. Academic Press
24. Brillouin, L. (1914) Light diffusion by a homogeneous transparent body. *Comptes Rendus Hebdomadaires Des Seances De L Academie Des Sciences* 158, 1331-1334
25. Brillouin, L. (1922) *Journal De Physique Et Le Radium* 3, 362
26. Schärtl, W. (2006) *Light Scattering from Polymer Solutions and Nanoparticle Dispersions*. Springer

27. Brown, W. (1993) *Dynamic light scattering: the method and some applications*.

28. Chu, B. (1991) *Laser Light Scattering: Basic Principles and Practice*.

29. Cummins, H.Z., and Pike, R. (1973) *Photon correlation and light beating spectroscopy*.

30. Novotny, L., and Hecht, B. (2006) *Principles of nano-optics*. Cambridge University Press

31. Gans, R. (1912) Über die Form ultramikroskopischer Goldteilchen. *Annalen der Physik* 342, 881-900

32. Bohren, C.F., and Huffman, D.R. (1983) *Absorption and Scattering of Light by Small Particles*.

33. Jagannathan, R., *et al.* (2007) *J. Phys. Chem. C* 111, 6933

34. Parmar, A.S., *et al.* (2007) *Biophys. Chem.* 129, 224

35. Muschol, M., and Rosenberger, F. (1997) *J. Chem. Phys.* 107, 1953

36. Arnaudov, L.N., and De Vries, R. (2005) *J. Biophys.* 88, 515

37. Kottmann, J.P., *et al.* (2001) *Chem. Phys. Lett.* 341, 1

38. Kottmann, J.P., *et al.* (2001) *Phys. Rev. B: Condens. Matter Mater. Phys.* 64, 253402

39. Jensen, T.R., *et al.* (1999) *J. Am. Chem. Soc.* 103, 2394

40. Pinchuk, A., *et al.* (2004) *Surf. Sci.* 557, 269

41. Pérez-Juste, J., *et al.* (2005) *Coordination Chemistry Reviews* 249, 1870

42. Link, S., and El-Sayed, M.A. (1999) *J. Phys. Chem. B* 103, 4212

43. Boyer, D., *et al.* (2002) *Science* 297, 1160

44. Kubo, R. (1962) *Phys. Lett.* 1, 49

45. Alvarez, M.M., *et al.* (1997) *J. Phys. Chem. B* 101, 3706

46. Kerker, M. (1969) *The Scattering of Light and Other Electromagnetic Radiation*.

47. Jin, R., *et al.* (2003) *Nature* 425, 487

SOLUBILISING CURCUMIN, SYNTHESIZING GOLD NANOPARTICLES AND THEIR ANTI-OXIDANT PROPERTY

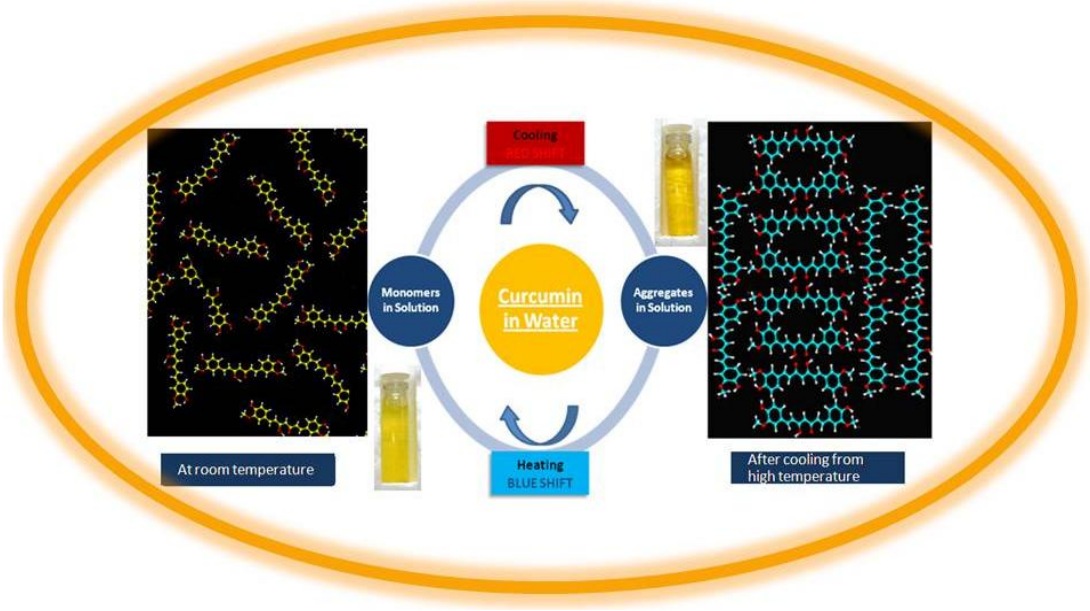

Curcumin is a phytochemical that gives yellow color to turmeric and is responsible for most of the therapeutic effects of turmeric. The keto-enol-enolate equilibrium of this heptadiene-dione moiety determines its physiochemical and antioxidant properties. However, solubility of curcumin is very low in water at neutral pH and room temperature, which decreases its bioavailability. The mechanism behind its solubility issues at various temperatures and the influence of interplay of temperature, dielectric environment and intra/intermolecular H-bonding in curcumin leading to aggregation-disaggregation in various temperature regions is investigated. A remarkable change in the temperature dependent electronic transition behavior of the molecule in water is observed. The study indicates that it is perhaps the breaking of the intra-molecular hydrogen bonding which leads to the exposure of the polar groups and hence responsible for the dissolution of curcumin at higher temperature. We believe that formation of inter-molecular aggregates might be responsible behind a better room temperature stability of the molecules after cooling its aqueous suspension from 90^{o}C to 25 ^{o}C.

The synthesis of gold nanoparticles using curcumin in water around 90 °C is carried, thereby increasing the possibility of enhancing the bioavailability and drug-action. In this method curcumin acts both as a reducing agent and as a capping agent. The nanoparticle size (~20 nm) is quantified by transmission electron microscopy. The synthesized nanoparticles are very stable and show good anti-oxidant activity.

The study in this chapter began as an endeavor to functionalize gold nanoparticles with a strong anti-oxidant such as curcumin, which would have multiple advantages. This chapter comprises of two parts: **Part I** deals with the study of the temperature-dependent spectroscopic behavior of curcumin in water and **Part II** comprises of the use of the aqueous curcumin to synthesis gold nanoparticles and their characterization.

5.1.1. PART I: Study of dissolution of curcumin in water

Turmeric is a wonder drug[1] which has been therapeutically used in the Indian subcontinent for various ailments including wound-healing, skin-lightening (as a cosmetic), anti-inflammatory and antimicrobial since time-immemorial.[2] Interestingly, it was also included as an inseparable part of the Indian/Asian cuisine in the form of spice and coloring agent since time immemorial. Curcumin or diferuloylmethane (1, 7-bis [4-hydroxy-3-methoxyphenyl]-1, 6-heptadiene-3, 5-dione), is a major component (2-6%) of turmeric, isolated from rhizomes of the perennial herb *curcuma longa* and is being recognized as being responsible for most of its therapeutic effects.[3-5] Curcumin, also called as the Indian solid gold, has highly active medicinal properties such as anti-oxidant and anti-inflammatory, anti-cancer, anti-tumor, inhibitor of angiogenesis and neuroprotective, to name a few.[6-8] Owing to its wondrous actions in protecting the human body, the molecule is being recently revisited using modern science and technological tools, and is revived back from the age-old ayurvedic medicine to validate the age-old practices in a scientific way. Neurodegenerative diseases like the Alzheimer's disease are associated with the formation and accumulation of proteins like amyloid-beta (Aβ) plaque in this case, that leads to declined memory and other neurocognitive functions of the brain.[9] (Figure 5.1)

Figure 5.1. From the cover page of the weekly magazine Science News, 2007 (Sept 15, vol 172, no.11)

Curcumin has shown potent anti-amyloidogenic effects for Alzheimer's amyloid fibrils *in vitro* [10] as well as *in vivo* [11]. It is reported that the low molecular weight and the hydrophobic nature of curcumin allows it to penetrate the blood brain barrier effectively and bind to the beta amyloids.[11] Recently scientists have established a direct link between its anti-neurodegradation properties as well as relatively lower number of neurological diseases in Indian subcontinent (such as Alzheimer's and Parkinson's disease) [11, 12] and have attributed it to its direct intake as part of the regular diet in Indian curries. Curcumin has also shown to reduce induced-memory deficit in rat.[13] An extensive research on curcumin and its biomedical pathways reveal that curcumin possesses strong inflammatory and anti-oxidant properties, contributing to antiseptic and analgesic, anti-bacterial [14, 15] and anti-fungal [16], anti-malarial and insect repellant properties.[17] It is also recently reported that curcumin kills tumor cells, suppresses lipid peroxidation and angiogenesis [18] by affecting the action of a wide variety of growth factors and enzymes. Curcumin has been shown to down-regulate the activity of human EGFR-2 (called HER2/neu), a growth factor

receptor closely linked with cancer of the breast, lung, kidney and prostate.[19] It is reported to be cancer preventing and cancer curing as well. [6, 19, 20] Noting its curing abilities, curcumin is studied for widespread clinical applications. [21] The immunomodulatary effects of curcumin has been studied in depth and shown that it exerts either null or beneficial effects on cellular immune functions *in-vivo*.[22]

Various studies have shown that it is safe to use curcumin even at high doses. In spite of all the medicinal properties exhibited by curcumin, it is not yet a pharmacological drug due to its very low bioavailability. Owing to extremely low solubility of curcumin in water, it has a very poor bioavailability.[23] In humans, after 1h of administration of 4-8 g of curcumin, showed peak plasma levels of 0.41–1.75 μM [24] whereas in an oral dose, the peak plasma level of curcumin was at 11.1 nmol/L.[25] Despite its lower bioavailability, the therapeutic efficacy of curcumin against various human diseases, including cancer, cardiovascular diseases, diabetes, arthritis, neurological diseases and Crohn's disease, has been widely documented as mentioned above. The potential of therapeutic applications has triggered an interest in manipulating the solubility of curcumin in water by chemical modifications of the molecular structure. However, its stability and solubility in water still remains poorly understood. Its promise as an efficacious and safe drug is precluded due to low aqueous solubility and consequently, poor bioavailability [23, 26] hindering the direct use of curcumin as a biomedicine. The strong hydrophobicity of the conjugated alkene chain and the unavailability of polar group render the molecule insoluble or sparingly soluble in polar solvents. Curcumin is practically insoluble in water at neutral pH. However, in slightly acidic media and possibly in the interior of cell membranes, it is likely to exist in the keto form. This form appears to favor H-atom transfer reactions, [27] thus playing a crucial role in the antioxidant action of curcumin. For ages, curcumin has been consumed in the form of powdered turmeric added into oil, milk or water for Indian curries while cooking at high temperatures. Enhanced bioavailability of curcumin as a drug in the near future is likely to bring this promising natural product to the forefront of therapeutic agents for treatment of human disease. Henceforth, several methods of conjugation have been adopted for enhancing the solubility and/or its bioavailability (Part II). It is important to note that the expected phase transfer from organic phase to aqueous phase in the human body

is quite less and administration of the drug in the aqueous phase may help in increasing its bioavailability.

Keeping in mind these challenges, present study involves experiments to solubilize curcumin by heating it in the aqueous medium and performing detailed in-situ UV visible spectroscopic studies to investigate various aspects of dispersion such as the effect of medium on the UV-vis absorption peak, peak shape and the absorption maxima, size of the agglomerates, etc.

Though the UV visible spectroscopy is largely accompanied in the past few decades by Raman Spectroscopy, ESCA studies, NMR spectroscopy, nonetheless it is still a very powerful tool in studying the molecules that absorb in the UV visible radiation. Our goal in this study is to investigate and perform a systematic study on whether curcumin gets dissolved in water by heating it at relatively higher temperature and thereupon the effects of heating on the structural stability as well as long term solubility of the drug. In a previous study by Kurien et al.,[28] the mechanism of dissolution of curcumin in water at high temperature is not explained and the quantitative data on its solubility in water is erroneous, as it is calculated from the standard curve of curcumin in methanol, neglecting the corresponding solvent effects in λ_{max} and ε (molar extinction coefficient), and intensity changes due to the specific preferential solubility in different solvents.

A number of investigators have studied the structure of curcumin, solutions of curcumin in different organic solvents, predictions of the electronic and vibrational excitations and their experimental data; however, a detailed study of curcumin in water at different temperatures is not reported. It is observed that the spectrum of curcumin in water is complicated, uniquely temperature-dependent and different from what is obtained in organic solvents.

5.1.2. Results and discussions

The purified curcumin used in this study was a kind gift from Dr. K. J. S. Rao and Dr. P. Srinivas, Central Food Technological Research Institute (CFTRI), Mysore, India. The purity of the as-received curcumin is tested by using techniques such as UV-vis spectroscopy (Figure 5.4), FTIR spectroscopy (Figure 5.10), NMR spectroscopy (Figure 5.9) and HPLC (Figure 5.11).

5.1.2.1. Temperature dependent UV-vis absorption spectroscopy of curcumin in water and effects of intra/inter-molecular H-bonding on the electronic transitions

In Figure 5.2A, we have shown the structure of curcumin. Here, the β-di-ketone moiety undergoes keto-enol tautomerisation[29] and the molecule exists in a planar, intra-molecularly hydrogen-bonded form; both in solution as well as in the solid state.[30]

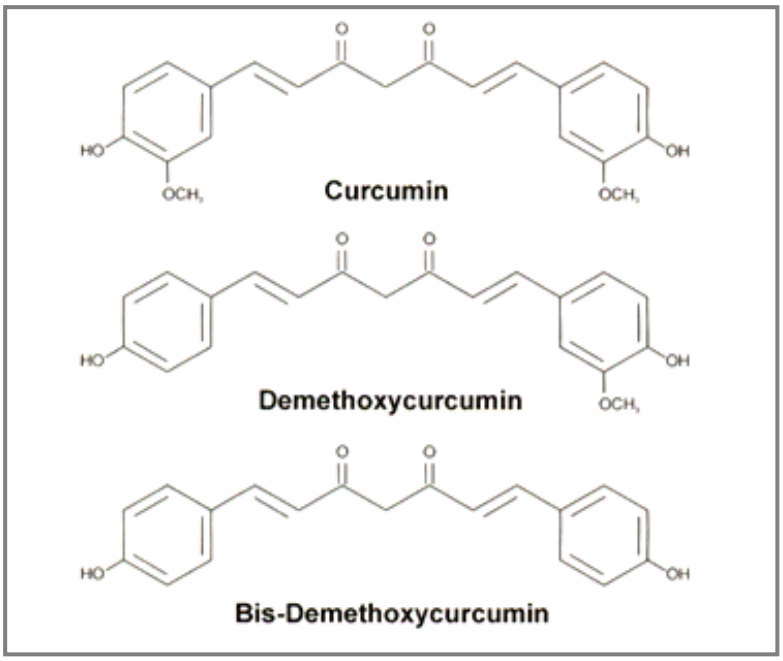

Figure 5.2. Structure of (A) curcumin, (B) demethoxycurcumin and (C) bis-demethoxycurcumin.

Curcumin is totally hydrophobic in nature due to the lack of any polar groups in the molecule as well as due to the stretch of conjugated back-bone (heptadiene) of curcumin.

The visible and ultraviolet spectra of organic compounds (like curcumin) represent the transitions between the electronic energy levels. These transitions are generally between a bonding or lone-pair orbital and an unfilled non-bonding or anti-bonding orbital. The maximum absorption wavelength of the spectroscopy of the compound is a measure of the separation between the energy levels of the orbitals concerned. An isolated double bond / lone pair of electrons gives rise to a strong absorption

maximum around 190 nm [31] whereas presence of conjugation reduces the energy separation between the orbital occasioned by absorption at longer wavelengths. In organic solvents, the enolisation of the diketone group in curcumin allows conjugation between the π-electron clouds of the two vinylguaiacol parts. This leads to a common conjugated chromophore, resulting in reduction in energy. Due to the low-energy π- π* excitation of that chromophore, the solution of curcumin in organic solvents (primarily ethanol or methanol) typically absorbs around ~420 nm thus exhibiting a bright yellow color. The n- π* transition, due to excitation of an oxygen lone-pair electron to the anti-bonding π-orbital of the carbonyl group in curcumin is observed around 262 nm in methanol.

However, in aqueous systems like water, it is understood that at alkaline pH, the acidic phenol group in curcumin donates its hydrogen, forming the phenolate ion that enables curcumin into dissolution in water. However, the molecule is not stable for long at neutral and alkaline pH and gets easily degraded into compounds like vanillin, ferulic acid, etc. Below pH 7, curcumin is stable but parallel with the decreasing pH values, the dissociation equilibrium shifts towards the neutral form of very low aqueous solubility. Due to this process, significant change of the UV-vis absorption spectrum of curcumin can be observed at acidic pH values. However, in neutral pH, it is practically insoluble at room temperature.

To check the effect of temperature on the solubility and stability of curcumin in water, we took about 2 mg of curcumin in 3 ml of deionized water (purified through a Millipore Milli-Q system with a resistivity of 18 MΩ/cm) at neutral pH and performed an *in situ* temperature dependent absorption spectroscopy up to 95 °C, with spectrum acquisition at an interval of every 5 °C rise in temperature.

Figure 5.3A shows the spectra of curcumin in water as the temperature is increased from 25 °C to 95 °C. We observe that as the temperature is increased, the peak intensity also increases around wavelengths 237 nm, 345 nm and 419 nm and the color of the solution turns turmeric yellow. The increase in intensity of the peak above 400 nm is plotted as a function of temperature in Figure 5.3B. A comparision of the spectrum of curcumin in water and the spectrum of curcumin in methanol is shown in Figure 5.3C. This will help in understanding the following explanation.

We observe solvatochromic shifts in the temperature-dependent absorption spectroscopy of curcumin in water as we compare the spectrum of curcumin in methanol (see Figure 5.3C) and in water (more polar compared to methanol) (Figure 5.3A). In general, the solvent effects on the π- π* and the n- π* transitions could be red-shifted or blue-shifted depending upon the polarisabilities of the solute-solvent interactions and thereof their effects on the electron reorganization in both the solute and the solvent. Most transitions result in an increase in the polar nature in the excited state than the ground state. Distortions of the chromophore may also lead to red or blue shifts depending on the nature of the distortion.

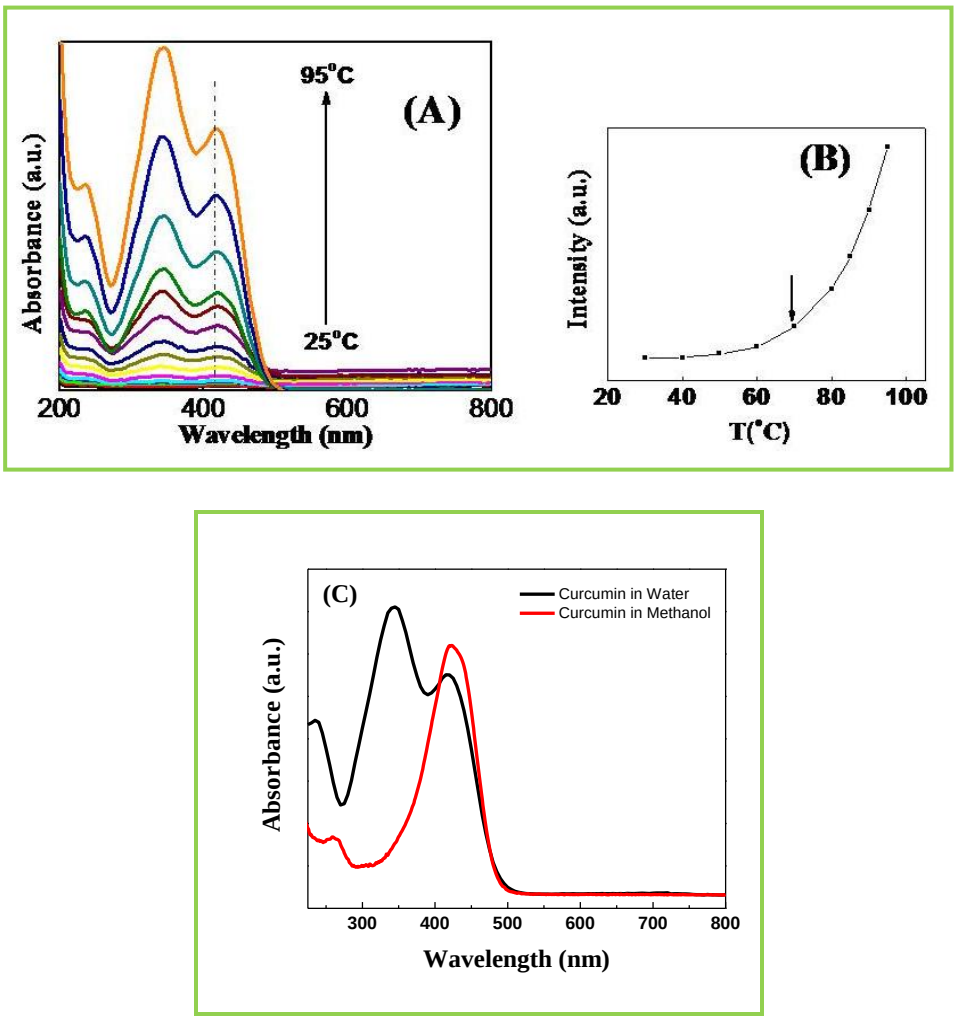

Figure 5.3. (A) Temperature dependent UV-Visible spectra of curcumin in water, **(B)** Change in intensity (of absorption at λ_{max} ~ 420 nm) vs. temperature and **(C)** Comparison spectrum of curcumin in water with curcumin in methanol.

In the case of weak forbidden n- π* transitions of the oxygen lone-pair in ketones, the solvent effect is due to the lesser extent to which the solvents can H-bond to the carbonyl group in the excited state. In methanolic solution of curcumin, the absorption maxima of the n- π* transition is at 262 nm, whereas in aqueous solution the maximum is at 237 nm. Clearly the n- π* transition is blue-shifted as we move from methanol to water. The effect of temperature seems not to affect the structure of this electronic transition and thus blue-shift is due to the solvent effect.

However, the π- π* transitions of curcumin in water is complicated unlike the n- π* transition. In case of the π- π* transition, generally the opposite effect occurs where the dipole-dipole interactions with the polar solvent molecules will lower the energy of the excited state than that of the ground state. Thus, we expect a red shift for the π- π* transition as we go from methanol to water. However, we note that the absorption peak for the π- π* transition in methanol is at 420 nm and in water, we observe two peaks at about 345 nm and 419 nm; note here that the intensity of the peak at 345 nm is more than that of the peak at 419 nm. The evolution of two absorption peaks for the π- π* transitions of curcumin in water indicates change in the tautomeric form of the keto-enol-enolate group in curcumin, due to both the solvent effect and the temperature. Temperature, *per se*, does not affect the signature of the peaks in the absorption spectroscopy. We see that the absorption spectrum of curcumin in methanol (boiling point of methanol is 64.7 °C) does not change with varying temperature, as shown in Figure 5.4, except mild decrease in intensity with increase in temperature due to the Boltzmann distribution of the populations at ground state at different temperatures.[32]

It appears that the resonance stability in the keto-enol-enolate is changed sharply as the temperature is increased. The thermal energy provided by heating could break the intra-molecular H-bonding of the keto-enol-enolate group in curcumin exposing the polar groups to the solvent. However, instead of a red-shift caused by more dipole-dipole interactions between curcumin and water molecules, we observe a remarkable blue-shift in the peak at 345 nm.

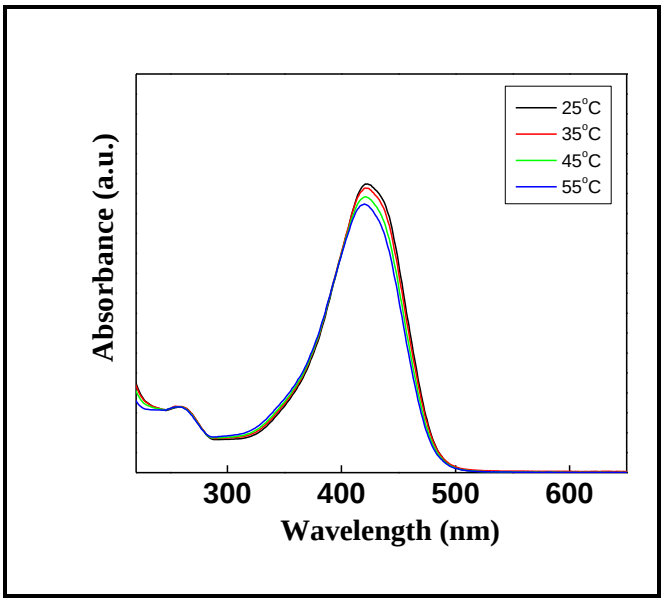

Figure 5.4. Temperature dependent UV-visible spectroscopy of curcumin in methanol

The blue-shift could be due to two factors:

(1) the high temperature of the solution could hinder the interaction between the solute and the solvent, preventing them to form inter-molecular H-bonding, and hence reducing the dipole-dipole interactions and increasing the energy, and

(2) the opening of the cyclic moiety (keto-enol-enolate group) in curcumin, going into its keto form, has lowered the conjugation effect of the molecule and thus increasing the energy.

Thus, as the temperature of the sample is increased, it is observed that the positions of the uncoupled absorption peaks of the π- π* transition moves to higher frequency. This is considered to result from a decrease in the H-bond strength between the water molecules and curcumin, at high temperatures, where the keto-enol/keto groups of curcumin could have been available for interaction with water molecules (due to breakage of intra-molecular H-bonding). As the temperature increases, the H-bond strengths become progressively weaker as a result of increased distortion and elongation of the H-bonds. With respect to the absorption characteristics of the molecule, it is evident that there are environmental changes caused by the breakdown of the intra-molecular H-bond in the keto-enol tautomer as the temperature is raised, leading to the change in the electronic transition energy. And

as the conjugation decreases, the wavelength of the absorption maximum also decreases. Both non-specific dipolar interaction and specific H-bonding interaction play an important role in the position of the absorption and fluorescence maxima of any sample.

5.1.2.2. Effect of temperature on the spectrum of curcumin in water, solvent effect and its proposed mechanism

To understand the process involved, we acquired in situ UV-vis spectroscopy of curcumin in water with heating, cooling and re-heating, as shown in Figure 5.5A. Upon heating to about 90 °C, we obtain the spectrum (black curve) similar to what we saw in Figure 5.3A. However, upon cooling, to room temperature (25 °C), there is a remarkable change in the absorption spectra (red curve).

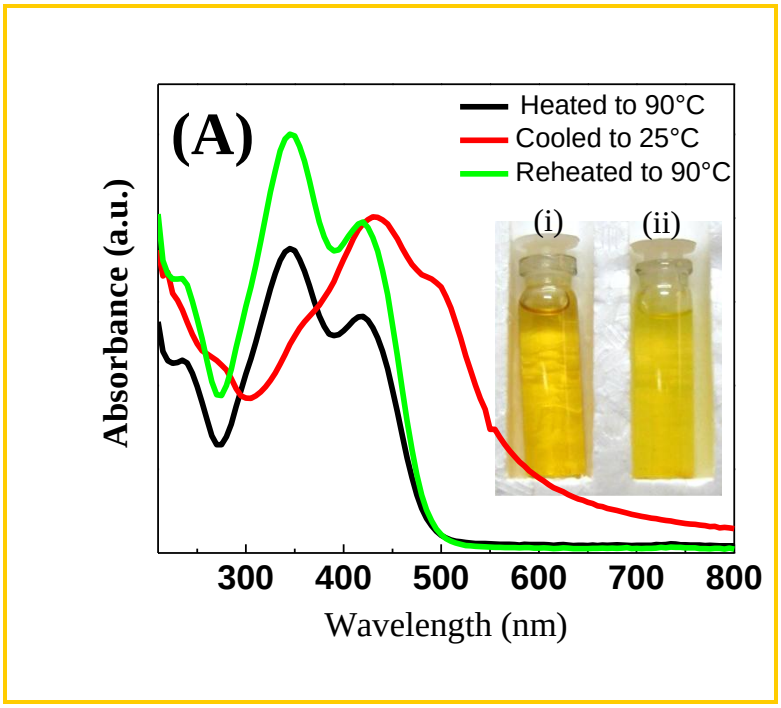

Figure 5.5. (A) UV-Visible Spectroscopy of curcumin in water; the graph shows spectra taken at 90 °C, cooled back to room temperature ~ 25 °C and reheated to 90 °C. Inset: (i) Optical transmission of curcumin in water at 90 °C and (ii) Turbid solution of curcumin in water at 25 °C.

The peaks observed at 90 °C are 237 nm, 345 nm and 420nm and after cooling, the peaks observed are 275 nm, 431 nm and 500nm. The n- π* transition is red- shifted

upon cooling owing to aggregation and less polar microenvironment caused due to aggregation and clearly, there seems a phenomenal change in the π- π* transition. And this change is a physical change, as the peaks gain back the respective position (237 nm, 345 nm and 420 nm) upon re-heating to 90 °C. Also, the shift from 431 nm to 420 nm upon heating indicates breaking of the interactions therein. Therefore, the spectrum analysis implies the picture of curcumin structure that could be visualized as one in which the structural clusters of curcumin flicker into and out of one form to another form on a rather rapid time scale, maintaining an equilibrium between the different states that is dependent on the temperature of the system. Thus the structural model of curcumin is proposed, based on the spectroscopic data, to be composed of a relatively small number of distinguishable (by absorption spectroscopy) species. The structural arrangements for the species vary with respect to the temperature and solvent effect. An increase in temperature results in an increase in the number of the H-bonds broken and therefore, a variation in the type, size and/or number of the structural units. Conditions which would change the distribution of the strength of the H-bonds would necessarily change the absorption maximum of the molecule.

Thus, depending upon the temperature of the system, the discussion of the results obtained is as follows: as explained before, upon heating, the breaking of the intra-molecular H-bond leads to the absorption maximum at 345 nm. This is one population of curcumin molecules with their polar groups exposed, existing in the solvent at that temperature along with the other population whose distribution contributes to the λ_{max} at 420 nm, where the intact molecules are not much affected by the polar water environment. The peak at 420 nm is characteristic of curcumin in almost all organic solvents (except like ethyl amine, which is highly basic). Upon cooling down, the formation of H-bonding, non-specific dipolar or hydrophobic interactions takes place. Thus, where there was a sharp peak at 345 nm when the sample was hot, there exists a small shoulder upon cooling to room temperature. The species of curcumin existing in this state is converted to other forms (whose transitions are detected at 431 nm and 500 nm). Since more molecules are converted into the form absorbing at 420-430 nm, where molecules already exist, we note an increase in the intensity. Thus the intensity of the 420 nm peak is shot up with a red-

shift to 431 nm after cooling. Once the polar groups in the molecule are exposed by heating, when it is cooled back, there are possibilities of intra-molecular H-bonding, inter-molecular H-bonding and hydrophobic interactions between curcumin molecules and inter-molecular H-bonding between curcumin and water molecules. Owing to these interactions the small red-shift could be explained at 431 nm. However, we also observe another shoulder at 500 nm, which could be due to larger aggregates of curcumin molecule formed upon cooling. This peak is definitely absent upon re-heating the solution. There are both empirical and theoretical attempts made to relate the principal or longest wavelength maximum with chain length; [31] as evidenced, the increasing value of λ_{max} alludes in a conclusive manner for increasing length of the conjugated curcumin molecule when it is present in the aggregated state. When the sample is re-heated, the intensity is increased more than before due to the obvious reason that now more molecules are exposed due to the intra-molecular H-bond breaking in the system.

More proof of the proposed hypothesis is shown in the inset of Figure 5.5A, where the optical transmission of the sample is exhibited. Sample vial (i) is that of curcumin in water at 90 °C, and it is an optically transparent solution. The same sample is cooled to room temperature (ii), and we observe that there is turbidity in the sample. Here, as seen in the picture, owing to the milky appearance of the sample, we suspect that the spectrophotometry of this turbid suspension of curcumin particles in water involves a large scattering contribution. We can infer from this temperature dependent behavior of the sample that the aggregation of the molecules take place upon cooling. It is also important to note that curcumin dissolved in other solvents obey Lambert-Beer's law suggesting the absence of aggregation of molecules, however, in water, curcumin fails to obey the same. Figure 5.5(B) shows a schematic of the mechanism explained above.

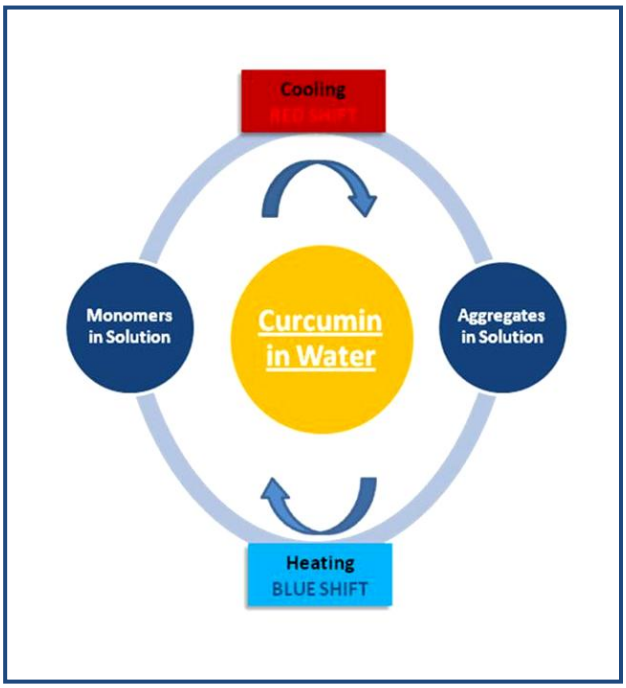

Figure 5.5. (B) Schematic picture of dissolution of curcumin in water upon heating and cooling, and its corresponding blue shift and red shift in its absorption spectra.

Additionally, to understand the dependence of these peaks of curcumin in water on the solvent also, we took equal amounts of curcumin in different ratios of water and methanol percentage. The absorption spectra of the sample is shown in Figure 5.6, where at 50% of methanol and water mixture, the principle peak is at 420 nm alone though there is also a weak shoulder around 350 nm. As the percentage of water increases, we note that the intensity of the peak at 350 nm increases however it remains relatively lower than the peak at 420 nm unlike the spectrum of curcumin in water alone at high temperatures. Note that in water, at high temperature, the peak was obtained at 345 nm, where as in water-methanol mixtures it is 350 nm, in accordance with the fact that the mixture is less polar. Though the presence of methanol in water reduces the solvation energy required for curcumin to dissolve in the mixture, water molecules being highly miscible with methanol easily forms strong H-bonds with methanol and hence it does not reduce the energy required for the π- π^* transition. Therefore, we observe blue-shift. This implies that the peak observed in water around 345 nm is solely due to the solvent effect; wherein the structure of the curcumin molecule in that state gives rise to this signature.

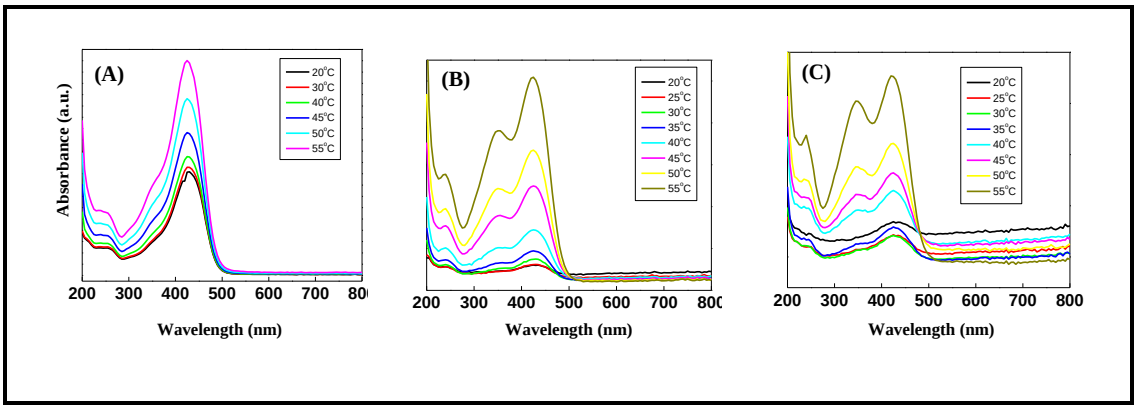

Figure 5.6. UV-Visible spectroscopy of curcumin in water and methanol at increasing temperatures and at different vol %(A: 50% methanol, B: 20% methanol and C: 10% methanol in water). The comparison clearly shows that the structure of the peak in water is merely a solvent effect.

In our study, we did not use half-curcumin, 4(4-hydroxy-3-methoxyphenyl)-3-buten-2-one (hC), a close analog of ferulic acid as a potential model of curcumin, [26] due to the obvious difference in the spectral properties between curcumin and hC in water. To further study this system, we filtered the solution, containing 0.5 g of curcumin in 325 ml water, after heating it up to 95°C, using Whatman filter paper (retention size ~ 11 micron); much of the insoluble curcumin remained as residue owing to its sparingly soluble nature even at high temperature. The filtrate is a stable yellow solution of curcumin dispersed homogeneously in water as explained before. Then, immediately, while it is still hot at > 95°C, we filtered the same solution using 20 nm filter. Surprisingly, we found that when filtered immediately, the dilute solution of curcumin filtered out as shown in vial (i) in Figure 5.7. However, upon filtering the curcumin solution, after cooling back to room temperature, most of the color in the solution was lost as shown vial (ii) in Figure 5.7, indicating that the curcumin molecules, though in solution, has aggregated into larger sizes and are not filtered out by a 20 nm filter, supporting the explanation given above. Though this is a simple physical test, it strongly supports the mechanism.

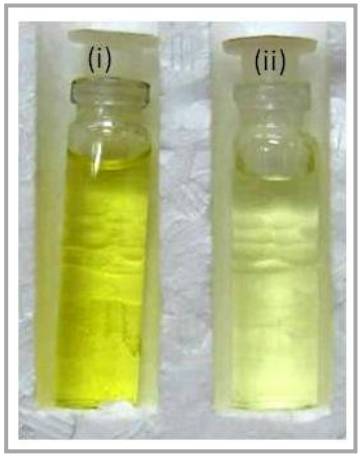

Figure 5.7. Picture of curcumin in water after filtering through a 0.22 μ filter at different temperature. (i) Color of solution filtered immediately after dissolution by heating and (ii) Color of solution filtered after cooling.

This is an important observation, in accordance with our absorption data, revealing that as the temperature begins to reduce, curcumin mostly precipitates back to its stable form of keto-enol-enolate tautomer, recrystallising into few monomer units. The more intriguing observation is the fact that not all of the curcumin precipitates back immediately. We have observed that for more than a month's time, the curcumin in water remains stable, which can be used for any further assays or applications. Hence, without the use of a co-solvent, or other chemical means to modify the molecule and thus affecting its activity, we note that curcumin gets into the water phase and remains stable.

5.1.2.3. Establishing and estimating solubility of curcumin in water

'Solubility' of curcumin in water upon heating is an ambiguous term to use in this study. As observed and established in the above explanations, the tests reveal that curcumin is more dispersed in the solvent (water) than dissolved, though it is readily available for biochemical reactions and drug actions. And the amount of curcumin in the solvent is extremely low even after heating it in water. Establishing the amount of curcumin that goes into the solution phase with acceptable accuracy is difficult. That explains the lack of any work relating to work on curcumin alone in water so far in literature. After repeated tests to estimate the amount of curcumin that is in

water, we could roughly calculate 1-10 µg/ml, using gravimetric analysis. However, since decrease in temperature could lead to the molecule precipitating out of water to form aggregates of solid curcumin, ensuring the level of curcumin in solution phase could be erroneous. Hence we cannot accurately calculate the molar extinction coefficient of curcumin in water, as reported in some previous studies, since aggregates are formed and Lambert Beer's law cannot be applied. Moreover, for conjugated dienes, ε_{max} cannot be predicted with accuracy.

5.1.2.4. Addressing the stability of curcumin in water

To determine the stability of curcumin in water, we used UV-vis spectroscopy, FTIR spectroscopy, NMR spectroscopy and HPLC techniques.

The aqueous sample was filtered through a Whatmann filter paper to remove particulates, dried to remove the water and re-dispersed in the desired solvent for all the techniques. For UV-visible spectroscopy study, the dried sample was dissolved in methanol and the spectrum was acquired as shown in Figure 5.8A. There is no change in the spectrum of curcumin sample due to the heat treatment as evidenced in the spectrum.

Note that the amount of curcumin treated in water and re-dissolved in methanol is less compared to the amount of untreated curcumin in methanol as seen in difference in the intensity of λ_{max} and the color contrast in Figure 5.8. Curcumin dried in a similar way was dissolved in deuterated methanol and the sample was submitted for proton NMR spectroscopy.

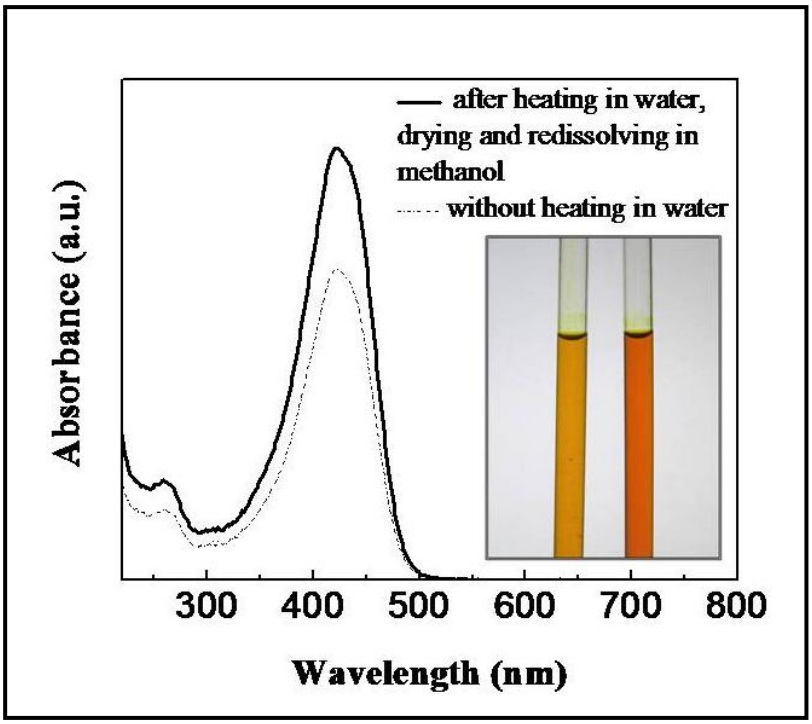

Figure 5.8. UV-vis spectra of curcumin in methanol. The solid curve shows the absorption spectra taken after dissolution of curcumin in water (till 100^{o}C) and thereafter drying it and resuspending in methanol. The broken curve shows the absorption spectra of curcumin in methanol without heat treatment. The picture in inset shows the color of the curcumin in methanol. We have shown two different cases where the darker contrast in the second tube is due to higher amount of dissolved curcumin in methanol.

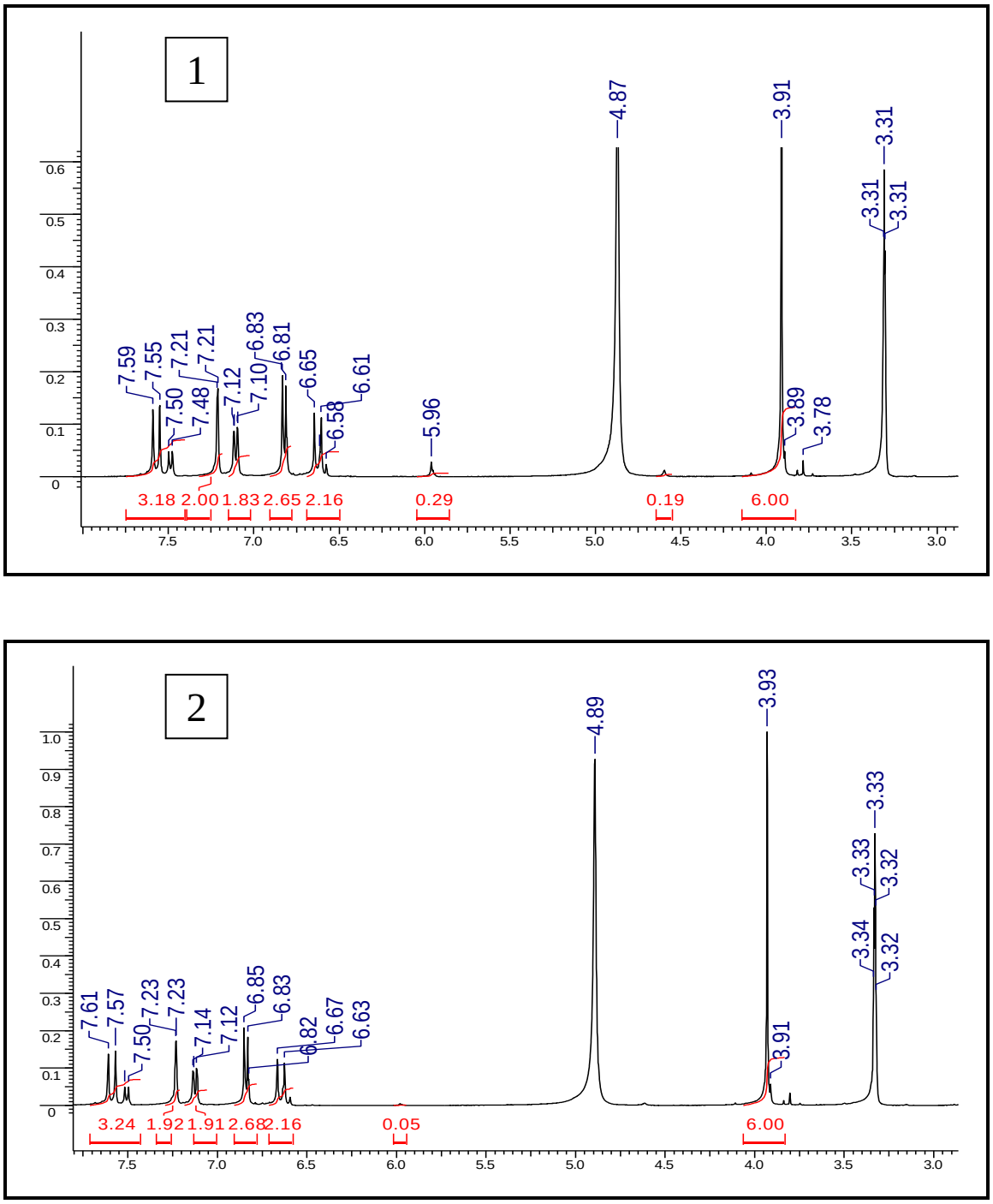

Figure 5.9. Proton NMR spectra of curcumin in CD_3OD. The first spectrum is that of curcumin without any heat treatment and the second spectra is that of curcumin with heat treatment in water.

The ^{1}H NMR spectra were run on a 400 MHz Bruker AVANCE instrument using a broad band probe with a z-gradient coil. Chemical shifts (δ) are quoted in ppm and are referenced to solvent CD_3OD. The NMR spectra shown in Figure 9 also revealed that there was no change in the molecule.

For FTIR spectroscopy, the sample while heating was taken and coated onto piranha-treated silicon wafers, dried and data acquired from a Perkin-Elmer spectrophotometer. We observe that upon heating neat curcumin, there is no observable vibrational change as shown in the IR spectra below (Figure 5.10).

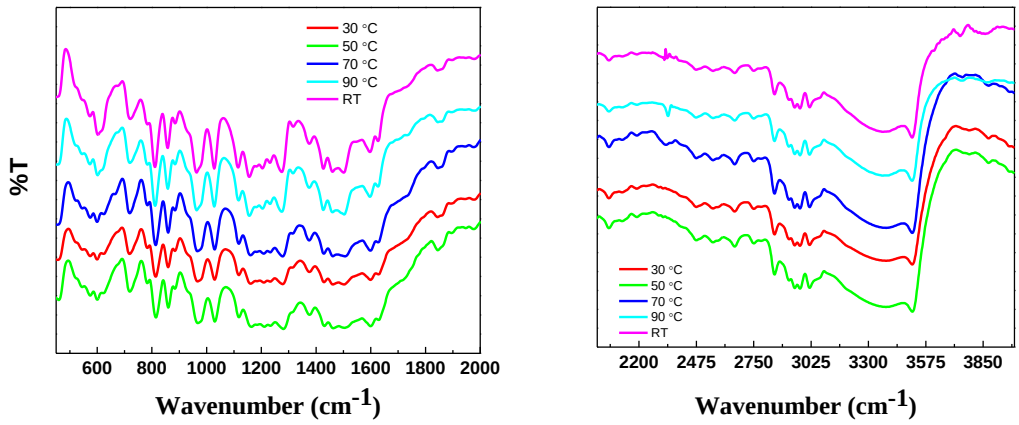

Figure 5.10. FTIR spectra of curcumin at different stages of heating in water.

To further analyze, we obtained HPLC chromatograms (Figure 5.11) on the sample for verification. The HPLC system used was Waters Delta 600 series and a wavelength of 425 nm was used for detection. Chromatographic conditions used are as follows: the elution was carried out with gradient solvent systems with a flow rate of 1.0 mL/min at ambient temperature. The mobile phase consisted of methanol (A), water (B), and acetonitrile (C). The sample was determined using the above solvents programmed linearly from 45 to 65% acetonitrile in B for 0-15 min. The gradient then went from 65 to 45% acetonitrile in B for 15-20 min, with a constant of 5% A. The compounds were analysed using HP ChemStation software.

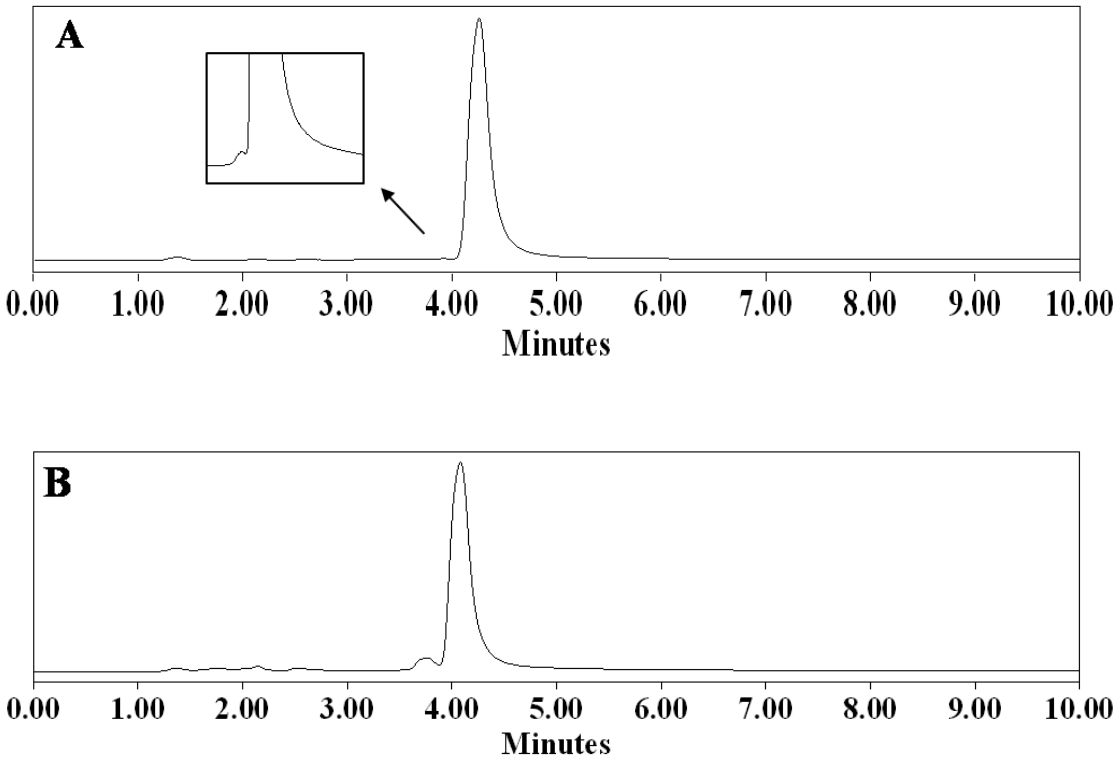

Figure 5.11. HPLC chromatograms of curcumin (A) before heating (B) after heating in water, drying and re-dissolving in methanol.

The HPLC analysis of as-received curcumin in methanol shows a peak at retention time of 4.3 min, which corresponds to curcumin (Figure 5.11A). [33] Also there is a small peak at around 3.75 min which corresponds to bisdemethoxycurcumin ((1E, 6E)-1,7-bis(4-hydroxy phenyl)hepta-1,6-diene-3,5-dione) (zoomed view). Bisdemethoxycurcumin is another curcuminoid present in turmeric whose structure (Figure 5.2B) is similar to that of curcumin. Since these two curcuminoids acts synergically, there will always be a trace of bisdemethoxycurcumin along with curcumin [34]. The HPLC analysis of heat treated curcumin (Figure 5.11B) shows that curcumin has not undergone any chemical change or degradation because of heat treatment. However, the intensity of the peak corresponding to bisdemethoxycurcumin is enhanced little bit; this can be explained by the absence of non-polar methoxy group in this molecule and hence enhancing its availability in polar water as compared to curcumin with two methoxy groups. Further

quantification into these processes is required; however, due to the sparingly low availability of the compound (note the intensities in the HPLC chromatogram) in the aqueous solvent even after heating, it is difficult to analyze.

5.1.2.5.Fluorescence of curcumin in water

In Figure 5.12, we have shown the photoluminescence spectrum (excitation wavelength is 420 nm) of curcumin in water at room temperature, after dissolution at high temperature and filtering it through the Whatman filter paper. As evident from the emission spectra, curcumin emits quite strongly in water.

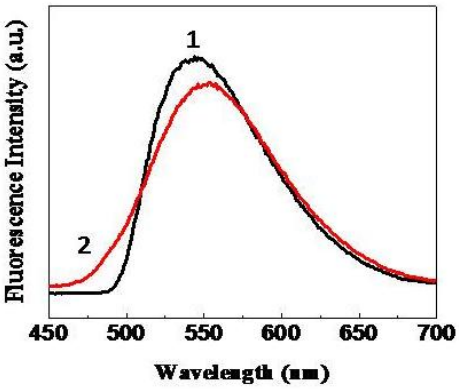

Figure 5.12. Photoluminescence of curcumin in methanol (1) and water (2) at the excitation wavelength of 420 nm.

In a previous report, Chignell et al.[26] showed that both intensity and the wavelength of the most intense emission peak of curcumin are highly sensitive to the nature of the solvent in comparison to the absorption spectra. In our study we note that at least between changing the solvent from water to methanol, the emission spectra does not change a lot. It is important to note in our results that the emission peaks of curcumin in water is tending to more symmetrical as compared to that of in methanol; this shows that the curcumin and solvent aggregates are not non-symmetrical in nature. From Chignell *et al.*'s observation that the position of most intense absorption band in spectrum of curcumin is solvent independent and its fluorescence intensity is solvent dependent, we see in our study that the fluorescence absorption is solvent independent. This could be because of the packing of curcumin molecules into

closed structures and thus the feeble difference in the spectra in spite of the large difference in the interaction of curcumin with water and the interaction of curcumin with methanol.

5.1.3. Conclusions

Little or no spectroscopic work is reported about the behavior of curcumin in aqueous system. We present a detailed spectroscopic data on the interaction of curcumin with water in a temperature dependent manner. By contrast, considerable attention has been given to the spectra of curcumin in various organic solvents in various reports, where the absorption contributions are assigned to the molecular structure with respect to the solvent in which it is dissolved. Electronic transitions are characteristic of molecular structure of the molecule. A change in the electronic transition therefore represents a change in the molecular structure; however, there are other factors that could affect the transition, such as the solvent effect, presence of an auxochrome, temperature, aggregations of molecules, etc. To clearly establish the stable conformation of the molecule in aqueous solution, computational predictions are required and further detailed experimentation is needed. At this stage, it is not possible to state the correct conformation of curcumin in water at high temperature. We observe in our study that the solvent plays a major role in the absorption spectrum of curcumin and we make use of this interaction to understand the process of dissolution. In this work, we have shown that curcumin is dispersed in water at high temperatures and aggregates upon cooling, with some precipitation out of the solvent. Based on our detailed spectroscopic measurements at various temperature conditions, we propose that it is the breakage of intra-molecular H-bonding that probably leads to the increased availability of curcumin molecule in water. As the temperature is increased, the thermal energy helps in breaking the bonds and exposes the polar hydroxyl (—OH) and keto (>C=O) group which enhances the solubility of the ampiphilic molecule. Also, our gravimetric analysis estimates its amount to 1-10 μg/ml at ~ 95 °C. Further study is also carried out to investigate the changes, if any, upon heating curcumin in aqueous phase and we observe that there is no degradation of the molecule. The curcumin dissolution at high temperature in water is made use of synthesizing gold nanoparticles as explained in the next section.

This study would help further research on curcumin in water and its applications in biological systems and pharmaceutical industries. Possible enhancement in its bioavailability cannot be overlooked considering the promising utility of this report.

5.2.1. PART II: Synthesis of gold nanoparticles using aqueous curcumin

Among other possible ways to overcome this problem of bioavailability of curcumin[35], nanoparticles[36], specifically metal nanoparticles, seem to overcome this problem in aqueous media, providing enhanced activity due to (1) conjugation onto a large surface to volume moiety, (2) increased half-life, (3) enhanced stability and (4) resistance to metabolic processes. Previous reports of use of nanoparticles as carriers of curcumin, circumventing the hydrophobicity of the molecule as a hindrance in its solubility involves a polymer-based nanoparticle. [37] However, these results proved little advantage in terms of enhanced solubility/availability in water and potent anti-oxidant activity.

We have shown in our recent paper that the curcumin heated to increase its solubility is stable enough to retain its chemical nature and anti-oxidant activity [Ramya Jagannathan, et al. (communicated)]. In the present paper a new and a very promising tool against various disorders and diseases (such as neurodegenerative & cardiac problems) has been proposed, which aims at an improved pharmacokinetic activity of curcumin[23] using noble metal nanoparticles. The high surface areas of these small particles allow them to be solubilised into the bloodstream where micro particles or larger particles cannot. Gold nanoparticles have been proved to be effective drug carriers and diagnostic probes. Biocompatibility of gold nanoparticles is well reported[38]. This work demonstrates the promising use of curcumin in conjugation with gold nanoparticles as a good showcase of drug delivery. We have used curcumin *in situ* to synthesis gold nanoparticles in aqueous system, where curcumin acts as a reducing agent.

The anti-oxidant activity of the curcumin reduced gold nanoparticles being functional; it could act as a promising pharmacological drug for human use. With the efforts to enhance the solubility and availability of curcumin, this work has paved a new way of using the curcuminoids towards possible drug delivery and therapeutics. Extensive research is carried on and a plethora of review articles are available on the use of gold nanoparticles for drug and gene delivery.[39]

5.2.2. Results and discussions

The synthesis of gold nanoparticles comprises of a facile mixing of the reactants around a temperature of 90 °C as explained. The deep red color of the reaction mixture indicates the formation of gold nanoparticles. We tried the reduction of various concentrations of chloroauric acid by curcumin, which helped us in determining the optimum concentration of chloroauric acid by measuring the absorbance in the UV-NIR region. For the synthesis of gold nanoparticles using curcumin, the aqueous solvent (500 ml) was heated on an oil bath up to 95 °C, when chloro auric acid (optimized concentrations is 1.5 x 10^{-4} M) followed by curcumin (4 mg) was added under constant stirring. The high temperature of the reaction mixture was to solubilise curcumin in water and also to kinetically control the nucleation of the gold nanoparticles so as to achieve monodisperse spherical particles. Immediately after mixing the reactants, heating was stopped and the reaction mixture was allowed to cool to room temperature. Within few minutes of mixing, deep red color of gold nanoparticles is formed.

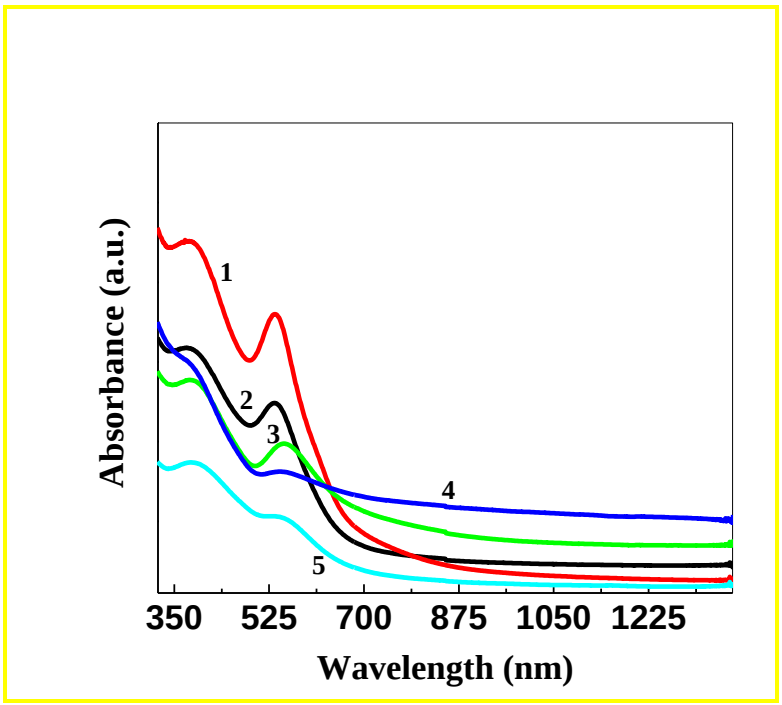

Figure 5.13. UV-Visible Spectroscopy of gold nanoparticles at different concentrations: (1) 1 x 10^{-4} M, (2) 1.5 x 10^{-4} M, (3) 2 x 10^{-4} M, (4) 5 x 10^{-4} M and (5) 5 x 10^{-5} M, synthesized by curcumin.

The pH of the sol is 5.67. It is known that curcumin is a superb H-atom donor, based on the rate constants of H-atom transfer reactions. Therefore, it appears that it is better than well-known, "classical" H-atom donors as thiol [27]. This explains the ready reduction of chloroauric acid into gold nanoparticles. *In vivo* also curcumin is reported to undergo extensive reduction, followed by conjugation[23].

Thus, in view of this, curcumin probably readily reduces gold ions to zero oxidation state gold and also caps them to form stable sol. The bioconjugation onto the gold nanoparticles makes it a very stable sol and the results confirmed that the bioconjugation of curcumin on gold nanoparticles showed an improved bioavailability as compared to curcumin alone. Figure 5.13 shows the surface plasmon resonance of these gold nanoparticles synthesized at different concentrations of chloro auric acid; we observe that unlike our previous reports using different biomolecules for synthesis of gold nanoparticles,[40, 41] we do not observe any anisotropic growth here. After the synthesis of colloidal gold solution, we dialyzed the solution to remove any unbound curcumin molecules as well as unreduced gold ions by using a cellulose tube (MW cutoff 12 400 D) against 1 L of deionized water for 9 h at 30 °C. We repeated the dialysis process to make sure the removal of unbound curcumin molecules as well as unreduced gold ions was complete. We used the dialyzed curcumin synthesized gold nanoparticles for various characterizations as discussed.

The isotropic SPR of gold nanoparticles is further supported from the TEM micrographs (Figure 5.14A, B) of the nanoparticles where the particles are largely around 20 nm in size (Figure 5.14C). The particles are primarily spherical in shape, though a few equilateral triangles are also seen in Figure 5.14A.

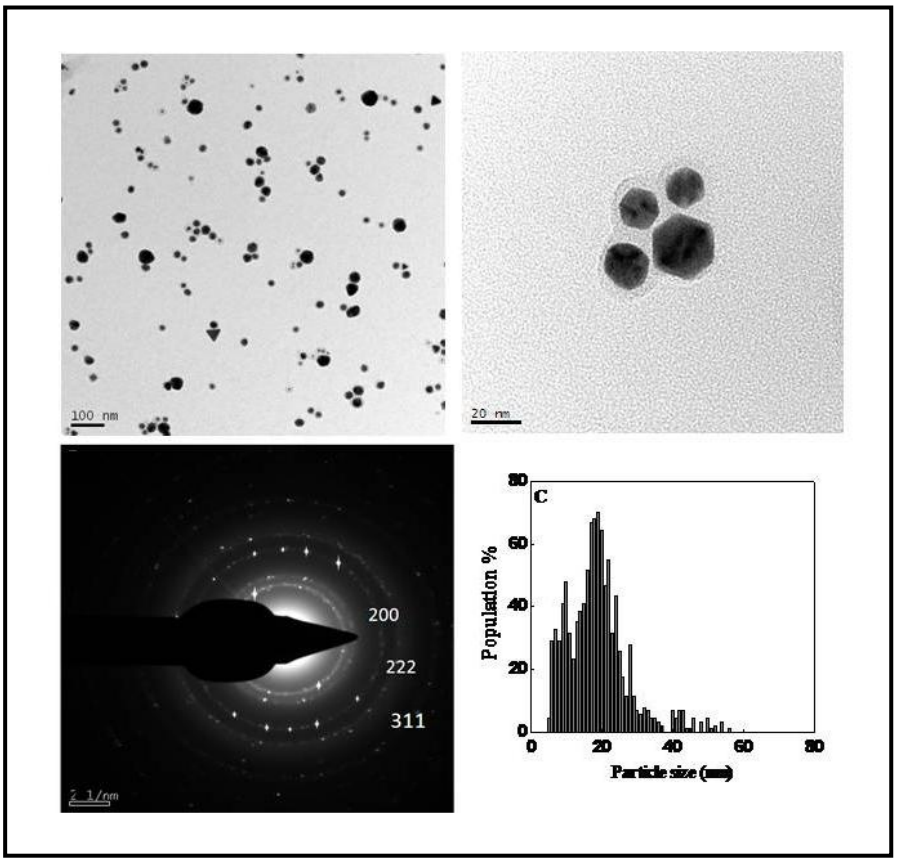

Figure 5.14. TEM micrographs of gold nanoparticles (1.5 x 10^{-4}M) synthesized by curcumin (A), SAED pattern (B) and the particle size distribution (C).

The 20 nm size of these particles is commendable for use to deliver into biological systems. In this study, the optimized concentration of choloauric acid, 1.5 x 10^{-4} M is used for the synthesis and the as-synthesized gold nanoparticles are used for further characterization and analysis. The pH of the sol is ~5.67, and hence forming stable gold nanoparticles, since it is known that curcumin is stable in acidic conditions[29]. It exists in the keto-form under acidic pH; alkaline conditions degrade the molecule. The stable pH-dependence of curcumin molecules could form stable nanoparticles as well as stable conjugated molecules.

To empirically determine the amount of capping on the gold nanoparticles, thermo-gravimetric analysis was carried out. The weight loss of the capping molecule on the gold nanoparticles is plotted in Figure 5.15. Though the percentage of weight loss is found to be around 63$\pm$10%, it is not conclusive of the amount of the capping agent, since the melting point of gold nanoparticles, corresponding to this size regime (~20

nm) also falls under this temperature range[42]. Therefore, it would be presumptuous to conclude the weight loss of the capping molecules from the gravimetric analysis. Nonetheless, this experiment provides a depth of the information that could be possibly obtained using such techniques in different system, for example, as in our case the curcumin synthesized gold nanoparticles.

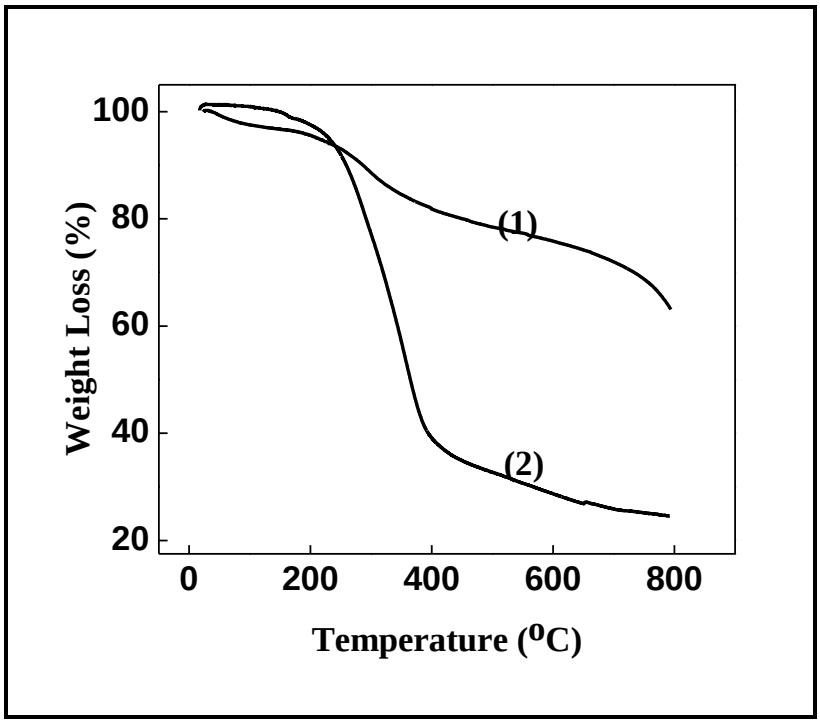

Figure 5.15. Thermo-gravimetric analysis of gold nanoparticles synthesized by curcumin. Curve 1: Curcumin alone and curve 2: Gold nanoparticles synthesized by curcumin

Figure 5.16 shows the fluorescence spectra of curcumin and curcumin reduced gold nanoparticles in water. It is known that the effect on chromophore fluorescence in close proximity to the surface of metal nanoparticles is due to the strong electromagnetic field generated at the surface of metal nanoparticles[43]. The oxidized curcumin molecules on the gold nanoparticles surface interact electronically with the surface to donate electron to the metal, thus quenching the fluorescence by non-radiative pathways available in the metal nanoparticles. Thus we see that the emission peak of curcumin in water, prominent around 550 nm is absent in the gold

nanoparticles synthesized by curcumin, when excited by the wavelength, λ = 420 nm.

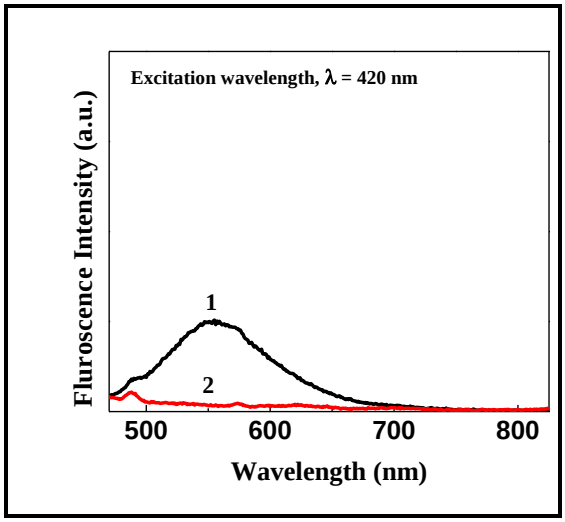

Figure 5.16. Fluorescence spectra of (1) curcumin in water and (2) gold nanoparticles (1.5×10^{-4}M) synthesized by curcumin in water. The Raman peaks of the water molecule have not been subtracted from the spectra.

The anti-oxidant activity of gold nanoparticles synthesized by curcumin was determined using the free radical, 2.2-Diphenyl-l-picrylhydrazyl ($DPPH^{\bullet}$). The radical $DPPH^{\bullet}$ absorbs at 515 nm, which disappears upon reduction by an anti-radical or an anti-oxidant species. Gold nanoparticles synthesized and stabilized by curcumin was reacted with $DPPH^{\bullet}$ and shown to possess anti-oxidant activity, with curcumin (in aqueous phase) alone as control. For each sample tested, the reaction kinetics was plotted as shown in Figure 5.17A. It shows the decrease in the optical density at λ = 515 nm as the radical $DPPH^{\bullet}$ is quenched by the anti-oxidant.

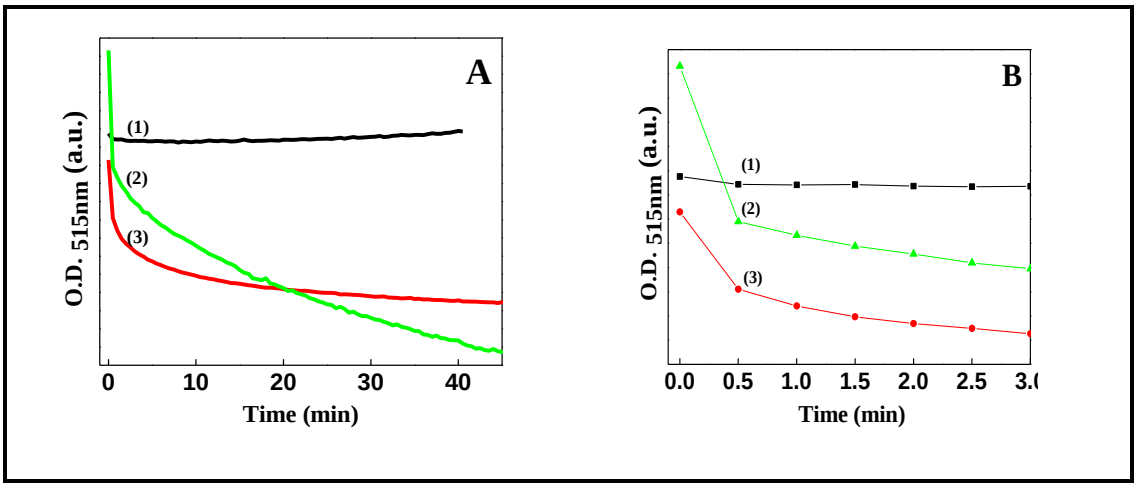

Figure 5.17. Anti-oxidant activity by DPPH radical test. (1) Only DPPH in water as control, (2) gold nanoparticles (1.5 x 10^{-4}M) synthesized by curcumin in water and (3) curcumin in water.

The use of DPPH method provides an easy and rapid method to check the presence of any anti-oxidant property. Since this reaction mechanism is highly solvent dependent, Curve (1) in Figure 5.17A shows plain water with the radical as a control, and we see that there is almost no quenching. And with temporal progression, it is a plateau. Curve (2) is the gold nanoparticles synthesized by curcumin and curve (3) is curcumin mixed with the radical respectively. The observation is a qualitative one owing to the difficulties encountered in quantifying the solubility of curcumin in water and hence a quantitative comparison between the sample and control is not valid here. Hence, the optical density on the ordinate is arbitrary and not comparative for quantifying. We can conclude from the observation of curve (2) and curve (3) that the rate reaction of anti-oxidant activity of gold nanoparticles synthesized by curcumin is progressively enhanced. The slope in curve (2) is more than in curve (3), as evident in Figure 5.16B. We could infer from the anti-oxidant activity that these nanoparticles are functional and could be used for further studies.

5.2.3. Conclusions

In conclusion, gold nanoparticles have been synthesized using curcumin in aqueous phase. These gold nanoparticles, reduced and capped with curcumin, are synthesized in a simple process without harsh chemicals. These curcumin reduced gold nanoparticles exhibit potent anti-oxidant activity, which promises for unlimited

medicinal use. This study warrants future investigation of the potent *in vitro* activity of the bio-conjugated nanoparticles and thereupon pharmacokinetics as well. Further studies such as regarding safety, needs to be guaranteed by performing tests on cells and animals.

5.3. References

1. Ishita Chattopadhyay, K.B., Uday Bandyopadhyay and, and Banerjee, R.K. (2004) *Current Science* 87, 44
2. Valianthan, M.S. (2003) *The Legacy of Caraka*. Orient Longman
3. Duvoix, A., *et al.* (2005) *Cancer Lett* 223, 181
4. Li, H.L., *et al.* (2008) *J Clin Invest* 118, 879
5. Morimoto, T., *et al.* (2008) *J Clin Invest* 118, 868
6. Ohori, H., *et al.* (2006) *Mol Cancer Ther* 5, 2563
7. Dunsmore, K.E., *et al.* (2001) *Crit Care Med* 29, 2199
8. Kuhad, A., *et al.* (2007) *J Agric Food Chem* 55, 10150
9. Gan, L., *et al.* (2008) *Neurobiol Dis* 29, 71
10. Ono, K., *et al.* (2004) *J Neurosci Res* 75, 742
11. Yang, F., *et al.* (2005) *J Biol Chem* 280, 5892
12. Balasubramanian, K. (2006) *J Agric Food Chem* 54, 3512
13. Dairam, A., *et al.* (2007) *J Agric Food Chem* 55, 1039
14. Kumar, S., *et al.* (2001) *Bioconjugate Chemistry* 12, 464
15. Negi, P.S., *et al.* (1999) *J Agric Food Chem* 47, 4297
16. Kim, M.-k., *et al.* (2003) *J Agric Food Chem* 51, 1578
17. Hatcher, H., *et al.* (2008) *Cellular and Molecular Life Sciences* 65, 1631
18. Fiorillo, C., *et al.* (2008) *Free Radical Biology and Medicine* 45, 839
19. Anand, P., *et al.* (2008) *Cancer Lett* 267, 133
20. Lin, J.K., *et al.* (2009) Molecular Mechanism of Action of Curcumin. In *Food Phytochemicals for Cancer Prevention II*, 196-203, American Chemical Society
21. Bisht, S., *et al.* (2007) *J. Nanobiotech* 5, 3
22. Varalakshmi, C., *et al.* (2008) *Int Immunopharmacol* 8, 688
23. Anand, P., *et al.* (2007) *Molecular Pharmaceutics* 4, 807
24. Cheng, A.L., *et al.* (2001) *Anticancer Res* 21, 2895
25. Sharma, R.A., *et al.* (2004) *Clin Cancer Res* 10, 6847
26. Garcea, G., *et al.* (2004) *Br J Cancer* 90, 1011
27. Jovanovic, S.V., *et al.* (1999) *J Agric Food Chem* 121, 9677

28. Biji T. Kurien, A.S., Hiroyuki Matsumoto, R. Hal Scofield (2007) *ASSAY and Drug Development Technologies* 5, 567

29. Payton, F., *et al.* (2007) *J. Nat. Prod.* 70, 143

30. Tsonko, M.K., *et al.* (2005) *International Journal of Quantum Chemistry* 102, 1069

31. Dudley, H.W., and Fleming, I. (1996) *Spectroscopic methods in organic chemistry*. Tata McGraw-Hill

32. Colin N. Banwell, E.M.M. (2006) *Fundamentals of Molecular Spectroscopy*. Tata McGraw-Hill

33. Jayaprakasha, G.K., *et al.* (2002) *J Agric Food Chem* 50, 3668

34. HH., T. (2002) Solubility, chemical and photochemical stability of curcumin in surfactant solutions. Studies of curcumin and curcuminoids, XXVIII. *Pharmazie* 57, 820

35. Safavy, A., *et al.* (2007) *J. Med. Chem.* 50, 6284

36. Sahu, A., *et al.* (2008) *Biomacromolecules* 9, 2905

37. Bisht, S., *et al.* (2007) *J Nanobiotechnology* 5, 3

38. Shukla, R., *et al.* (2005) *Langmuir* 21, 10644

39. Han, G., *et al.* (2007) *NanoBioTechnology* 3, 40

40. Jagannathan, R., *et al.* (2007) *J. Phys. Chem. C* 111, 6933

41. Jagannathan, R., *et al.* (2009) *J. Phys Chem C* 113, 3478

42. Cortie, M.B., and Lingen, E.v.d. (2002) Catalytic gold nano-particles. *materials forum* 26, 1

43. Mooradian, A. (1969) *Phys. Rev. Lett.* 22, 185

SUMMARY

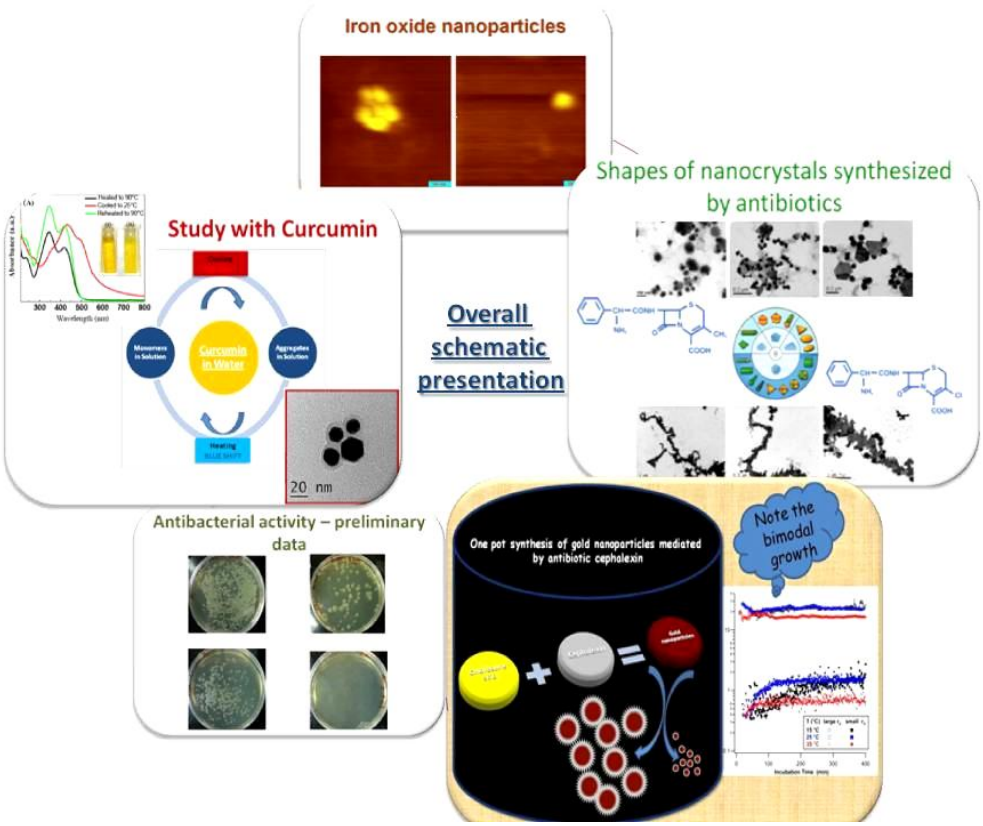

This summary reflects the salient features of the work presented in the thesis and emphasizes on potential avenues for future research work in this field.

Summary

Study of functionalizing nanoparticles using biomolecules in a facile pot, towards potential applications like anti-bacterial and anti-oxidant activity and analysis of the mechanism of formation and function using biological, physical and chemical methods is presented in this thesis. This is a promising work for enormous future scope of research study.

The work begins with the '*road not taken*' wherein antibiotics are used for the first time to synthesize stable gold nanoparticles. The use of antibiotics as the capping agent calls for attention due to the major global threat faced by the human population from the highly resistant pathogenic bacteria that is even now evolving, as we develop new means of combating them. Hence this work proves as a new mode of delivering the antibiotic into the environment/system where the bacteria are yet to develop resistance. The capped molecule is unlike the same antibiotic used for the synthesis in two ways:

1. Its redox potential is changed since it participated in the reduction of chloroauric acid into gold nanoparticles

2. It is bound onto the surface of the metal nanoparticle and hence not easily accessible for the lactamases to act upon it, thereby increasing the effective activity against the bacteria.

Further, the system also provides as a simple means of conjugation chemistry which can be used in biological research. Antibiotics being simple biomolecules that are extensively used in the infectious world are easily participating in the reduction reaction in a concentration dependent manner. In addition, antibiotics like cefaclor and ampicillin are also shown for their potential to form stable and active gold nanoparticles.

The synthesis, characterization and preliminary anti-bacterial activity are shown. This new delivery of antibiotics synthesized nanoparticles may not allow the bacteria to quickly gear up their resistance; instead they may get prone to the same.

This synthesis route is also a perfect model system to study the growth of the gold nanoparticles, which is elaborated in following chapter. The simple system is studied

in a temperature dependent manner using light absorption and scattering methods and the electron microscopy. Unique bimodal distribution of gold nanoparticles is reported for the first time in our knowledge using the DLS data. The transmission electron micrograph supported the presence of a large number of smaller 1-3 nm particles as well as larger particles around 25 nm. However, the fact that change in temperature, by an increase of 10 degree order, has nonetheless resulted in bimodal distribution of comparable sizes is highly intriguing. Change in temperature alters every aspect of the reaction. The stability and diffusion rate of the complexes formed in the reaction as well as the binding strength of the surfactant molecules to the growing nanocrystals are all strongly temperature-dependent. Moreover, increasing the temperature greatly decreases the stability of the intermediate complexes formed in solution and the binding of the surfactants to the nanocrystals surface, while increasing the diffusion rates of the complexes. This favors the nucleation and growth. However, too high a temperature may lead to uncontrolled growth so that it is impossible to exploit subtle kinetic or energetic effects to achieve precise control over the size and size distribution of the nanocrystals. Thus choosing an appropriate temperature range is one of the key steps in obtaining control over nanocrystal growth. In our study we see the expected change in the morphology of the particles formed at different temperatures. Hence, the ongoing process of this reaction system is complicated with various parameters affecting the size and shape. This offers as a very good model system that can be exploited to study the energetics involved. According to Howard Reiss's prediction small crystals will grow more rapidly than larger ones if monomer concentrations are sufficiently high. This prediction on which the 'size-distribution focusing' approach is based can be used to explain our observation of the particle morphology at low temperature. The slow growth conditions at low temperature does not allow for change in the size-distribution of the particles, however, the critical size, which depends on monomer concentration, shifts to a smaller value. This work presents a novel and detailed study of different systems of functionalisation of nanoparticles. The different facets of the study make it interesting. Better understanding of these nanosystems holds the key to exploring the exciting opportunities of this field to the full potential of colloidal nanoparticles.

As an effort to functionalize enzymes onto nanoparticles so as to have enhanced efficiency and stability, and improve ease of separation for industrial use, the

commercially important enzyme, Penicillin acylase was used to functionalize on chemically synthesized nanoparticles in a separate study. The system is characterized and the bioactivity of the enzyme capped on the magnetic nanoparticles is measured. True to the expected data, and industrially accepted limits, the immobilized enzymes had good activity when the enzyme activity was estimated. This is the first report of such a study using the Penicillin acylase enzyme, where numerable studies using polymers and different substrates are used for good immobilsation and activity. The advantage of using magnetic nanoparticles is in the ease of separation for washing and reusing after the biocatalyst has been used. Magnetic nanoparticles are already in the market for such purposes and they prove to be useful in such a utility. Further studies are underway to estimate the leaching percentage, pH stability, re-useablility and magnetic sensitivity, to make these nanoparticles useful.

Further, curcumin is used as the functionalizing molecule. Curcumin is a molecule that is making a revolution in the western world, both in the market and in the research field. Name a disease or disorder, curcumin seems to have an effect on it, for the better of it. Curcumin has been used to cap gold nanoparticles. However, like the previous report of synthesis using antibiotics, we observe that curcumin also reduces gold ions to form gold nanoparticles. However, the solubility of curcumin in water has been an issue for biomedical advantages, owing to the high hydrophobic nature of the molecule. Hence the first part of the chapter deals with the study of the physical and spectroscopic behavior of curcumin in water when heated at high temperatures. Such a sample is then used to produce stable gold nanoparticles in aqueous phase. A detailed study of the solubility of curcumin in water at high temperature which is not reported previously is presented in the last chapter. A remarkable change in the temperature dependent electronic transition behavior of the curcumin molecule is observed; however, the absorption spectra after cooling and heating cycles (between 25 ^{o}C and 90 ^{o}C) remain unchanged. The study indicates that it is perhaps the breaking of the intra-molecular hydrogen bonding which leads to the exposure of the polar groups and hence responsible for the dissolution of curcumin at higher temperature. We believe that formation of inter-molecular aggregates might be responsible behind a better room temperature stability of the molecules after cooling its aqueous suspension from 90 ^{o}C to 25 ^{o}C. This report warrants further studies to understand the mechanism of the process at depth.

Nonetheless, this curcumin in water is used to synthesize gold nanoparticles which exhibit good anti-oxidant activity compared to curcumin. Their potential use in fight against diseases where anti-oxidants are most helpful can be tested. In vitro studies, as a first step, would throw some light on the effective use of this system as a drug.

These systems need further exploration, to understand them, to verify their usability and to address the toxicity effects if any. Since the first line of exposure comes from the molecules that are functionalized on the nanoparticles, their behavior, properties and acceptance into the biological world depends on the functionalized molecule.

List of Publications

1. **Ramya Jagannathan,** Poddar, P. & Prabhune, A. "Cephalexin-mediated synthesis of quasi-spherical and anisotropic gold nanoparticles and their *in situ* capping by the antibiotic" *The Journal of Physical Chemistry C* **111**, 6933-6938 (2007).
2. **Ramya Jagannathan.** et al. "*In situ* observation of antibiotic mediated concurrent growth of two distinct homogeneous populations of gold nanoparticles in solution phase" *The Journal of Physical Chemistry C* **113**, 3478-3486 (2009).
3. Muralidhar L. Hegde, Bharathi, Anitha Suram, Chitra Venugopal, **Ramya Jagannathan,** Pankaj Poddar. et al. "Challenges associated with metal chelation therapy in Alzheimer's Disease", *Journal of Alzheimer's Disease* **17**, 457-467 (2009).
4. Raja Das, **Ramya Jagannathan,** Chandrashekar Sharan, Umesh Kumar, Pankaj Poddar "In Situ Observation of Antibiotic Mediated Concurrent Growth of Two Distinct Homogeneous Populations of Gold Nanoparticles in Solution Phase" *The Journal of Physical Chemistry C **113***, 21493-21500 (2009).
5. R**amya Jagannathan**, Priya Abraham, K. Vivekanand, Jagannatha Rao, P. Srinivas, Pankaj Poddar, "Effect of Temperature, Dielectric Environment, Intra/Intermolecular H-bonding on Electronic Transitions in Curcumin: A Mechanistic Study of its Solubility and Stability". (communicated)
6. **Ramya Jagannathan**, Priya Mary Abrahman, K. S. J Rao and Pankaj Poddar, *"In situ* reduction and bioconjugation of gold nanoparticles with curcumin in aqueous medium: A potential approach to combat various diseases". (manuscript under preparation)
7. **Ramya Jagannathan,** Ambrish Rathore, Pankaj Poddar, Asmita Prabhune "A study of immobilisation of Penicillin G acylase onto iron oxide nanoparticles". (manuscript under preparation)